University of Nevada, Reno

Automatic Extraction of Joint Characteristics from Rock Mass Surface Point Cloud Using Deep Learning

A dissertation submitted in partial fulfilment of the requirements for the degree of Doctor of Philosophy in Mineral Resource Engineering

By:

Rushikesh Battulwar

Dr. Javad Sattarvand/Dissertation Advisor

December 2021

THE GRADUATE SCHOOL

We recommend that the dissertation
prepared under our supervision by

RUSHIKESH BATTULWAR
entitled

Automatic Extraction of Joint Characteristics from Rock Mass Surface Point Cloud Using Deep Learning

be accepted in partial fulfillment of the
requirements for the degree of

DOCTOR OF PHILOSOPHY

Dr. Javad Sattarvand, Ph.D., Advisor

Dr. Behrooz Abbasi, Ph.D., Committee Member

Dr. George Bebis, Ph.D., Committee Member

Dr. Ebrahim Emami, Ph.D., Committee Member

Dr. Raj Kallu, Ph.D., Committee Member

Dr. Sean Warren, Ph.D., Committee Member

Dr. Robert Watters, Ph.D., Graduate School Representative

David W. Zeh, Ph.D., Dean, Graduate School

December-2021

ABSTRACT

A methodology for a computerized recognition of joint sets on 3D point cloud models of rock masses using deep learning is presented. The process starts with classifying joints on a 3D rock mass surface through training a deep network architecture and validated using manually labelled datasets. Then, individual joint surfaces are identified using the Density-Based Scan with Noise (DBSCAN) clustering algorithm. Subsequently, the orientations of the identified joint surfaces are computed by fitting least-square planes using the Random Sample Consensus (RANSAC). Finally, the joint planes are classified into different joint sets, and the dip direction and dip angle for each set are calculated. The performance of the proposed methodology has been evaluated using a case study. The results show that the presented procedure is fast, accurate, and robust.

DEDICATION

This dissertation is dedicated to my parents and brother. Thank you for always believing in me and being my pillar of strength throughout my life.

Jai Shivaji, Jai Bhavani

ACKNOWLEDGEMENTS

Foremost, I would like to express my sincere gratitude to my advisor Dr. Javad Sattarvand for his continuous support in achieving my dream of graduate education, for his patience, motivation, enthusiasm, and immense ingenuity.

I am grateful to the National Institute for Occupational Health and Safety (NIOSH) for funding this research. I would like to thank Dr. Masoud Naghadehi and Dr. Ebrahim Emami for their invaluable insights during this research project.

I would also like to thank Jorge and Meirzhan for their outstanding help in outdoor experiments and data analysis.

I am also grateful to my committee members: Dr. George Bebis, Dr. Behrooz Abassi, Dr. Robert (Bob) Watters, Dr. Raj Kallu, Dr. Ebrahim Emami and Dr. Sean Warren for their continuing guidance throughout the Ph.D. studies.

Finally, I want to thank my parents whose countless sacrifices and immense patience have helped me complete my education.

TABLE OF CONTENT

TABLE OF TABLES

TABLE OF FIGURES

CHAPTER 1 : INTRODUCTION

Rockfall is a significant safety hazard in open-pit mines that needs to be rigorously managed. It causes risk of fatal injuries for workers, damages to equipment and transportation routes, and may adversely affect mine production. The Mine Safety and Health Administration (MSHA) reports that highwall failure has been the cause of most fatal injuries in the U.S. surface metal/nonmetal mining operations in the past decade. However, despite the frequency of rockfall hazards and the crucial importance of managing them, there is not an automated system for prediction and alert of it in mining operations.

In practice, geotechnical engineers collect only a limited amount of rock mass data through face mapping (from accessible parts of the mine only) and study the rock features on a stereonet plot. This is followed by energy, velocity, bounce height and statistical analysis (using software packages such as ROCFALL) so that the overall risk of the rockfall, in a mine, is estimated. However, the statistics of accidents associated with rock fall in open-pit mines proves that these measures are not capable of accurately assessing related risks in a comprehensive manner.

Field measurements such as scan-line mapping with a geological compass near steep rock slopes of bench faces in open-pit mines present numerous problems. Safe access often does not exist to the rock faces to carry out geological mapping. Also, it is difficult to measure the orientation and geometry of large geological structures such as faults by simply measuring an orientation where a scanline crosses the fault. As well, mapping with a compass at the base of a steep slope exposes people to harm from rockfalls. On the other hand, as the mine is being developed, new measurements are required since the slope faces are drastically changed due to new production blasting practices.

Rockfall hazard has attracted a great deal of attention from both government bodies and researchers in recent years. A number of empirical methodologies have been proposed in order to prioritize and assess rockfall hazard in road rock cuts, as well as protective works have been tested and modeled. The best-known and most widely used techniques are the Rockfall Hazard Rating System (RHRS), developed for Oregon by Peirson (1992), and the Rockfall Hazard Rating for Ontario (RHRON), initially proposed by Franklin and Senior (1997) and further developed by Senior (2003). Empirical methods are not the only approach to dealing with the rockfall problem. Theoretical fall paths and trajectories have been extensively researched in laboratories and in situ by a range of authors, including.

The review of the literature reveals that despite the broad range of the research conducted on both rockfall assessment methods and photogrammetry-based methodologies, there is not any combined automated system for early warning of the rockfall hazard in open-pit mines nor for other applications. All existing technologies are laborious and expose the geotechnical engineers to hazardous areas with the risk of rock fall. They are also limited to the sampling from the accessible locations of the mine.

This research work is part of a NIOSH project titled “Automated Rockfall Risk Assessment System”. This is a five-year research project aimed at developing an early warning system for open pit mines focusing on detecting and quantifying rock fall risks. It has been proposed to develop an automated rockfall risk alert system (ARAS) integrating the unmanned aerial vehicle (UAV) imaging platform with advanced artificial intelligence (AI)- based technology to compute the overall risk of rockfall hazard in open-pit highwalls.

In this approach, the risk of rockfall will be perceived according to three major elements, (i) what is the probability of rock fall on a face, (ii) how far a potential fallen rock may travel, and (iii) how much would be the consequence of rockfalls in that area. The proposed technology will be able to analyze all rock faces of the mine (instead of a few sample areas) with automatic identification of the plains that fit over the exposed joints. The result will be a fully representative stereographic map of the geological features.

This dissertation is structured in the following order, consisting of four chapters which have been explained in brief below:

Chapter 1: Introduction

A summary of the issues related to the current technology used for rockfall risk assessment in the mining industry has been explained. The goals of this research work, as well as the entire NIOSH project, are explained.

Chapter 2: Literature review

A comprehensive review of all the techniques and algorithms available for extracting discontinuity characteristics from the 3D models of rock mass. A comparison between generating 3D models of rock mass using different technologies such as drone and Lidar has also been presented.

Chapter 3: Data collection

In this chapter, the applications and procedures used for collecting data from field has been explained. Specifically, this chapter explains the procedure for generating high-resolution 3D models of rock mass. This chapter also includes the designing and development of the Android application for flight mission planning and execution. It starts with explaining the UI of the developed application, flight planning algorithms and their validation.

Chapter 4: Automatic extraction of discontinuity characteristics

This chapter explains the proposed algorithm for extracting joint characteristics from 3D model of rock mass using deep learning and advanced clustering techniques. It also validates the results from the algorithms by comparing them with manually measured orientations. Finally, a novel algorithm to calculate the spacing distributions for individual joint sets has been presented.

CHAPTER 2 : LITERATURE REVIEW

2.1 Introduction

Discontinuities play a significant role in stability of slopes, and most of the highwalls stability analysis methods rely on measurement and characterization of the geological discontinuities since they define the weak planes in a rock mass along which the rock blocks detach and fail (Jaboyedoff et al., 2009; Kainthola et al., 2015). Application of decisive information on rock joints also help predict the flow of groundwater, potential to improve the quality of blasting in open pit mine highwalls, and finally a better understanding of the stability condition of the slopes (Zare and Jimenez, 2015a; Zare Naghadehi et al., 2013). However, acquiring accurate bench-scale geological information is mostly dependent on the field measurements, such as scanline mapping with a geological compass near steep rock slopes faces. Occasionally, surveyors use a laser scanner mounted on a vehicle to scan the rock face and utilize special software in the office to make the measurements digitally on a computer. In contrast, the long-range Radar/Laser scanner cannot be employed for rock mass characterization due to the low resolution of generated point clouds. Therefore, the current practice approaches present numerous limitations. Firstly, apart from being a laborious procedure, the access often does not exist to the rock faces to carry out geological mapping either in person or by a scanner. Additionally, there is a huge variation in the measurements at different locations of the mine, and it is difficult to accurately estimate the orientation and geometry of geological structures at few sample locations where a scanline crosses the structure. Furthermore, in-person mapping with a compass at the base of a steep slope or driving on such an environment exposes people to multiple types of hazards. Finally, as the mine is being developed, new measurements are required since the slope faces are drastically changed due to new production blasting practices.

Algorithms developed to use 3D models of slopes, such as point clouds or surface meshes, for mapping the geological discontinuities can address most of the above-mentioned problems. These algorithms may be helpful with performing larger quantities of measurements on a rock slope including inaccessible areas with much less efforts compared to the manual measurements. The subjectivity of evaluations is lesser this way since more data points on the slope are collected and the analysis is performed on the entire rock surface instead of a few scanlines preferred by the geologists. Additional measurements can be conducted at any time to refine the evaluation or solve ambiguities of interpretations (Ferrero et al., 2009a). Further, automated analysis of rock slopes using 3D models is cheaper than traditional survey scanning in terms of operational cost and time (Slob et al., 2005). Feng and Röshoff (2015) presented a survey of laser scanning techniques for site characterization of rock faces. Abellán et al. (2014) conducted a review of publications related to the use of terrestrial laser scanners for rock slope characterization, rock slope monitoring, and other applications. However, the previous study doesn’t include more advanced and recent research in the field of automatic characterization of discontinuities. Further, it doesn’t include the studies related to aerial photogrammetry-generated 3D models that are highly applicable today for slope monitoring purpose. Therefore, there is a need to conduct a more comprehensive review.

The next section of the paper presents the various techniques for the acquisition of 3D models of slopes like point clouds or triangular meshes. The International Society for Rock

Mechanics (ISRM) (ISRM, 1978) outlined a number of parameters for geometrical, mechanical, and hydraulic characterization of discontinuities, including orientation, spacing, persistence/trace length, roughness, aperture, wall strength, filling, seepage, number of sets, and block size. The main part of this paper reviews the efforts on the partial or full automation of extraction of six discontinuity parameters, including joint sets, orientation, joint continuity (or trace length), spacing, face irregularity, and block size. Note that in this study, the terms 'joints' and 'discontinuities' are used interchangeably.

2.2 Data acquisition methods

Reliable extraction of discontinuity information from 3D models mostly depends on the quality of the models and the method of data acquisition. For the successful implementation of an automated analysis, the data acquisition procedure should cover every significant discontinuity, need less overall cost and time than a traditional survey, and provide direct access to the slope with adequate positional accuracy in the model (Ferrero et al., 2009a).

2.2.1 Laser scanning

A Light Amplification by Stimulated Emission of Radiation (Laser) scanner is mainly used to create accurate and precise high-resolution digital elevation models (DEMs) in raster grids or triangular meshes or 3D point cloud. There are two types of laser scanning techniques depending on the position of the sensor, including Airborne Laser Scanning (ALS) and Terrestrial Laser Scanning (TLS). Most ALS and TLS used for ground measurement are based on the pulse method which uses the time of flight of laser pulse to calculate distances. Figure 1 summarizes the workflow and average time requirements for the acquisition of point cloud data of a rock slope using TLS. Armesto et al. (2009) used the TLS-measured points to characterize the geometrical parameters for stability analysis of a granite boulder. They identified four issues that need to be considered while planning data collection using laser scanners that are (i) location, (ii) number of stations to overcome occlusions, (iii) resolution, and (iv) reference system. TLS is also used for detecting rockfalls in an urban area by comparison of point clouds collected at different times (Abellán et al., 2011). Figure 2 depicts the Leica RTC360 which is a high-performance 3D laser scanning system.

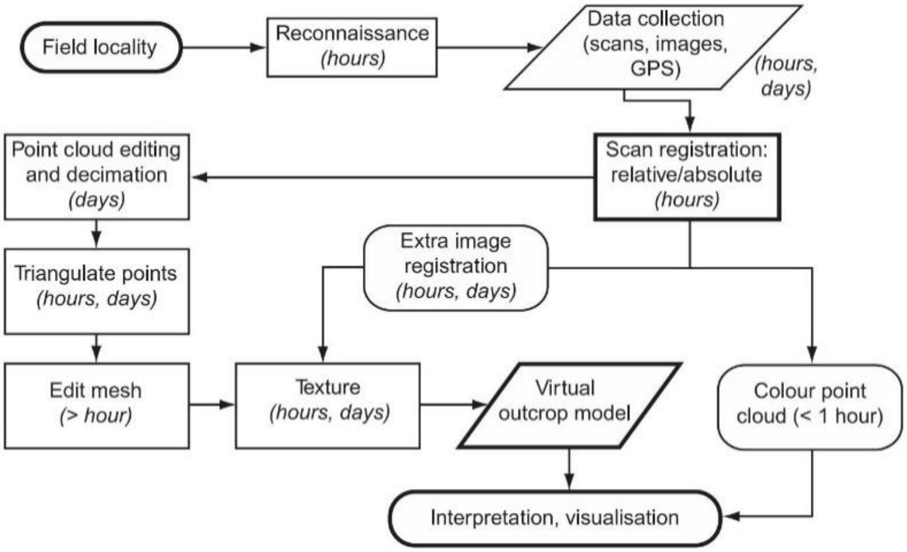

Figure 1 Workflow of laser scanning of rock masses (Buckley et al., 2008).

Riquelme et al. (2017) performed an analysis comparing the results of discontinuity characteristics acquired using TLS-generated point cloud and Unmanned Aerial Vehicle (UAV) data-generated point cloud, and found out that TLS data are more reliable. Further, the TLS category is found to be more accurate when the joint planes are not defined by enough planar points. Abellán et al. (2006) conducted a detailed study of rockfall using data from a long-range TLS. It enabled the collection of millions of points accurately in a few minutes. This study showed the ability of TLS to obtain reliable 3D displacement information over a large, unstable area (Oppikofer et al., 2009). The application of TLS for rock mass discontinuity characterization has been reported in numerous works in the literature (e.g., see Fardin et al., 2004; Slob and Hack, 2004; Bellian et al., 2005; Mavrouli et al., 2005.; Jaboyedoff et al., 2007; Olariu et al., 2008a; Lato et al., 2009; Sturzenegger and Stead, 2009a; Abellán et al., 2011; Gigli and Casagli, 2011; García-Cortés et al., 2012;Vöge et al., 2013).

Figure 2 Leica RTC360 3D laser scanner (Leica Geosystems).

Careful planning is essential to perform a TLS survey. Geological engineering field studies are conducted at a number of scales and distances; thus, it is necessary to plan ahead for required accuracy and precision mapping, scan resolution, and set-up of the scanner (Sturzenegger and Stead, 2009a). There is a need to take scans from multiple locations to avoid the occurrence of horizontal and vertical occlusions. Also, the position of the scanner must be elevated for better data quality and signal intensity. The data also has to be registered into the coordinate system. The 3D laser scanning is an expensive technique to be utilized for collecting 3D data of rock mass (Riquelme et al., 2017). A comparison of different parameters associated with data collection using a TLS and aerial photogrammetry is presented in Table 1. It is evident that laser scanning is a costlier method in terms of data acquisition and processing time. Moreover, the processing of LiDAR data usually involves considerable user input whereas photogrammetry-derived point cloud generation is mostly automatic.

Table 1 Comparison of laser scanning and UAV Photogrammetry data collection methods (after Cawood et al. (2017)).

Data acquisition method	LiDAR	UAV and Photogrammetry
Instrument	RIEGL VZ-2000 & Nikon D100	DJI Phantom 3 Advanced & on-board camera
Resolution	(0.0015°) Scale dependent	12 MP
Approximate cost (USD)	$100,000	$1800
Acquisition time (hr)	5	0.5
Processing time (hr)	35	8
Point cloud resolution (mm)	4	7

2.2.2 UAVs and Photogrammetry

The recent availability of ready-to-use UAVs as well as the advent of Structure from Motion (SfM) (i.e., digital photogrammetry software) have led to the increased application of UAVs for geohazard analysis (e.g., see Lee and Choi, 2015; Al-Rawabdeh et al., 2016; Car et al., 2016; Suh and Choi, 2017; Battulwar et al., 2019; Peik et al., 2020; Winkelmaier et al., 2020). There are various types of sensors that can be integrated into a UAV such as, visible-band, near-infrared and multi-spectral cameras, hyper-spectral cameras, thermal imaging, laser scanners, and synthetic aperture radar. A summary of each type has been presented in Colomina and Molina (2014). Figure 3 highlights the important components and workflow in the methodology for generating 3D models using drones and photogrammetry.

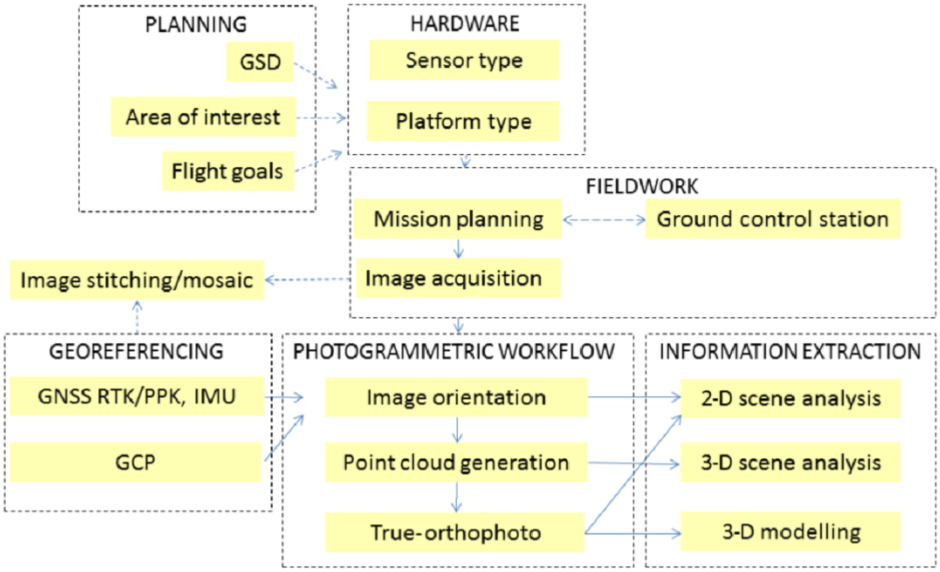

Figure 3 Workflow for generating 3D models using UAV and photogrammetry (Giordan et al., 2017).

The main reason for the augmented application of UAVs in Earth science industry can be attributed to the availability of low-cost drones with an at least 12 MP imaging sensor as cheap as $1000 (DJI, 2020a). The use of UAV with a high-resolution camera is significantly less expensive than a TLS unit, both of which generate almost similar point cloud data. Even with a low-resolution UAV, the authors have proposed a methodology for generating high-resolution 3D models for open pit mine slopes (Battulwar et al., 2020b). Further, the deployment of UAVs and the collection of images is a very simple process because of the availability of an array of commercial mobile applications for autonomous flight planning. Another advantage of using UAVs for rock mass mapping is the ability to collect high-quality images of rocks from a range of perspectives such as plane view, front oblique view, and side view, as well as close proximity views from a safe distance. This capability makes this technique superior to laser scanning in terms of safety and the capacity to map large size outcrops. Most of commercially available quadcopters weigh less than 2 kg which can be carried in a backpack (Zekkos et al., 2018). All these reasons make the UAVs ideal tools for remote collection of 3D data from rock masses. Several studies have successfully demonstrated the application of UAV photogrammetry for rock mass characterization (e.g., see Bemis et al., 2014; Vasuki et al., 2014; Greenwood et al., 2016; Vollgger and Cruden, 2016; Salvini et al., 2017). Figure 4 shows the DJI Matrice 600 Pro UAV fitted with a digital camera and Dual-Real Time Kinetic (D-RTK) GNSS for high-precision flights.

Figure 4 DJI Matrice 600 pro rotary-wing UAV (DJI, 2020b).

Although the use of UAVs is relatively easy, generating a high-resolution and accurate 3D model of rock mass requires a reasonable amount of experience and skills. The resolution and quality of the point clouds from UAV imagery depend on the relative height of the drone above ground, size of the imaging sensor, and an adequate proportion of overlapping between images (Di Franco and Buttazzo, 2016; Suziedelyte Visockiene et al., 2016). This process also requires the deployment of Ground Control Points (GCPs) in sufficient numbers that are distributed over the mapping area uniformly. The use of GCPs significantly improves the positional accuracy and scale of the 3D model (Martínez-Carricondo et al., 2018). Now, laying GCPs on steep ground is difficult because of accessibility limitations that is always the case in discontinuity characterization of open pit mine slopes. This problem can be solved using a slightly expensive solution that involves the use of double GNSS receivers and making Post Processed Kinematic (PPK) or Real-Time Kinematic (RTK) corrections.

Once the collection of images is complete, the data is processed in a photogrammetry software to generate the 3D models like point clouds, meshes, digital elevation maps and orthomosaic.

Table 2 lists the major photogrammetry software available in the market for professional and academic use. The process takes between a couple of hours to days depending on the number and resolution of photos as well as the computational power of the PC. Currently, companies such as Agisoft, Pix4D, Autodesk, and Bentley offer cloud processing feature that is relatively faster and saves hardware costs. However, mapping of a typical rock face (road cut) takes between 100-500 pictures that should be completed within a day (Vasuki et al., 2014; Salvini et al., 2017). The process of aerial imaging is also obstructed by bad weather conditions such as rain or high winds and, the image can practicality be diminished by the existence of the snow. Also, the position of the sun affects the number of shadows in the images, which may in turn create noise in the 3D models. The use of drones for non-recreational activities is regulated by federal agencies around the world like the Federal Aviation Administration (FAA) in the USA. Some of the regulations include the maximum flight altitude, which is 120 m, only line-of-sight operations, no flights over people and vehicles, etc. However, these regulations are easy to follow and make the UAV operation safer.

Table 2 Photogrammetry software and cost as of December 2020

Make	**Title**	**Price (USD)**	**Cloud processing available**
Agisoft (Agisoft, 2020)	Metashape	$3499	Yes
Pix4D (PIX4D, 2018)	Pix4Dmapper	$4,990/one-time or $291.7/month	Yes
Autodesk (Autodesk, 2020)	Recap Pro	$40/month	Yes
Bentley (ContextCapture, 2020)	ContextCapture Center	-	Yes
CapturingReality (RealityCapture, 2020)	RealityCapture	$4,000/one-time or $297.9/month	No
3DFLOW (3DF Zephyr, 2020)	3DF Zephyr	$4,665.96/one-time or around 299.1/month	No
Trimble (Trimble Geospatial, 2020)	Trimble Inpho	-	No
Changchang Wu (VisualSFM , 2020)	Visual SFM	Free	No
IGN (French National Geographic Institute) and ENSG (French National School for Geographic Sciences) (MicMac, 2020)	MicMac	Free	No
Alicevision (AliceVision, 2020)	Meshroom	Free	No

For the purpose of acquiring a detailed and high-quality 3D model of a rock mass, the UAV is required to capture a sufficient number of overlapping pictures from all the directions, which is a challenge to accomplish using manual maneuvering of UAVs. Another challenge is the continuous change of terrain in open pit mines. For example, due to blasting and extraction operations, the shape of slopes could potentially change every day. Since the profile of the ground is undulating, it requires the drone to follow the profile to constantly acquire required resolution images. These problems can’t be overcome using conventional commercial applications that use a parallel flight planning routine. This shows that there is a requirement for the development of customized flight planning applications using advanced coverage path planning algorithms as shown in Bircher et al., (2016), where such a problem has been modeled as a 3D art gallery problem or a two-stage imaging methodology proposed by Battulwar et al. (2020). Despite these drawbacks, it can be concluded that the application of UAVs for the collection of aerial images of the rock mass is a much safer, more efficient, and promising method.

2.3 Acquired Discontinuities Parameters

In this section, a brief survey of the works in the literature dealing with the extraction of rock mass discontinuity features including number and location of the joint sets, orientation, persistence, joint spacing, roughness, and block size, is presented. Firstly, all algorithms and methods presented in the literature are classified based on their parameter of interest. Secondly, a brief overview of the method, describing the procedure, is presented, and finally, their strengths and limitations are highlighted. The final goal of this analysis is to select procedures that can be used for developing an automated rockfall risk analysis system using UAVs. So, the procedures are reviewed based on their degree of autonomous operation and running time. For the same reason, in this paper, laboratory measurements of discontinuities based on drilling core samples are considered out of scope.

2.3.1 Joints Sets and Orientation

2.3.1.1 Clustering-based methods

Lato and Vöge (2012) presented a mesh-based software referred to as “PlaneDetect,” which extracts joint orientations by smoothing the mesh to remove noise in the first step, followed by identifying regions with co-planar points through the analysis of the angular difference between nodes. Each region was further analyzed by the same approach but different parameters for eliminating edge and blast-damage regions. Next, each co-planar region was classified as a discontinuity surface by comparing its area and average surface orientation variability with user-specified thresholds. Finally, discontinuity surfaces were clustered using fuzzy K-means algorithms where the value of K is set by the user. The user must also determine a total of nine parameters (eight thresholds and one K value) to render the accurate orientation of joint planes using this process. Despite such a high dependency on the user, the approach showed comparable results with manually mapped orientations.

The problem of working with mesh is that the quality depends on the process of triangulation and its resolution as small features could be neglected and complex shapes could lead to incorrect and distorted polygonal surfaces. Point clouds, on the other hand, provide lots of information in terms of millions of points but are computationally expensive (Gigli and Casagli, 2011).

The semi-automatic approach, which uses visual interpretation, generates results that are mostly non-reproducible because different operators have different expertise or may use different identification criteria. Studies indicate that even the same observer doesn’t reproduce the same results in the similar situations in multiple trials (Mabee et al., 1994).

However, geological analysis using 3D data is a complex process that requires the interpretation of complex geometries and subtle textural changes. Such an analysis necessitates significant intuition as well as deductive and inductive reasoning of the user. Therefore, it is important to note that a semi-automatic approach with user interaction is useful to allow geologically feasible results. Methods for automatic clustering of discontinuities based on their orientation without consideration of priori probabilistic models are common to determine the number of joint sets in point cloud datasets. Assali et al. (2014) used K-means clustering to classify 3D point cloud points into different joint sets based on their normal vector similarities. Olariu et al. (2008a) proposed a two-pass clustering method for estimating the mean orientation of joint sets. In the first pass, the multileader clustering was used to partition the point cloud into small clusters of which minimum and maximum sizes are defined by the user. The normal vector for each cluster was estimated using the principal component analysis (PCA). These clusters were partitioned into joint sets using K-means clustering algorithm where the optimal value of K is determined using a minimum description length (MDL) statistic (Barron et al., 1998). The orientation values measured from laser scanned rock mass point cloud using this method were reasonably accurate. Further, this method is completely unsupervised. However, the running time of method with respect to different sizes of point clouds needs to be investigated. Also, the effect of the parameters of multileader clustering method on the accuracy of measured orientation values is required.

Jimenez-Rodriguez and Sitar (2006) presented a spectral clustering algorithm which transformed the normal vectors for each point into a transformed K dimensional space. The point coordinates in transformed space were given by Eigenvectors of the normalized affinity matrix of normal vectors. K-means clustering was used for determining the clusters in a transformed space. The original points were assigned to the clusters same as their transformed point. Unlike usual clustering, the advantage of performing clustering in transformed space is that the transformed points are tightly clustered around the cluster centers, which increases the speed and accuracy of the process. It has also been claimed that the results of spectral clustering are more natural partitions than other clustering methods. Fuzzy K-means clustering performs a better clustering assignment compared to a non-fuzzy clustering method and was integrated with the spectral clustering algorithm by Jimenez (2008). The results were more accurate relative to spectral clustering solely using the K-means algorithm. However, the application of these techniques requires the prior knowledge of the value of K, i.e., the total number of clusters. Slob et al. (2005) used a fuzzy K-means clustering method directly with the orientation data for each facet of the mesh model for automatically clustering discontinuity sets. The clusters outliers were removed by iteratively using the Fisher's K value and selecting the cluster size with maximum K value. The working of the commercial software Split-FX (2020) is based on this method. Van Knapen and Slob (2006) automated the above method by determining the optimal value of clusters using cluster validity indices given by Hammah and Curran (2000) . Guo et al. (2017) further improved this method with the use of Firefly algorithm (Yang, 2009) to determine optimal locations of initial cluster centers for the fuzzy K-means algorithm and applied it to 3D point cloud data. They also segmented the raw point cloud into equal-sized cubes or octree partitioning and fitted a plane to each cube (using PCA) to determine its normal vector before clustering. This preprocessing step greatly reduced the computation time of the algorithm.

Chen et al. (2016) proposed a method for automatic clustering of mesh facets into joint sets using an improved K-means clustering algorithm. It was based on using sample density to find the initial clusters and the average Silhouette validity index (Rousseeuw, 1987) to estimate the optimum value of K. Silhouette validity index determines the validity of clusters. Its average was calculated for all data points for different K values and the K value with maximum Silhouette validity index was selected as the optimum. Individual joints inside each group were found by grouping all the neighboring triangles and setting a threshold for the minimum number for facets. Finally, RANSAC was being used to determine the plane parameters. The orientation measurements from this approach were compared to results obtained in Riquelme et al. (2014) for a test dataset. While the absolute values of deviation for dip and dip direction were almost the same, the average error for the dip was found to be higher. Further, it took 2.5 hours for automatic discontinuity extraction with almost 0.2M points because of the iterative steps for finding initial clusters centers and the optimum number of joint sets. Joint sets extraction results using the proposed automatic clustering showed that the technique was not robust enough for rock mass data with weathering and exfoliation features. The problem of clustering using the point cloud data is that small exposures and rough surfaces are under-sampled whereas a single discontinuity plane will be over-sampled because of higher number of representative points. In addition, clustering techniques and statistical models label each point of data as part of discontinuity surface, which can result in other sections of rock mass as weathered rock or trees also to be labelled as discontinuity surface.

With increasing computing power at their disposal, researchers have started developing sophisticated techniques for joint recognition on 3D point cloud data of rock mass.

Riquelme et al. (2014) proposed a semi-automatic method to estimate the joint plane equations by determining joint sets using Kernel Density Estimation followed by the application of density-based spatial clustering of applications with noise (DBSCAN) (Ester et al., 1996) in order for finding individual joint clusters inside each joint set. An example of the extracted joint sets is shown in Figure 5 where each set is represented by a different colour. Finally, PCA was used to fit planes to each discontinuity cluster. Approximately 80% of computation time was used in the estimation of normal vector for each point using the KNN search and the coplanarity test. However, using sensitivity analysis, it was shown that values for the parameters such as the number of neighbours and maximum deviation for the coplanarity test play a crucial role in discontinuity set assignment. It was found out that a greater precision of normal vectors can be obtained by considering higher number of neighbours in the KNN search. They recommended the KNN values ranging from 15 to 30 and an optimal threshold for the coplanarity test as 20%. The algorithm was tested on a dataset from the publicly available Rockbench repository (Lato et al., 2013). The performance of the algorithm was good except when the surface of the model was irregular. Finally, this algorithm was not recommended for performing analysis on large datasets (> 20M points) at once due to the difficulties in finding the dominant/principal orientations from stereo plots as well as extensive computation times.

Zhang et al. (2018) identified discontinuity planes by a simultaneous classification of the raster grids of rock mass digital elevation model with three parameters layers including slope aspect, slope gradient, and standard deviation of elevation using the Iterative Self-organizing Data Analysis Techniques Algorithm (ISODATA). The final planes from classified clusters were determined by selecting points with deviation from mean elevation

(DEV) values between +1 and -1. The method showed minimal differences with manual measurements. The accuracy depended on the two ISODATA algorithm parameters including the minimum number of points in cluster and radius of neighbourhood window. Also, an analysis in terms of the computation time with respect to point cloud size was required.

In order to eliminate human bias which is introduced in clustering algorithms in terms of K and initial cluster locations, Kong et al. (2020) utilized the fast search and found the density peaks (CFSFDP) algorithm (Rodriguez and Laio, 2014) to automatically detect the number of clusters. This algorithm only considers the local density of points and the minimum distance between a point and another point of higher density. Sine-squared of the acute angle between normal vectors was used as a measure of the distance between two points (Jimenez-Rodriguez and Sitar, 2006; Jimenez, 2008). Once the clusters were defined, DBSCAN was used for finding individual joint planes and RANSAC was used for determining plane parameters similar to Riquelme et al. (2014). The processing time for 1.5M points and 0.5M points was 5.5 and 1.5 hours, respectively. Majority of the time was consumed in creating the distance matrix of 3D points for the CFSFSP algorithm. The average error for this method was found to be less than that of by Riquelme et al. (2014) and Chen et al. (2016) for orientation computations. This increased accuracy proved the significance of computing normals using the iterative reweighted plane fitting (IRPF) method (Wang et al., 2013) and a better cluster segmentation using CFSFDP (Gao et al., 2019).

2.3.1.2 Region growing-based methods

Unlike the traditional methods of using clustering techniques for joint planes segmentation, Wang et al. (2017) proposed a region growing approach for extracting the full extent of joint planes from 3D point cloud. In region growing, a seed point is selected randomly from the point cloud and then the region is expanded by adding neighboring points satisfying the preset conditions. The point normal and curvature information estimated using K-nearest neighbors and least-squares plane fitting methods, are used to find and grow the seed points. The region growth and selection of new seed points were controlled using two user-specified thresholds based on angular difference between point normals. The ability to extract full extent of fracture regions and fast processing time are found to be the strengths of this method. However, the computation time steeply increases for more than 1M points. Also, the method needs improvements in terms of eliminating outlier clusters.

To improve the computation time using region growing for joint plane extraction in case of large point clouds with high resolution, Ge et al. (2018) suggested two solutions including gridded data and modified region growing algorithm. The raw point cloud was transformed into gridded data with evenly spaced rows and columns where each point could be accessed using row and column indices. This saved data retrieval and processing time in point clouds. Next, the modified region algorithm was characterized by an efficient growth criterion that increased the probability of making more neighbouring points as the seed points. The growth was controlled using a single user-specified threshold of maximum normal angle difference. Further, in this method, point normals were estimated using only four neighbouring points. This method resulted in a 97.66% less computation time compared with normal region growing. The segmented plane orientations were found to be closer to manual measurements. The identification of joint planes using this method is highly dependent on the threshold parameter where values should be between zero degree and the minimum normal difference between all joint planes.

Drews et al. (2018) further improved the accuracy and precision of region growing algorithm for joint plane segmentation by specifying additional growth criteria other than normal and curvature differences, such as distance of candidate points to the points and a fitted plane of growing region as well as standard deviation of candidate points. The increased accuracy was validated with statistical significance by comparing the orientation values with the ground truth (field measurements) and values from Virtual Reality Geological Studio (VRGS) (Hodgetts et al., 2007). It was found that the actual segmentation time using region growing was only around six percent and the rest of the time was used in normal vector calculations.

Hu et al. (2019) proposed an automatic approach for detecting joint planes in 3D rock mass point clouds by determining coplanar points in a Voxelized point cloud and merging individual voxels into planes by using region growing. Further processing was implemented after region growing to improve the accuracy of plane detection by using unprocessed points in the remaining steps. High accuracy and speed in detecting planar regions in point cloud were found to be the strengths of this approach. However, to determine the optimal configuration of eight parameters, a representative subset of the input point clouds needs to be selected and employed for testing. Since this initial trial-and-error procedure must be repeated for each new point cloud, it conflicts with the automatic nature of this method. Besides, there was no discussion related to the effect of the variable density in point cloud on the performance of the algorithms. In the future, it is also necessary to check the performance in terms of dip and dip directions of the detected planar regions.

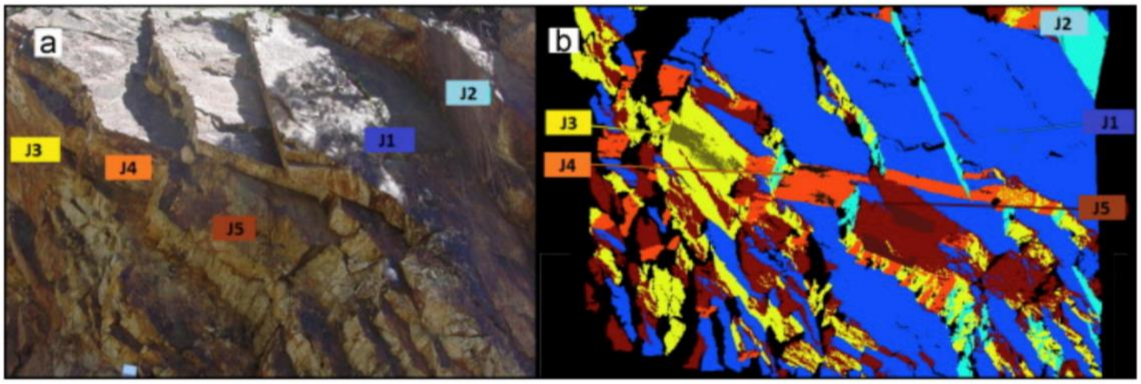

Figure 5 Identification of joints sets from 3D point cloud (Riquelme et al., 2014).

2.3.1.3 Other methods

The earliest attempts were made to extract joints and their orientation information using digital images of rock surfaces (Franklin et al., 1988, Kemeny and Post, 2003). Roncella and Forlani (2005) presented a multi-resolution Random Sample Consensus (RANSAC) (Fischler and Bolles, 1981) algorithm for extracting planar surfaces from DEMs of rock mass. It was one of the first approaches in this domain. The algorithm was slow and unstable. Also, the parameters were selected by trial-and-error. Ferrero et al. (2009a) presented a GUI software, namely RockScan, that lets the user select part of the image and segment discontinuity planes by iteratively running RANSAC for the selected points. Because of the iterative nature of the algorithm, it was computationally expensive to be run for the entire point cloud, and hence that is not practical. Further, there was no discussion on the values for different extraction parameters such as the threshold for RANSAC. Such analysis is also plagued with a bias as only the features considered important by the user are investigated. Also, its success depends highly on the skill and experience of the user.

Mah et al. (2011) considered each triangular element of a mesh 3D model as a plane, plotted their dip direction and dip as poles on a stereonet, and then used an automatic pole density contouring to determine the joint sets. However, the set orientation values were less accurate when compared with manual measurements. Gigli and Casagli (2011) presented a MATLAB (2020) tool, referred to as Diana, for semi-automatic extraction of joint sets and orientations from a given point cloud. Their approach was based on moving a cube through the entire point cloud and extracting least-square fitting planes inside the cubes. This resulted in the segmentation of the point cloud in planar regions. Then, these planar surfaces were merged based on their orientations and the distance from each other, resulting in individual discontinuity planes. The ability to resize the search cube helped extract even smaller features from point clouds with different resolutions. However, the values of parameters such as size of cube and angular and distance thresholds for planar segments merging depended on the point cloud resolution, noise and rock surface complexity. The computation time increased with a rise in the size of the point cloud. These reasons necessitate the manual collection of discontinuity parameters to complement the semi-automatic approach which makes the entire process comparable to manual field measurements in terms of time and cost.

Gomes et al. (2016) proposed a PCA-based algorithm that recursively divided the point cloud into subsets until they were planar or near-planar, as determined by user-specified thresholds. The algorithm was found to be accurate in terms of the orientation values of detected joint planes from rock mass point cloud. However, it either detected several planes or no planes on rough surfaces. Moreover, in case of rough rock faces and a low-resolution point cloud, the dip direction of detected planes could be inversed. A similar approach of recursive division of point cloud into smaller subsets (cells) of planar points is used in the FACETS plugin (Dewez et al., 2017) for CloudCompare software (CloudCompare, 2020). The adjacent cells are then merged back based on the similarity of their orientation values to form complete joint planes.

Aerial photogrammetry can generate photomosaic of rock mass slopes. Vasuki et al. (2014) presented an approach where discontinuity traces were detected from UAV images using phase congruency and phase symmetry algorithms complemented by user inputs. The third dimension of these 2D features was then computed using the DEM. RANSAC was used to compute the best fitted plane to the detected 3D points whereas the outliers or noise points were eliminated using the cutoff distance from the plane. The approach showed a good performance in terms of time and accuracy of computed orientations. However, the accuracy for the fault trace detection method was 79.8%, i.e., the algorithm couldn’t detect some fault lines represented by faint edges in the images. The user inputs help in perfectly capturing the geometry and location of the original fault trace lines. There is a need for testing the effectiveness of this approach on different rock textures and geometries.

2.3.2 Persistence and Trace length

Sturzenegger and Stead (2009b) determined the joints from 3D point clouds by manually fitting circular planes to individual rock mass discontinuities using the Polyworks software package (InnovMetric Software, 2020). The diameter of the fitted circular regions was assumed to be equal to the equivalent trace length for discontinuities. Sturzenegger and Stead (2009a) also pointed out the superiority in using 3D models for discontinuity persistence estimations in case of trace lengths exceeding 5 to 10 m and relatively higher benches. However, Sturzenegger et al. (2011) outlined the ground resolution of the model and the orientation of exposed rock mass as the major drawbacks that affect the accurate estimation of discontinuity persistence using this method.

Many different algorithms are discussed in the previous section for the detection of planar joint surfaces. Discontinuity persistence is basically the areal extent of these surfaces (ISRM, 1978). A polygon bounding the planar points for each discontinuity can be determined by applying convex hull algorithms (Preparata and Hong, 1977). Minimum and maximum persistence can be determined from the dimensions of this polygon (Gigli and Casagli, 2013).

When a rock face is investigated and mapped using UAVs, the discontinuity traces can also be extracted either manually or semi-automatically from the rock images collected by the UAV's image sensor and projected on the best-fitting plane for rock joints. The lengths of these projected lines could be used for the estimation of the persistence of discontinuities (Priest and Hudson, 1981; Reid and Harrison, 2000;Lemy and Hadjigeorgiou, 2003) . Each trace is associated with a discontinuity set based on the angle between the trace and the intersection lines of rock face plane and discontinuity set plane. A similar approach was also used by Kemeny et al. (2006). The results from the 2D approach indicated inconsistencies with the ground truth which could be attributed to the biased estimate of persistence for longer traces, practical difficulties during the field survey, or inaccuracies in fitted discontinuity set plane.

Some limitations of 2D approaches for a complete detection of the traces include the lack of points at the intersection of discontinuity planes and rock mass surfaces, division of a single trace into a number of broken fragments, and the generation of redundant segments of traces due to irregular rock surfaces (Li et al., 2016). Zhang et al. (2019) proposed to extract the trace lines from the 2D image of the rock face and then link the trace pixels with its corresponding points in a 3D point cloud. Linking pixels with point cloud data was completed using coordinate system conversion, and spatial trace coordination was computed using interpolation in triangulated point cloud data. The full trace length was equal to the Euclidean distance between the endpoints of the trace, and dip and dip direction could be computed by fitting a plane to trace points. The process of extracting trace lines from images is affected by occlusions, the position of the sun, shadows, weather conditions, rock type, color, and light conditions (Reid and Harrison, 2000).

Umili et al. (2013) presented a semi-automatic approach for extracting the traces from the Digital Surface Model (DSM) of the rock surfaces. The idea was to calculate the minimum and maximum principal curvature at each vertex. If the absolute value of any of these curvatures was more than a preset threshold for a vertex, then the vertex belonged to the convex or concave edges of a discontinuity. The vertices were then connected to create edge paths which are further segmented into edges and segments using the RANSAC. Finally, the segments were clustered into traces using the ISODATA algorithm (Ball and Hall, 1965). The mean trace length was calculated using either a circular window (Zhang and Einstein, 1998) or a circular scanline (Mauldon et al., 2001) sampling with varying radius. The time needed for trace detection using this method was similar to manual extraction from an orthophotograph. The parameters of the ISODATA algorithms such as the minimum number of members in each cluster, the maximum variance, and the minimum pairwise distance, are needed to be pre-specified. Furthermore, a sensitivity analysis of the curvature threshold values is essential to be performed to determine the range of optimal values.

Cao et al. (2017) identified edges of triangular elements in rock mass mesh as discontinuity traces based on the angle of intersection of corresponding triangular units. An edge was selected as a part of the trace if the corresponding intersecting angle was larger than a user-specified threshold. The resulting traces were post-processed to eliminate noises and redundancies. This is a simple method with a reasonable accuracy to automatically identify the discontinuity traces. The output of this method is dependent on the angular threshold value, mesh quality, and degree of weathering.

Li et al. (2019) presented an automatic method of extracting discontinuity traces from a 3D mesh model of rock mass face. It involved the detection and labeling of trace vertices as feature points using Normal Tensor Voting (Kim et al., 2009) and user-defined thresholds (Wang et al., 2012). The detected feature points were divided into groups with each group composed of adjacent points based on a common edge and difference of angle between normal and threshold. After this, trace segments which consisted of a continuous chain of feature points were estimated using a trace growth algorithm. This resulted in a number of trace segments that belonged to a single discontinuity trace. The segments belonging to one trace were connected using a similar growth algorithm but with different threshold values. Finally, each trace was made smooth and continuous by removing redundant trace segments through comparing their direction with the principal direction of the trace. The identified traces are depicted in Figure 6. This method is more robust for noisy point cloud data and artificial edges in the mesh induced by blasting. The accuracy of the output depends on the size of the mesh triangular element and the optimal values of the parameter. However, no evidence is given regarding the accuracy and running time of the presented algorithms.

Guo et al. (2018) proposed a curvature-based semi-automatic methodology for discontinuity traces extraction directly from 3D point clouds. In this method, normal vector for each point was calculated using PCA and later adjusted so that all the normals vectors point towards the same direction. Then, curvature information were calculated for each point based on 1D truncated Fourier series. Potential trace points were selected based on user-specified threshold for curvature. These potential points were further thinned through a curvature-weighted Laplacian smoothing technique. The thinned traced points were then linked to form final trace segments using a weighted line growing algorithm. The method resulted in more detailed and fast trace segment extraction from 3D point clouds as compared with the Compass plugin (Samuel T Thiele et al., 2017) in CloudCompare and the previously discussed method proposed by Li et al. (2019). However, the method couldn’t detect traces which intersect planar surfaces of rocks and differentiate between artificially induced traces (e.g., due to blasting) and natural traces. Later, Guo et al. (2019) proposed an automatic method for detecting discontinuity traces that used geometry as well as texture information from 3D points of rock mass. The texture and normals maps (2D) were generated from 3D point cloud by converting it into a mesh and then automatically unwrapping it using the Blender software. The texture map contained the RGB values of points, and the normal map included the normal vectors of points mapped to a 0 to 255 range. An edge detection technique, referred to as the multi-scale edge detector (MSEdge: A Multi-Scale Edge Chain Detector, 2017), was utilized to separately detect traces from the normal and texture maps. The traces from both maps were merged in order to get the final extracted traces, which were mapped backed to the corresponding 3D points. The method was effective in detecting traces on smooth surfaces of rocks. The addition of texture information in trace detection could also cause interference due to shadows or other noises which need to be eliminated separately.

Bolkas et al. (2018) further explored the application of 2D image edge detection techniques such as the space-frequency transforms for trace detection from Lidar data. They converted the 3D model into a 2D greyscale image by mapping the third dimension to a grey-scaled color. Such a conversion might cause loss of information from certain sub-horizontal or sub-vertical parts of rocks. The surface of 3D model was decomposed using wavelet function that gave multi-scale information of edges. The performance of contourlet (Do and Vetterli, 2005) and shearlet (Labate et al., 2005) transforms in automatic trace detection was found to be superior than other edge detection method. Also, the multi-scale feature approach helped to reduce noises from the data. The results were solely based on a 10-meter long section of entire 3D model. Further investigation needs to be conducted using larger point cloud datasets from different rock types. It should also be noted that in this research, transform parameters were determined using a trial-and-error approach.

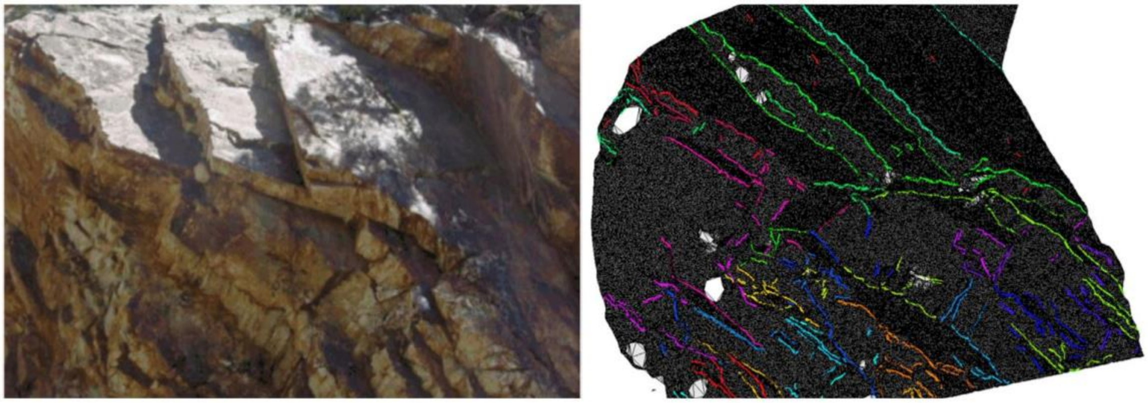

Figure 6 Discontinuity trace extraction modified after Li et al. (2016).

Riquelme et al. (2018) proposed a method for a semi-automatic extraction of the discontinuity persistence directly from a 3D point cloud. Initially, the point cloud of a rock mass was classified into discontinuity sets and clusters using an open-source software called the Discontinuity Set Extractor. Then, coplanar clusters were identified and merged into a single cluster. The points of each discontinuity set were extracted, and a coordinate system transformation based on the dip and dip direction of the parent discontinuity set was applied. Once this transformation was performed, the persistence in the dip and dip direction, the maximum persistence, and the area of persistence from the convex hull were estimated. The accuracy of this method depends on the correctness of the discontinuity set extraction from point cloud which is affected by the presence of noise, vegetation, or soil. In addition, the parameter K -which controls the sensitivity of coplanarity test- could also increase or decrease the measured persistence

2.3.3 Spacing

According to the ISRM (ISRM, 1978), the spacing has been defined as the perpendicular distance between two discontinuities which are adjacent to each other. There are mainly two approaches proposed in the literature for determining the spacing of discontinuities from 3D models of rock slopes. The first approach considers the pre-determined joint plane equations as the input. When the equations of the discontinuity surfaces are available for the discontinuity set, spacing can be derived by analyzing them in a 3D space. For each discontinuity set, the discontinuities are mostly parallel. Therefore, every discontinuity in the set is assigned the mean orientation of that set which makes them perfectly parallel to each other. Then, the spacing is calculated as the perpendicular distance between two adjacent discontinuities (Riquelme et al., 2015; Wichmann et al., 2019; Kong et al., 2020). Another proposed method in the same category is the use of a virtual cylinder of which base is a discontinuity plane as shown in Figure 7. All the discontinuity polygons which are intersected by the cylinder belong to the same set and the distance between these intersection points is used to calculate the mean, minimum, and maximum joint spacings (Gigli and Casagli, 2011). This approach showed a good accuracy; however, it should be tested on different rock types.

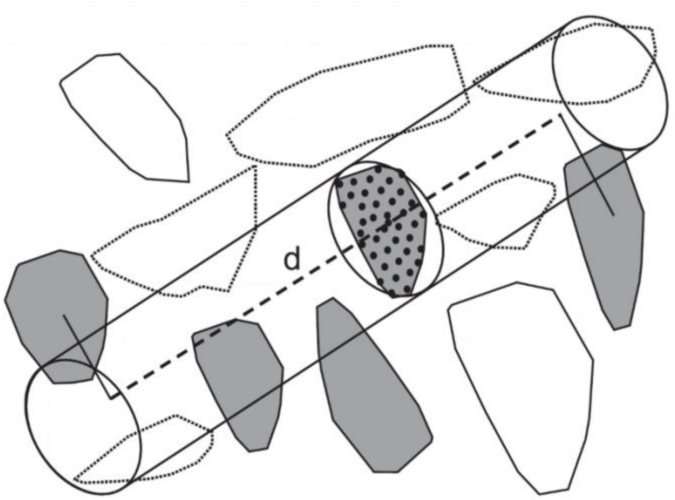

Figure 7 Virtual cylinder for spacing calculation (modified after Gigli and Casagli (2011))

In the second approach, the discontinuity traces projected in the 3D space are considered as the input. A clustering algorithm such as the K-means clustering is utilized to divide the projected traces into K groups. Then, a virtual scanline is created perpendicular to the average orientation of traces in each group, as shown in Figure 8. The average spacing is calculated for the set by taking into account the average lengths of line segments which are formed by an intersection between the scanline and the discontinuity traces (Li et al., 2019).

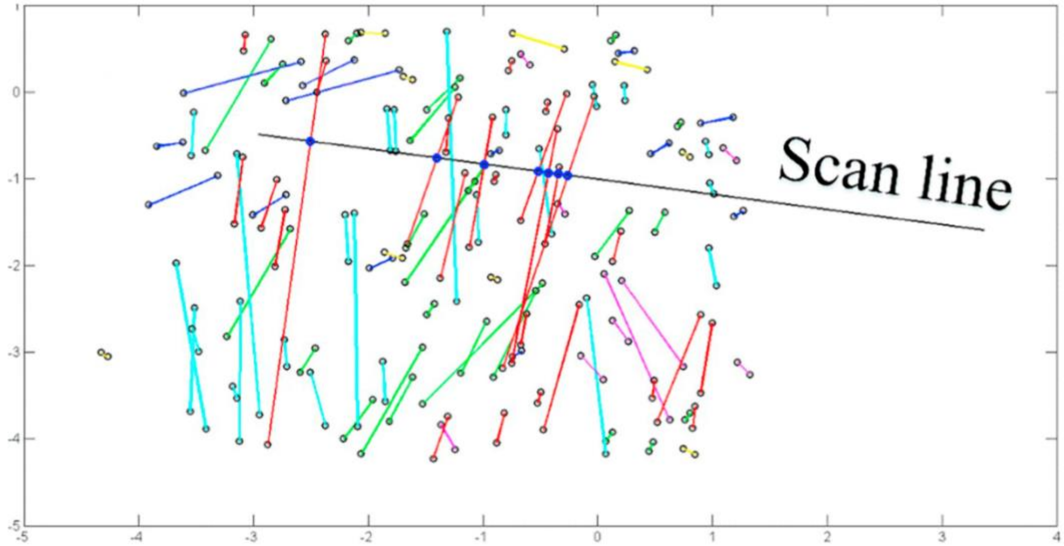

Figure 8 Virtual scanline plot perpendicular to extracted traces (Li et al., 2019).

2.3.4 Roughness

The roughness of a discontinuity is defined as the measure of irregularity and waviness of its surface relative to its best-fitted plane (ISRM, 1978). It plays a significant role in defining the shear strength of discontinuities and mechanical behavior of rock mass (Patton, 1966; Barton, 1973; Barton, 1976; Zare Naghadehi, 2015) (Zare et al., 2018). It can be measured from the point cloud of rock mass collected using a Laser scanner or photogrammetric methods. However, this way of measurement is affected by the presence of noise in data. Sturzenegger and Stead (2009a) presented two methods for quantifying roughness based on linear profiling, compass and disc-clinometer as suggested by the ISRM (ISRM, 1978). In the linear profiling method, the roughness is represented by a heat map depicting normal distance between the discontinuity surface and fitted plane. In the other method, square windows are created at random locations on the discontinuity surface, and then the orientation of the plane fitted to points inside each window is computed. The average orientation of these windows is represented as the roughness angle for the given discontinuity. These methods were implemented by Henk and Laux (2015) to automatically extract 2D and 3D roughness values of a given discontinuity from laser scanner data of an outcrop. The fitting of planes to the gridded points can be achieved using either the ordinary least square (OLS) regression (Fardin et al., 2004) or the orthogonal distance regression (Pollyea and Fairley, 2011) methods. In the case of noisy data, these methods might cause overestimation of the roughness values. The methods used meshing for creating linear profiles and hence depend on the characteristics of triangulation.

Another approach involves creating cross-sections on the surface of 3D models of rock mass and comparing them to Barton's standard Joint Roughness Coefficient (JRC) profiles (Barton and Choubey, 1977) to automatically estimate the coefficient for individual discontinuity set. The visual inspection is difficult and introduces a bias in the process. JRC can also be calculated using an equation developed by Tse and Cruden (Tse and Cruden, 1979):

$$JRC = 32.2 + 32.47 \log Z_2 \tag{1}$$

where Z_2 is the root mean square (Myers, 1962) of the first derivative of discontinuity profile which is given by:

$$Z_2 = \sqrt{\left(\frac{1}{L_n}\right) \sum_{i}^{N-1} \left(\frac{Z_{i+1} - Z_i}{x_{i+1} - x_i}\right)^2} \tag{2}$$

where $(x_i,\ z_i)$ and $(x_{i+1},\ z_{i+1})$ are the coordinates of consecutive points on the profile with Δx as the interval between them. N is the total number of points, and L_n is the considered profile length.

The profiles are created by intersecting a discontinuity surface with planes parallel to dip direction and perpendicular to it (Li et al., 2019). Haneberg (2007), on the other hand, used empirical equations developed by Maerz et al. (1990) for JRC and asperity angle i (Patton, 1966) estimation, as stated in Eq. (3-4).

$$JRC = c(R_p - 1) \tag{3}$$

$$i = \cos^{-1}\left(\frac{1}{R_p}\right) \tag{4}$$

where c is an empirical constant and R_p, a roughness profile index, defined as the ratio of the true length of profile surface to the projected length along the best-fit plane, given by Eq. (5).

$$R_p = \frac{\sum_{i=1}^{N} \sqrt{\Delta s^2 + (z_i - z_{i+1})^2}}{\Delta s(N-1)} \tag{5}$$

where Δs is the distance spacing between points.

It has also been found that there is no significant difference between the values of JRC computed using the above equations. However, the roughness measured using these methods is limited by the resolution of point cloud and accuracy of three-dimensional coordinates. It was found that the roughness calculated from the triangulated surface of the discontinuity (generated from a 3D point cloud of a terrestrial laser scanner) using the empirical roughness parameter developed by Grasselli et al. (2002) was more robust to noise than other roughness measures (Bitenc et al., 2015). Bitenc et al. (2019) proposed surface and range denoising methods for reducing the effect of noise and improving the estimated roughness values. The JRC is popular among engineers and researchers all over the world in the field of rock mechanics. Yong et al. (2018) proposed a non-visual method for comparing discontinuity linear profiles with Barton's standard profile. It involved representing the standard JRC and rock profiles into feature vectors based on the distribution of angular variation of the profiles. The comparison between two feature vectors was performed using the vectors similarity measures (VSM) such as Dice (Ye, 2012), Jaccard (Dharavath and Singh, 2016), and Cosine (Ye, 2015). The VSM-based JRC values were found to be in agreement with those of traditionally computed. However, the applicability of this method to a 3D discontinuity surface acquired using a laser scanner or photogrammetry is yet to be evaluated. Oppikofer et al. (2011) presented a method of calculating the JRC using the amplitude of the asperities along with the profile of the discontinuity surface. The equation is given as (Barton, 1982):

$$JRC = A\sqrt{0.2 * L^{-\log 80}} \tag{6}$$

where A is the maximum amplitude of asperities in mm, and L is the length of the profile in meters.

The JRC values estimated using this method are similar to those evaluated using visual comparison with Barton's standard profiles in case of a TLS-acquired rock mass point cloud.

The roughness of a discontinuity can also be measured by estimating the roughness angle of its surface. After the extraction of joint surfaces from the 3D point cloud, a sliding cube with varying dimensions can be moved on the surface. If the points inside the cube are more than the user-specified threshold, then a best-fitting plane is computed. The orientation value of the plane gives the discontinuity roughness angle for various cube sizes (Gigli and Casagli, 2011). The roughness angle decreases as the size of the cube increases showing the scale dependence of it. Ünlüsoy and Süzen (2019) proposed a new method of calculating JRC values of discontinuity surface profiles generated using a TLS scanner through comparing the area difference between the plot of power spectral density (PSD) functions of sample surface profiles with each of Barton's ten template profiles. The JRC range with the minimum area difference was primarily selected. An interpolation algorithm for computing the quantitative value of JRC was also proposed. This approach was found to be more accurate and reliable than the JRC estimations using conventional Z_2 formulae proposed by Tse and Cruden (1979), Tatone and Grasselli (2013) and Jang et al. (2014).

Cai et al. (2018) proposed another quantitative estimate of roughness entitled the index of roughness (I_R) which was more closely linked to the shear strength of discontinuities. This parameter was found to be relatively better in correlation with JRC than Z_2 and Graselli's method. Ge et al. (2015) proposed an index called brightness area percentage (BAP) to estimate the surface roughness of rock using its digital terrain model created from a TLS point cloud. It was basically defined as the percentage of bright triangles in the joint surface when light was irradiated using a virtual light source. The degree of brightness of tiny planes was directly related to their orientation (dip and dip direction) which is, in turn, related to their resistance during shear failure. This index was found to be capable of characterizing the anisotropy, scale effect, and interval effect features of roughness similar to fractal dimension (D) and Graselli's method. This method also requires the non-stationary component of the roughness to be removed before estimating the BAP.

Fardin et al. (2004) calculated the fractal dimensions, D and A, from the point cloud of the in-situ laser scanner using the roughness-length method (Malinverno, 1990). They presented a fast way of calculating primary roughness which governs the stability in high stressed fractured rock masses from a 3D point cloud. However, due to the limitations of scanning resolutions and the presence of noise, it was not capable of calculating the secondary roughness.

2D (Zhang et al., 2014a) and 3D (Zhang et al., 2017a) JRCs were also proposed to estimate the roughness of discontinuity profiles collected using a laser scanner. Hong et al. (2006) used the Specific Roughness Coefficient proposed by Belem et al. (2000) to estimate 3D roughness from the point cloud of rock surface. Also, Lai et al. (2014) used three curvature-based roughness measures namely curvature difference, curvature sampling, and curvature ratios mainly by exploring the use of curvature-based indices to estimate roughness from 3D mesh models of rock mass. The relationship between the shear resistance and these indices is not evident yet. Mostly, these indices were utilized for differentiating between planar and rough regions such as discontinuities, fractures, and bedding planes in a fast and efficient way.

2.3.5 Block size

The block size distribution of a rock mass is usually estimated by creating a 3D discontinuity model using rock mass characteristics like joint orientation, spacing, persistence, and others (Jafari et al., 2013). This is a statistical approach. As discussed in section 3.1-3.4, there are various algorithms available to extract these required parameters from 3D point clouds. These extracted parameters can be used for estimating block distributions in a rock mass point cloud. Mavrouli et al. (2015) estimated in-situ block size distribution using the formula:

$$v_b = s_1 \times s_2 \times s_3 \tag{7}$$

where v_b is the block volume in m^3, and s_i are the spacing values for intersecting joints.

Similarly, Wichmann et al. (2019) also computed block size from 3D point cloud data using a formula given by Cai et al. (2004):

$$v_b = \frac{s_1 \times s_2 \times s_3}{\sin \alpha_{12} \times \sin \alpha_{23} \times \sin \alpha_{13}} \tag{8}$$

where α_{ij} is the acute angle between two joint set normals.

However, these equations result in an underestimation of actual block sizes due to their simplified approach. Chen et al. (2017) presented an algorithm for automatic extraction of block size directly from the 3D rock mass point clouds generated by laser scanner or photogrammetry, as shown in Figure 9. The algorithm used joint planes extracted using the RANSAC Shape Detector (RSD) plugin developed by Schnabel et al. (2007), available in the Cloud Compare software. The outlines for the extracted planes were estimated using the concave hull algorithm (Rosen et al., 2014). Intersecting lines between non-parallel planes were found using geometrical equations. Two pairs of intersecting planes that share a common plane were used as an identification of the blocks. The final blocks were selected by using a combination of the Floodfill algorithm (Nosal, 2008) and the volumetric method. The blocks were assumed to be in the shape of symmetric parallelepipeds and their sizes were calculated from the volume of the tetrahedron formed by intersecting segments. Minimal deviations were found on comparing the results for this method with manual measurements using the Cloud Compare software. This method is applicable only to the exposed part of the blocks of a rock face. Some of the challenges to this method are irregular rock surfaces and complex shapes of blocks.

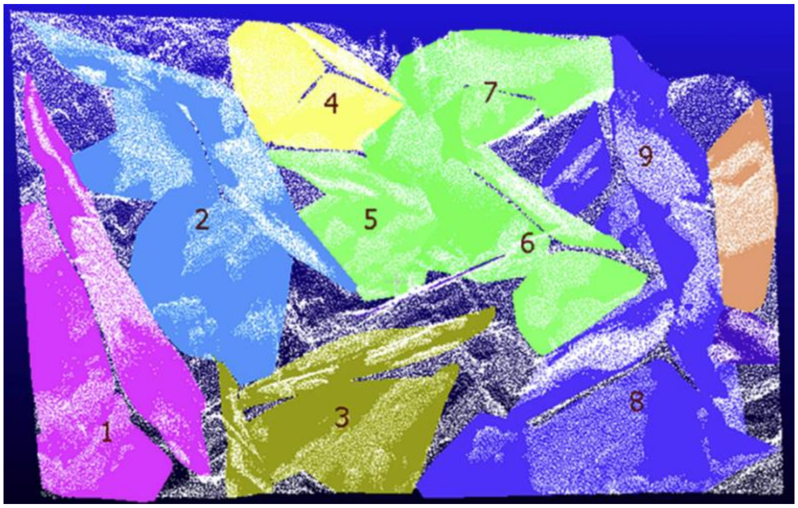

Figure 9 Blocks detection from a 3D point cloud (Chen et al., 2017).

2.4 Discussion

This paper presents a critical review of methodologies and algorithms in the literature for the automatic extraction of discontinuity characteristics including the joint set number, joint plane orientation, trace length, persistence, spacing, roughness, and blocks size, utilizing 3D models of the rock mass. The most popular 3D models used in the literature are point clouds and triangular meshes as shown in Figure 10. As there are numerous different approaches presented for each discontinuity characteristic, it is important to understand and analyze them to find some of the best methods in case of each characteristic. Therefore, in this paper, the methods have been categorized based on five parameters including joint sets and orientation, joint persistence, spacing, roughness, and block size. Each section contains a summary of the major studies conducted for automatic acquisition of those parameters. This review provides a comprehensive list of all the research conducted on this topic, which aims to help researchers find any possibility of improvement in the currently presented methods and direct future research. This survey is also important from the viewpoint of developing an automated rockfall risk analysis system similar to what performed by Riquelme et al. (2016). There are empirical indices for rockfall hazard in slopes such as CRHRS (Santi et al., 2009) and ROFRAQ (Alejano et al., 2008), that could be computed remotely given the discontinuity parameters are automatically extracted from the point cloud data of the slope.

Table 3 summarizes the strengths and drawbacks of each method presented for discontinuity parameters extraction. This table indicates that the clustering-based and region growing-based methods are popular for the computation of joint sets and orientations. It also highlights the major challenges in the extraction of discontinuity parameters from the different 3D models. In case of "joint set number and planes computation", the major challenges are higher computation times for clustering-based methods, and increased number of parameters and inaccurate joint boundary detection for region growing-based methods. As for the "Trace length or persistence," the curvature-based methods are found to be accurate and fast for discontinuity trace detections in rock mass point cloud or triangular meshes. These methods, supplemented with texture information, are demonstrated to detect traces in smooth rock surfaces as well. A major challenge identified in this approach is the error due to the presence of noise or bad lighting conditions which is introduced with the texture information. One of the ways of tackling this problem is to pre-process the texture information to eliminate the presence of noise with the application of state-of-the-art of shadow and weather effects removing algorithms. A review of various image enhancement and de-weathering techniques for outdoor images has been presented in Wahab et al. (2013). The selection of a method depends on the nature of noise such as fog, haze or rain.

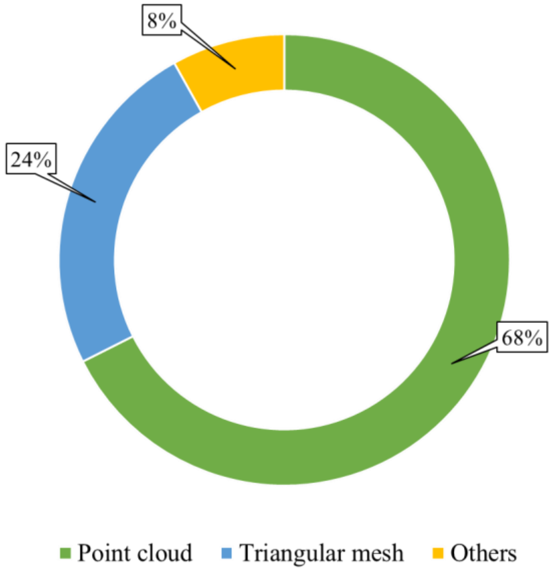

Figure 10 Percent-wise share of different 3D models used for discontinuity characterization.

The main factors which influence the application of these techniques in a real mine environment can be summarized as accuracy, number of parameters, running time, and robustness. The joint planes extraction is the first task in an automatic feature extraction effort. The analysis in Section 3.1 suggests that there is a trade-off between running time and number of parameters in the selection of a method for extracting joint planes from rock mass point cloud data. The region growing approach suggested by Hu et al. (2019) is fast and efficient in segmenting joints but it requires the determination of optimal values for a large number of parameters. On the other hand, if the running time is not an issue, then joint sets extraction using the CFSFDP and RANSAC, as presented by Kong et al. (2020), is the most appropriate method. It eliminates the human bias factor and automatically computes the number of joint sets and joint planes. In the case of a triangular mesh, K-means clustering with silhouette validity index proposed by Li et al. (2019) can be used.

If the joint planes are already extracted, the minimum and maximum persistence along dip and dip direction can be automatically computed using the convex hull algorithm, as presented by Riquelme et al. (2018). The Normal Tensor Voting with trace growth algorithm, discussed by Li et al. (2019), is found to be more robust in trace length computation from triangular meshes. In the case of 3D point clouds, the curvature-based method of Guo et al. (2018) is effective in terms of processing time and accuracy. If the rock surface is relatively smoother, then the multiscale edge chain detection method (Guo et al., 2019) which extracts traces from point cloud data based on texture and geometrical information is recommended.

The spacing can be calculated as the perpendicular distance between joints from the joint plane equations (Riquelme et al., 2015, Kong et al., 2020). In the case of a mesh, it can be determined using a virtual scanline and K-means clustering method where the value of K is equal to the number of joint sets detected in the first step (Li et al., 2019). As shown in Table 3 (the "Roughness" row), a number of different approaches have been proposed to quantify the 2D and 3D roughness values from point clouds, mesh, DEM, and images on both laboratory and large rock mass scales. However, few researchers have managed to integrate these methods into an automated process like what presented by Li et al. (2019). There is a need to develop novel algorithms to incorporate these roughness quantifications for automated characterization of discontinuity roughness. Another important point to note is that parameters such as spacing or roughness are usually not validated since their manual measurement involves significant errors leading to a lack of reliable ground truth data (Li et al., 2019).

Even though the computation time for block size using the joint planes intersection approach of Chen et al. (2017) is higher, it is currently the only method that directly computes the block size from the point cloud. There seems to be no algorithm available to approximate block size from triangular meshes. However, Eq. (7-8) can also be used with the spacing data calculated from a mesh. This shows that there is a need to develop faster algorithms for computing block sizes directly from the point cloud or mesh models.

The point cloud data resolution collected by laser scanners or aerial photogrammetry is currently on the scale of few millimeters. Given the size of open pit mines, any point cloud collected from a slope or highwall would include billions of points. The algorithms presented in the literature have high running times when the size of the point clouds are over one million. Given the significance of point clouds in discontinuity characterization (Figure 10) in the future, it is imperative to develop algorithms that can process large point clouds in reasonable times. This can be achieved by working towards algorithms that employ parallel computing to exploit the power of GPUs or by using machine learning (Lary et al., 2016). Determining the optimal parameters for algorithms in each case requires significant time and expertise. In some cases, it is possible that the time saved from not indulging in manual measurement is used in finding optimal parameters for the algorithms which render the computational algorithms insignificant.

The presence of noises such as vegetation and debris are an important challenge in the automated processing of 3D models of the rock mass. Many applications require a pre-processed point cloud which is free of vegetation, parts of the sky, or other noises. Recent developments in the field of artificial intelligence such as machine learning and deep learning can be used for solving these problems. Weidner et al. (2019) proposed a Random

Forest machine learning approach for automatic classification of TLS data into vegetation, talus, bedrock or other categories. Qi et al. (2017) showed that a 3D point cloud-based deep learning model can be employed for predicting the normals of points based on their neighboring points. Soilán et al. (2019) also used a deep learning network entitled the PointNet for automatic classification of an aerial point cloud collected using an ALS into vegetation, roads and other structures with 87% of accuracy. Similarly, Battulwar et al. (2020a) proposed a methodology for the application of the PointNet and DBSCAN for automated extraction of joint orientations in aerial photogrammetry-generated rock surfaces. This approach is shown to be better compared to DSE in terms of accuracy and time complexity for large point clouds.

Table 3 Approaches for rock mass discontinuity characterization from 3D models with strengths and limitations

Characteristic	Authors and year	Input type	Method(s)/Approach(es)	Strength(s)	Limitation(s)
Joint set number and planes computation	Roncella and Forlani, 2005 (Roncella and Forlani, 2005)	DEM	Multi-resolution RANSAC	Easy to implement	Not robust
	Slob et al., 2005 (Slob et al., 2005)	Triangular mesh	Fuzzy K-means clustering	Good accuracy	Need to specify K value
	Olariu et al., 2008 (Olariu et al., 2008b)	Point cloud	Multileader and K-means clustering	Acceptable accuracy No need to specify K value	Investigation into running time required
	Ferrero et al., 2009 (Ferrero et al., 2009b)	Point cloud	Iterative RANSAC	Easy to implement	Computationally expensive Suitable for smaller point cloud only
	Mah et al., 2011 (Mah et al., 2011)	Triangular mesh	3D pole density contouring	Easy to implement	Less accuracy
	Gigli and Casagli, 2011 (Gigli and Casagli, 2011)	Point cloud	Moving cube with least square fitting	Suitable for extracting small features	Cube size depends on density and other features of point cloud
	Voge et al., 2013 (Vöge et al., 2013)	Triangular mesh	Fuzzy K- means clustering	Results comparable to manual operation	Value of K specified by user
	Vasuki et al., 2014 (Vasuki et al., 2014)	Images and DEM	phase congruency and phase symmetry algorithms, RANSAC	Good time and accuracy performance	Fails to detect when edges are faint

	Assali et al., 2014 (Assali et al., 2014)	Point cloud	Spherical K-means clustering	Validation of clusters	Need to specify K value
	Riquelme et al., 2014 (Riquelme et al., 2014)	Point cloud	Kernel density estimation and DBSCAN	Good performance	Not recommended for large datasets or irregular surface Higher computation time
	Gomes et al. 2016 (Gomes et al., 2016)	Point cloud	PCA	Good accuracy	Detects multiple planes on rough rock surfaces
	Wang et al., 2016 (Wang et al., 2017)	Point cloud	Region growing	Lower computation time Good accuracy	Presence of some outlier planes
	Guo et al., 2017 (Guo et al., 2017)	Point cloud	Firefly algorithm and Fuzzy K-means clustering	No need to specify K value Lower computation time	Inaccurate classification of boundary points
	Zhang et al., 2018 (Zhang et al., 2018)	Digital Elevation Maps	ISODATA clustering; DEV	Good accuracy	Optimum parameters using sensitivity analysis No evidence of computation time
	Ge et al., 2018 (Ge et al., 2018)	Point cloud	Modified region growing	Lower computation time	Segmentation highly dependent on threshold
	Drews et al. 2018 (Drews et al., 2018)	Point cloud	Region growing	Good accuracy	Computational normal vector estimation
	Xiaojun et al., 2019 (Li et al., 2019)	Triangular mesh	K- means clustering with silhouette validity index	No need to specify K value	Longer running time Not robust to weathering
	Hu et al., 2019 (Hu et al., 2019)	Point cloud	Region growing	No clustering Very fast and efficient Voxelized approach, parallel computing possible	High number of parameters
	Kong et al., 2020 (Kong et al., 2020)	Point cloud	CFSFDP; RANSAC	No need to specify K value More accurate	Longer running time
Trace length or	Gigli and Casagli, 2011 (Gigli and Casagli, 2011)	Point cloud	Convex hull algorithm	Calculation of minimum and maximum persistence	Need to find joint planes

	Umili et al., 2013 (Umili et al., 2013)	DSM	Principal curvature with ISODATA algorithm	Semi-automatic approach Direct extraction	Longer processing time Optimal parameters not available
	Li et al., 2016 (Li et al., 2016)	Triangular mesh	Normal Tensor Voting with trace growth algorithm	Direct extraction More robust	No evidence of running time Output depends on mesh resolution
	Cao et al., 2017 (Cao et al., 2017)	Triangular mesh	Intersection angle between planes	Direct extraction	Affected by weathering, bedding in data
	Riquelme et al., 2018 (Riquelme et al., 2018)	Point cloud	Coordinate system transformation with convex hull algorithm	Calculation of minimum and maximum persistence in dip and dip direction	Needs joint planes identified Accuracy depends on presence of noise, vegetation in data
	Guo et al., 2018 (Guo et al., 2018)	Point cloud	Curvature-based method	Detailed extraction Fast processing	Neglects traces on smooth surfaces Detect artificial traces also
	Bolkas et al. 2018 (Bolkas et al., 2018)	Point cloud	Space-Frequency transforms	Good accuracy Eliminated noise	Trial-and-error approach
	Zhang et al., 2019 (Zhang et al., 2019)	Images and point cloud	Trace projection in 3D	No need to find joint planes	Typical image extraction problem like weather, occlusions
	Guo et al., 2019 (Guo et al., 2019)	Point cloud	Multiscale edge chain detection	Includes texture information Detect traces on smooth rock surface	Interference due to shadows or other noise in texture information Unwrapping of mesh is required
Spacing	Gigli and Casagli, 2011 (Gigli and Casagli, 2011)	Point cloud	Virtual cylinder intersection	Good accuracy	Neglects joint planes which do not intersect the cylinder
	Xiaojun et al., 2019 (Li et al., 2019)	Triangular mesh	K- means clustering with virtual scanline	Method is similar to actual field measurement method	Smaller traces are neglected by the scanline No discussion about accuracy of measurement

	Riquelme et al., 2015 (Riquelme et al., 2015); Kong et al., 2020 (Kong et al., 2020)	Point cloud	Perpendicular distance between extracted joint planes	Easy to calculate from joint plane equations	Expertise in rock mechanic is required to get optimum results
Roughness	Fardin et al., 2004 (Fardin et al., 2004)	Point cloud	Fractal parameters D and A	Fast computation of primary roughness	Needs uniform density point cloud
	Haneberg, 2008 (Haneberg, 2008)	Triangular mesh	JRC Eq. 3-5	Eliminated biased measurements	Accuracy is limited by resolution and positional accuracy of 3D point cloud
	Oppikofer et al., 2011 (Oppikofer et al., 2011)	Triangular mesh	Amplitude of asperities	Results in agreement with JRC values using Barton's profiles	Not consistent with centimeter-scale insitu measurements
	Gigli and Casagli, 2011 (Gigli and Casagli, 2011)	Point cloud	Roughness angle using best fitting plane	Approach is similar to ISRM suggested method	Low accuracy of point cloud could lead to overestimation
	Lai et al., 2014 (Lai et al., 2014)	Triangular mesh	Curvature based roughness	Efficient for differentiating between planar and rough surface	Relationship to shear strength to be explored
	Ge et al., 2015 (Ge et al., 2015)	Point cloud; Image	Brightness Area Percentage	Easy to calculate	Non-stationary component needs to be removed first
	Zhang et al., 2015 (Zhang et al., 2014b)	Point cloud	2D JRC	Takes direction and amplitude into consideration	Constants need to be found using curve-fitting
	Zhang et al., 2017 (Zhang et al., 2017b)	Point cloud	3D JRC	Considers the 3D JRC profiles	Further investigation of directional variation required
	Yong et al., 2018 (Yong et al., 2018)	Triangular mesh	Vector Similarity Measure	Eliminated bias Values in agreement with Barton's profiles	Evaluation using TLS data required
	Cai et al., 2018 (Cai et al., 2018)	Point cloud/Mesh	Index of Roughness	Closely related to shear strength of discontinuity Higher correlation with JRC	Correlation to shear strength need to be further studied

	Unlusoy and Suzen, 2019 (Ünlüsoy and Süzen, 2019)	Point cloud	Power Spectral Density (PSD)	Better precision Reliability	Small values of JRC
	Xiaojun et al., 2019 (Li et al., 2019)	Triangular Mesh	JRC Eq. 1	Objective method	No validation conducted
Blocks size	Chen et al., 2017 (Chen et al., 2017)	Point cloud	Using Intersecting joint planes	Automatic calculation directly from point cloud More accurate	Not robust to irregular surfaces or complex shape rock mass Only applicable for exposed blocks Long concave hull computation time
	Mavrouli et al., 2014 (Mavrouli et al., 2015) ; Wichmann et al., 2019 (Wichmann et al., 2019)	Point cloud	Eq. 7-8	Easy to calculate from joint spacing and orientation	Overestimation of block size Manual measurement required

2.5 Conclusions

Automatic or semi-automatic extraction of discontinuity parameters from the 3D models of rock mass has been a focus for researchers in the past two decades. This paper categorizes the major previous studies in this domain based on five parameters including joint sets and orientation, joint persistence, spacing, roughness, and block size. For each parameter, the presented algorithms are briefly summarized, and their strengths and drawbacks are analysed. This is a first comprehensive review presented on this topic. The possibilities of improvement in the existing methods have been identified, which will help the engineering geology and rock mechanics communities direct future research in optimal ways. Some of the most suitable methods for discontinuity characteristics have been highlighted and recommended as follows: the region growing approach for joint set orientation, the convex hull algorithm for joint persistence, the joint plane equations for spacing, and the joint planes intersection approach for roughness and block size estimation. The overall challenges in developing an automated methodology for discontinuity characterization have also been discussed. The voxel-based region growing approach has been found to outperform conventional statistical analysis-based methods for joint plane estimation in terms of computation time, though it needs to be explored further. Other discontinuity parameters such as wall strength, aperture, filling, and seepage have not been considered in this review. Remote measurement techniques of discontinuities should also be further developed by using different sensors such thermal (Vivas et al., 2015) or hyperspectral imaging (Kurz et al., 2011).

Furthermore, this review is limited to the measurement of discontinuity characteristics exposed on the surface of the rock mass. A complete 3D measurement of parameters such as persistence can only be achieved by undertaking subsurface investigations (e.g., using ground-penetrating radar (GPR) surveys; see Longoni et al. (2012), where the discontinuity planes extracted using GPR could be used to construct the actual model of the rock mass). The application of newly developed 3D point cloud-based deep learning models as PointNet and PointNet++ needs to be explored for joint characterization from 3D models. These techniques can be utilized for tasks such as the classification of joints surfaces in rock mass 3D point clouds.

CHAPTER 3 : DATA COLLECTION

3.1 Introduction

Unparalleled advancement has been witnessed in the field of UAVs in the past decade. They have been successfully incorporated into modern mining operations throughout the world. The increasing availability of cost-effective drones and skilled personnel have led to their use for multiple applications in open-pit mining operations. UAV technology is the perfect tool for mining companies due to the vast and remote nature of operations and their hazardous environment. As a result, many companies have already been using drones for surveying, volumetric analyses, and visual inspection of inaccessible locations (e.g., Rio Tinto (“Life as a drone pilot.,” 2020), BHP Billiton (Knox, 2017), Newmont (Newmont, 2017), and Barrick (Airware, 2018)). Other applications such as designed vs. actual survey of ramps and benches (Tournaire and Paparoditis, 2009), detecting the height of safety berms, blast fragmentation analysis and determining the accuracy of drill holes (Valencia et al., 2019), and vegetation (Yan et al., 2019) and surface moisture (Hasan et al., 2014) monitoring have been presented in the literature. Completing all of these tasks with aerial missions can result in significant benefits for mining operations in terms of time and resource utilization; however, available technologies for using drone images by application of artificial intelligence, computer vision, and machine learning algorithms have not yet been developed to their highest capacities. This is due to the lack of sufficient resolution in acquired aerial images in most cases. For example, detection of tension cracks and monitoring their evolution remains a critical problem for geotechnical engineers at open-pit mines despite all of the advances in slope monitoring techniques. Current slope monitoring practices rely primarily on instrumentation such as inclinometers, prisms, crack extensometers, or remote sensing technologies like LiDAR and slope stability radar (SSR); however, instrumentation is an unsafe and laborious exercise and remote sensors like SSR are not able to directly visualize cracks regardless of being a state-of-the-art slope movement monitoring technology. Further, capital and installation costs associated with an SSR system are unaffordable for small- to medium-scale mining operations (Hannon, 2007). It seems that UAV imaging would be an ideal tool for automation of this process; however, tension cracks are usually narrow geometrical features that are not detectable on low resolution images usually taken from a constant, high altitude (around 400 feet) by popular drones currently on the market. In this regard, the Mining Automation Lab at the University of Nevada, Reno conducted a project (supported by the National Institute for Occupational Safety and Health, NIOSH) to use UAVs for high-resolution imaging and to develop state-of-the-art machine learning techniques for automated identification and characterization of cracks. The technology can be used as an early-warning system that alerts geotechnical engineers about the location of new cracks, and subsequently the potential for related failures so that necessary safety steps can be executed to avoid them (Battulwar et al., 2021).

This paper describes a part of the project wherein a practical setup was developed to use popular, cost-effective drones for systematic generation of high-resolution images and 3D models for large open-pit mines. The setup consists of a ground station mobile application that assists the user with designing an imaging mission. It generates a series of flying waypoints at a constant, short distance above the ground to take high-resolution images. Images are processed by photogrammetry software to generate three-dimensional

(3D) models of the pit, which are used for detecting and monitoring tension cracks (Winkelmaier et al., 2020).

3.2 High-resolution Imaging

3.2.1 Photogrammetry

The science of obtaining 3D information on physical world objects from their digital photographs is referred to as photogrammetry (Abe et al., 2010). Mathematical relationships for flight planning and estimating parameters of the flight for taking overlapping photos of an area are discussed in the literature [13, 14]. Photogrammetry has been a fundamental approach for generating required 3D models from overlapping images in many applications. A methodology for generating a high-resolution orthomosaic of an active landslide area using a micro UAV fitted with an image sensor was demonstrated by Torres et al. (Torres et al., 2016). The 3D form of a scene can also be estimated from a series of 2D digital images using Structure from Motion (SfM) (Hartley and Zisserman, 2004). Lucieer et al. (Lucieer et al., 2011) provided an example showing the use of SfM where a 3D point cloud of topography in a real-world coordinate system was generated with an accuracy of 3 cm from overlapping UAV photographs of the terrain. In the field of agriculture, where financial and technical challenges of satellite sensors exist, photogrammetry is used to derive quantitative remote sensing models on crop stress and water spills using UAVs equipped with standard thermal and multispectral imaging sensors guided by autonomous GPS navigation (Li et al., 2020).

Agisoft PhotoScan (Agisoft, 2020) is used in this project for photogrammetric processing of images and generating dense point clouds, digital elevations maps (DEM), georeferenced orthomosaics, and contours. Processing steps for creating these items from overlapping images collected by UAVs are shown in Figure 11. A computer server equipped with eight NVIDIA Ti 2080 graphic cards, 256 GB RAM memory, dual 16-core 2.1 GHz CPUs, and 30 TB SSD storage is used in this research to process photogrammetry calculations in a timely manner.

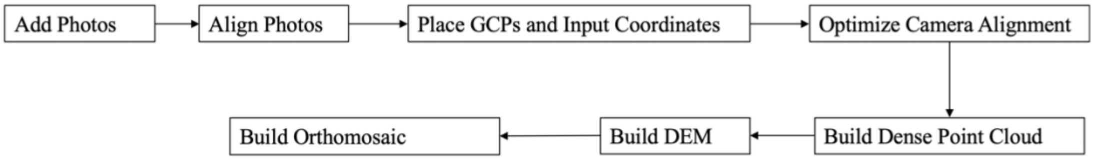

Figure 11 Workflow in Agisoft PhotoScan software.

Although photos are automatically geotagged by the UAV and contain latitude, longitude, and elevation of the point where the photo has been taken in its metadata, there are substantial errors in the geo-location information of images due to inaccuracy of the drone’s GPS. These errors need to be minimized in order to create an accurate geo-referenced 3D model of the mine. Ground control points (large visual signs on the ground with surveyed coordinates) are used to improve the accuracy of generated models in a global coordinate system.

3.2.2 Flying Challenges in an Open-pit Mine Environment

It is crucial to fly over a surface mine in an optimized way due to the mine’s huge scale and the limited capacity of batteries on board drones. During a flight mission, the UAV takes off from a starting point (called Home), visits and takes photos at locations (called waypoints), and returns Home. Waypoints are at a constant distance above the ground (*e.g.*; 30 m for 1 cm/pixel resolution with DJI Mavic drone) with sufficient forward and lateral overlapping among images (around 80%). Hence, thousands of images need to be taken in a typical mine mapping mission.

Due to the relatively low altitude of flights above the ground, the required resolution, and the fact that the terrain of an open-pit changes continuously, common sources of global terrain models such as the Space Shuttle Radar Topography Mission (SRTM) (USGS, 2018) , ASTER Global Digital Elevation Model (NASA, 2012), or JAXA’s Global ALOS 3D World (JAXA, 1997) would not be applicable to develop a flight mission for an open-pit mine. Furthermore, these terrain models are of low resolution (30 m/pixel) and were generated many years ago. Two feasible options are installation of LiDAR range finder sensors on the drone or importing a previously generated high-quality terrain map. The latter is selected to maintain practicality of missions on simple drones like Mavic and Phantom. The imported terrain can be a mine Toe-Crest computer-aided design (CAD) model or a DEM resulting from photogrammetry.

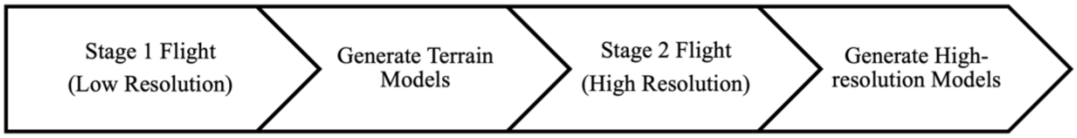

Figure 12 Workflow of the proposed approach in this research.

Figure 12 depicts the developed procedure for generating high-resolution maps for an open-pit mine. There are two stages of flights in this process. First, an area mapping flight is conducted at the highest permitted altitude (400 m) by designing a grid mission and using ground control points (GCPs). Then, photogrammetry is used to create the updated terrain model of the mine. Since the geometry of benches and walls change constantly in an open-pit mine, this stage needs to be repeated periodically. Second, the surface terrain obtained in the first stage is used as an input to fly the drone precisely at a required elevation above an area of interest to generate high-resolution models of that area. In both flight stages, each waypoint is defined based on forward and side overlap required between images. Unlike the constant flight altitude in Stage 1, elevations of waypoints in Stage 2 are set at a constant distance above the mine terrain model, which is derived from Stage 1. This distance is determined based on the required ground resolution and camera specifications. Another difference between the two flights is that Stage 1 always follows a parallel path while Stage 2 follows an optimized path that will be explained later in the paper.

3.2.3 Ground Station Mobile Application

Development of the operating procedure for the Android flight control system is explained in this section. While Android Studio V.3.1.4 has been used as the developing environment, DJI Android SDK (DJI, 2020b) has been utilized for interacting with and sending flight commands to the UAV's flight controller. Further, Google Maps' API platform (Google, 2020) has been an interface for flight planning and navigation. Updated versions of all three kits have been implemented in JAVA.

Figure 13 A view of DJI Mavic Pro.

DJI Mavic Pro (Figure 13) has been used as a test platform for conducting test flights using the application during development and testing stages. It is a commercially available quadcopter fitted with an image sensor. Table 4 lists the main specifications for this UAV.

It has a high-quality image sensor for capturing aerial imagery and videos and it automatically geotags these images with the WGS 84 coordinate system, which aides in photogrammetric processing of data.

Table 4 DJI Mavic Pro specifications (DJI, 2020a).

Flight Time	27 min	Image	4000 x 3000 px
Navigation	GPS + GLONASS	Weight	734 g
Battery	3830 mAh, 11.4 v	Charging Time	45 mins
Max. Altitude	120 m	Max. Speed	40 mph

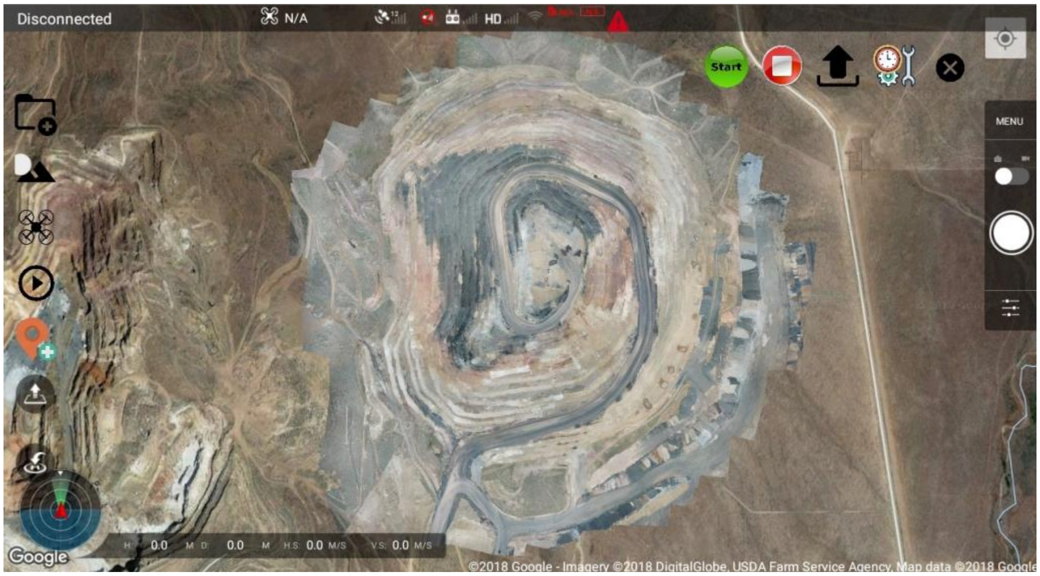

Figure 14 Graphical User Interface of the designed application with updated mine terrain.

Figure 14 depicts the flight planning interface of the designed mobile application. It can import 3D terrain models generated using photogrammetry. As shown in Figure 14, the most up-to-date 3D model of the mine has been overlaid as a reference for the user on Google Maps, which initially did not have a trace of on-going mining operations. Subsequently, the user can plan and edit UAV mapping missions based on the imported terrain. Once flight parameters are input by the user, the application uploads the path to the drone's flight controller, which will execute the mission and bring the drone back to its initial launch position. Once the drone lands, the mobile application automatically downloads captured images and uploads them to the project server where they will be processed for the next stages of the project.

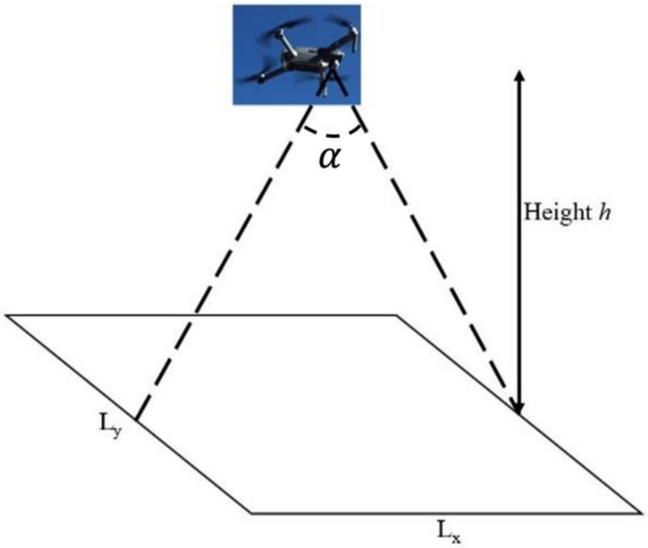

Figure 15 Area projected by a camera with angle of view α flying at altitude h (i.e.; area of ground that is visible through the camera at a particular position and orientation).

The size (L_x, L_y,) of the ground image taken by the UAV flying at height h above the ground depends on h and the size of the image sensor, as shown in Figure 15 (Suziedelyte Visockiene et al., 2016) (Di Franco and Buttazzo, 2016). It can be computed as follows:

$$L_x = 2h\,tan\frac{\alpha}{2} \tag{9}$$

$$L_y = \frac{L_x}{\rho} \tag{10}$$

where L_x is the width of the image on the ground, L_y is the length of the image on the ground, α is the angle of view of the camera, ρ is the aspect ratio ($\rho\ = \frac{I_x}{I_y}$), I_x is the width of the image expressed in pixels, and I_y is the length of the image expressed in pixels.

In addition, Ground Sampling Distance (GSD), which is the distance between centers of two pixels of an image measured on the ground is given by Equation (11).

$$GSD = \frac{L_x}{I_x} = \frac{2h\, tan\frac{\alpha}{2}}{I_x} \tag{11}$$

From Equation (9), it can be concluded that the size of the image on the ground is directly proportional to the altitude of the UAV above the ground. Another important parameter is the proportion of overlapping between images along the length and width of the area. The industry-wide recommendation is to have 85% forward (length) overlap and 70% side (width) overlap (PIX4D, 2018). The distance between two overlapping images along the length and the width of an area of interest (Figure 16) can be determined as:

$$a = d \times \left(1 - \frac{q}{100}\right) \tag{12}$$

$$b = d \times \left(1 - \frac{p}{100}\right) \tag{13}$$

where a is distance between two images along the width of the mapping area, b is distance between two images along the length of the mapping area, d is size of the image on the ground, p is percentage of forward overlap, and q is percentage of side overlap.

3.2.4 Validation of Images and Models

The developed application has been validated by conducting a case study at the East Keystone Trail Head near Reno, Nevada. The objective of this experiment is to validate the ability of the software to generate high-resolution terrain maps of the area by following the terrain at constant altitude. The East Keystone trail is a suitable site for this experiment because it has a hilly terrain and is sparsely populated. GCPs were laid out over the approximately 0.09 km^2 area as shown in Figure 17a to minimize errors in generated 3D models. X-marks are made with survey-grade spray paint that has a bright color like orange

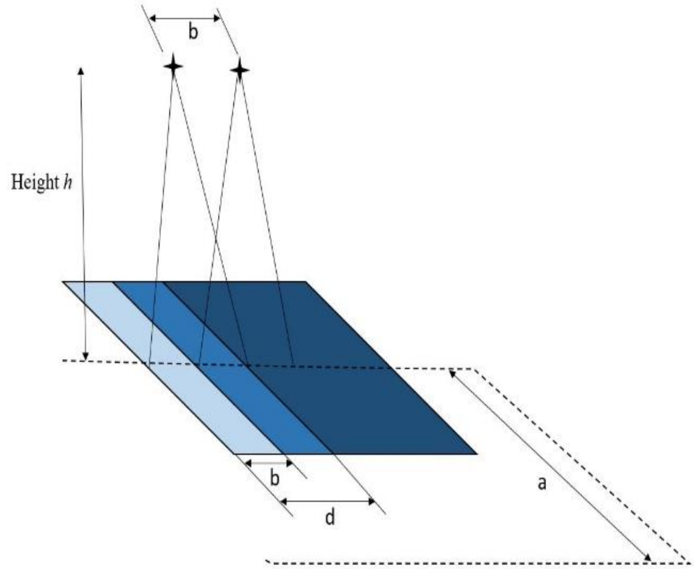

Figure 16 Flight parameters forward distance b and side distance a between drone waypoints when flying at altitude h.

as shown in Figure 17b. The size of each X-mark is 1 m × 1 m. A wooden peg was installed at the center of the X-mark to be used as a survey point. In order to easily spot GCPs, survey stakes with ribbons as shown in Figure 17c, were placed near them. An integrated global navigation satellite system (GNSS) was used for surveying. This unit is comprised of a Trimble R8 as the receiver and a Trimble TSC3 as the data collector.

(a) (b) (c)

*Figure 17 (**a**) Ground control points (GCPs) at Keystone Trailhead; (**b**) X-mark GCP; (**c**) Survey stake.*

Placement and surveying of GCPs took around 1.5 hours. Once this was completed, the Stage 1 flight was conducted over the area with a DJI Phantom 4 Pro UAV. Collected images from the flight were processed using PhotoScan to generate a point cloud, a DEM, and an orthomosaic of the area. The orthomosaic and the DEM were then imported into the designed mobile application to plan and execute the Stage 2 flight with the terrain-awareness feature enabled for an area of interest (Battulwar, 2018). Characteristics for Stage 1 and Stage 2 flights are shown in Table 5, and the estimated UAV path for the Stage 2 flight is depicted by the red polyline in Figure 18. The altitude for the Stage 2 flight was set to a lower value of 36.5 m compared to 60 m for the Stage 1 flight to generate sub-millimeter resolution models. It can be observed in Figure 18 that the Stage 1 generated terrain map of the test site has been overlaid on Google Maps to aid the user in flight planning. Since the terrain-awareness feature was enabled, flight planning was based on altitude values derived from the generated DEM of the area. DJI Mavic Pro was used for this test flight. The Android application ran on an Asus Zenpad with 1.3 GHz CPU and 2 GB RAM.

This is a significant advantage because the Mavic Pro UAV is able to generate higher resolution models even though its imaging sensor is smaller than that for the Phantom 4 Pro UAV (20 MP resolution). The resolution of 6.3 mm/pix is reasonably sufficient for detecting tension cracks and measuring drill hole accuracy from an orthomosaic. In this case study, the considered area was relatively smaller than that for an actual mine. It can be observed from Table 5 that if the area of interest increases, the number of images taken and the flight time required to do so rises significantly. With less flight time available for each battery, it is a major challenge to manage UAV battery power consumption for mapping mining operations. For such missions, it is crucial to calculate the number of batteries required beforehand and also to charge batteries simultaneously during the mission using an on-field power source like a car battery. This problem is addressed in the next section by developing an optimization algorithm to map a greater area using a given UAV with the same amount of battery power or map the same area with less battery consumption.

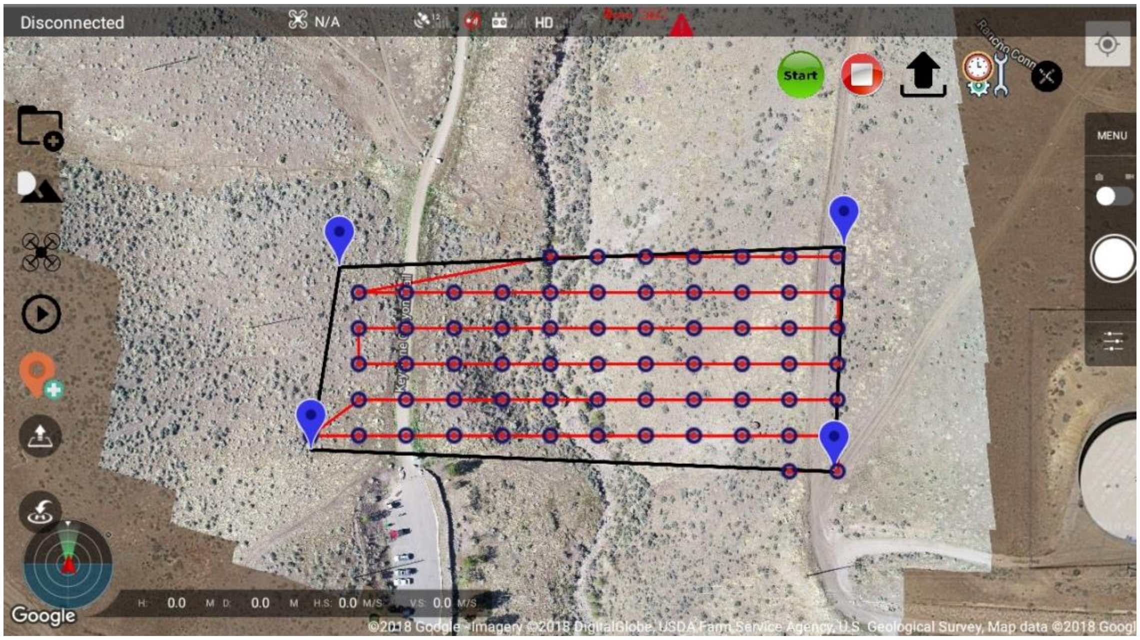

Figure 18 High-resolution flight planning using the developed application.

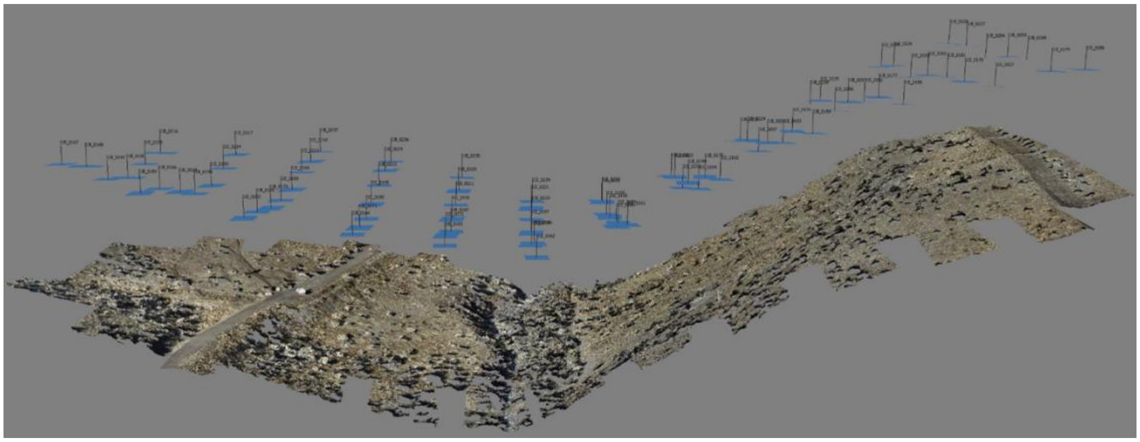

Figure 19 Generated point cloud and position of images captured during Stage 2 flight.

Table 5 Flight parameters for Stage 1and Stage 2 flight test.

Parameters	**Stage 1**	**Stage 2**	**Parameters**	**Stage 1**	**Stage 2**
Altitude (AGL)	60 m	36.5 m	Forward Overlap	80	80
Area	0.0658 km^2	0.0104 km^2	Side Overlap	80	80

Max. Speed	7 m/s	5 m/s	Terrain-awareness	No	Yes
Flight Time	15 min	7 min	No. of Images	119	84

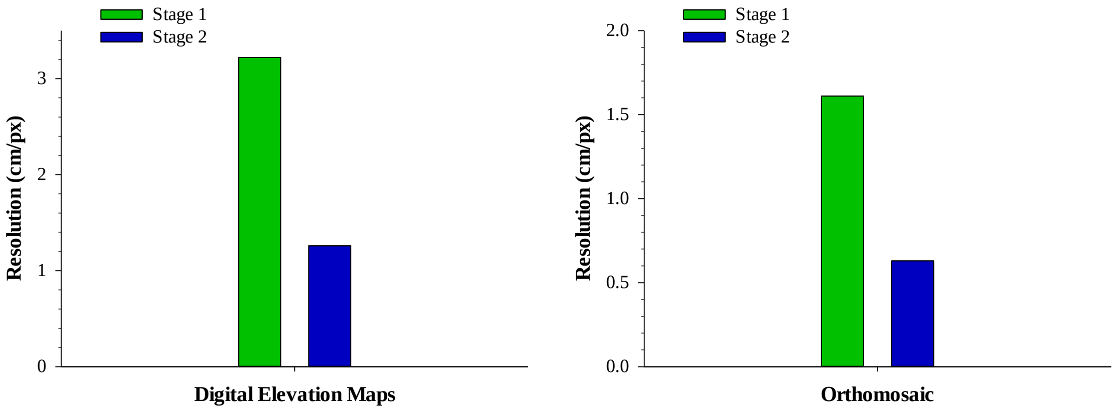

(**a**) (**b**)

*Figure 20 Comparison of (**a**) DEM and (**b**) orthomosaic resolutions for Stage 1 and Stage 2 flights.*

3.3 Materials and Methods

An optimized flying mission can be defined as completing the flight with minimum power consumption and/or at the shortest travel distance, which can be formulated as a classical Traveling Salesman Problem (TSP). In a TSP, the salesman has to visit all cities (represented by nodes on a graph) in a tour such that each city is visited exactly once and the total distance traveled is minimized (Hussain et al., 2017). This is a challenging, nondeterministic, polynomial-time problem, which can be solved by different approaches such as simulated annealing (Kirkpatrick and Toulouse, 1985), neural networks (Bhide et al., 1993), and Tabu search (Glover, 1990). Integer linear programming methods have also been proposed with ways to eliminate sub tours (Miller et al., 1960); however, integer programming is not a suitable choice when the number of cities increases to more than one hundred. An application of a genetic algorithm for solving a 3D variation of the TSP has been presented by Meneses et al. (Meneses et al., 2017).

In general, the speed of reaching a solution can be increased by using metaheuristics for estimating the initial solution in cases with evolutionary algorithms. A 3D path planning approach using genetic algorithms for multiple drones has been presented by Ergezer and Leblebicioglu (Ergezer and Leblebicioglu, 2013). They proposed a solution that plans drone flights through some desired areas while avoiding other undesired areas. Besada-Portas et al. (Besada-Portas et al., 2010) designed an evolutionary trajectory for multiple UAVs in a military environment that can work online as well as offline. It includes constraints based on a drone’s dynamics and environment with the goal of minimizing the risk to the UAV from enemy’s missiles. Pehlivanoglu and Hacioglu (Pehlivanoglu and Hacioglu, 2007) proposed a vibrational mutation operator designed to improve the speed of path planning using a genetic algorithm. The advantage of such an algorithm is that when the solution is unstable/jammed in local minima, it helps to remove the repetitive iteration.

3.3.1 Experimental Study

A power consumption model for the UAV is necessary to optimize drone battery performance. Experiments were conducted to study battery performance when the drone flies in different directions and encounters varying wind speeds.

The power consumption model for a UAV can be calculated in one of two ways, known as White-box model and Black-box model approaches. A microscopic behavior model for a drone can be derived by conducting a comprehensive study of motor performance, aerodynamic environment, and battery systems. Such an approach is called the White-box model approach. A significant number of aerodynamic parameters relating to the body of the drone and sophisticated experimental setups are required in this method, and the method is specific/limited to the particular drone (Kim et al., 2013). In the Black-box model, a multivariate regression model for drone power consumption is derived by conducting empirical studies (Cappiello et al., 2002). This model is more flexible and acceptable for flight mission optimization. Also, parameters in this approach are easier to measure; hence, it is a more desirable approach. Since most mining companies use commercial drones, this approach is more suitable for mining applications because these drones do not come with development kits (Tseng et al., 2017).

In this project, a statistical approach was used for deriving the energy consumption model for the DJI Mavic Pro. In a UAV, powering motors to lift the UAV's body consumes a significant portion of total available energy. The rest is consumed in controlling the UAV's motion in different directions. An experimental analysis was performed to study on-board battery power consumption during the drone's movements in different directions while encountering varying wind speeds. A drone's movements can be categorized as hovering, horizontal, and vertical motion. Each drone flight is a combination of these three motion types. To measure the rate of power consumption during these motions, multiple experiments were conducted. In each experiment, the drone was programmed to ascend and descent repeatedly at its maximum speed in a vertical direction. Then, it is moved horizontally at maximum speed without altering its altitude. DJI Mavic Pro was used as a test platform for these experiments. The UAV's speed relative to the ground in vertical and horizontal directions, battery power, and barometers readings are recorded for each experiment from telemetry data. Figure 21 depicts recorded data from one of the above experiments for the DJI Mavic Pro test drone. Barometer readings show the drone's altitude above the ground. Accelerations in both vertical and horizontal directions were also calculated from time series data. During vertical movements, the drone deviated slightly from a straight path due to errors in GPS modules. Similarly, during horizontal movements, the UAV was not moving at an exact constant altitude due to barometer errors. However, the average of these deviations was less than 0.1 m, which is considered negligible.

It was observed that power consumption steadily increases as the drone moves in an upward direction and decreases as it descends. GPS errors also generate minimal horizontal speed data during vertical motion, which have been filtered. It was observed that power consumption is relatively stable during horizontal motion at constant altitude. The hovering motion has been considered by recording power consumption between these horizontal and vertical motions.

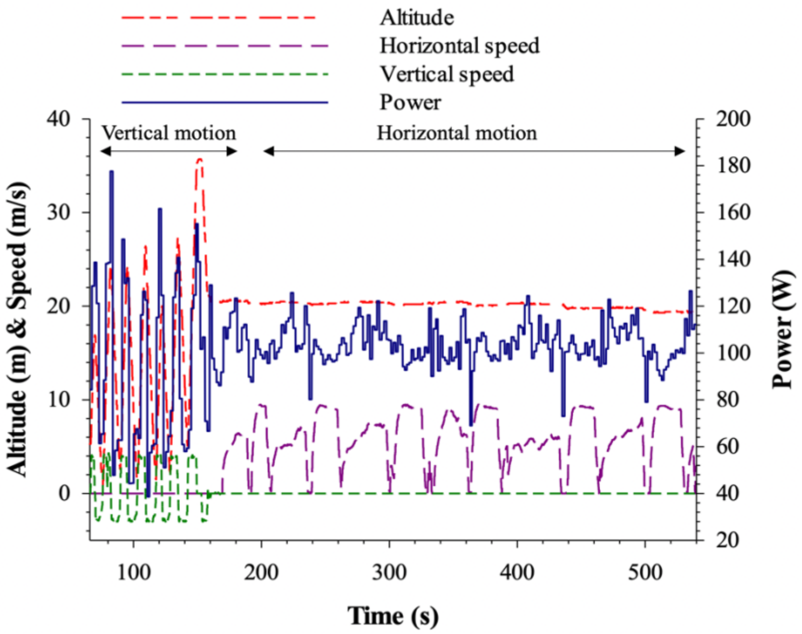

Figure 21 Battery power consumption of the DJI Mavic Pro during different motions.

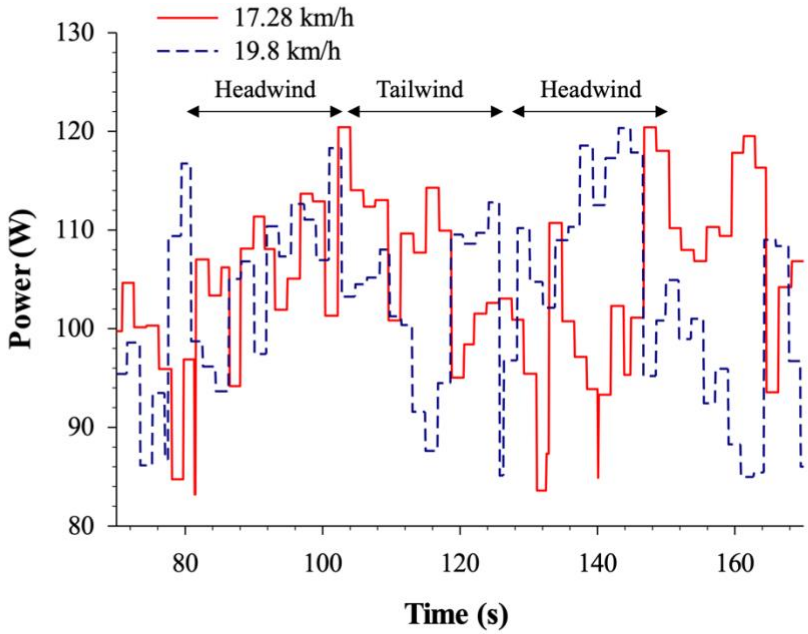

Figure 22 Battery power consumption of the DJI Mavic Pro under various wind conditions.

Powering drones is similar to power electric ground vehicles, but being aerial, they face some distinctive challenges. To elaborate, wind is a major environmental factor that affects power consumption of the Mavic Pro during experiments. Therefore, another set of experiments was designed to model and measure battery performance when the drone flies in the same direction as wind and in directions opposite wind. Wind speed and direction were recorded with a wind speed meter. The frequency of wind speed measurements was 2 sec. Flights were made at a local park, but on different days to consider different wind speeds and to make the study more comprehensive. The drone was made to fly closer to the ground to minimize errors in wind measurements due to elevation differences between the wind speed meter and the drone. The average wind speed of each flight has been used as a representative speed for the entire flight. Experiments were conducted for three wind speed cases: 17.28 km/h, 18 km/h, and 19.8 km/h.

It can be observed in Figure 22 that the DJI Mavic Pro's power consumption increases when it is flying in the direction opposite to the wind (*i.e.*, with a headwind) and decreases when it is flying in the same direction as the wind (*i.e.*, with a tailwind); however, the relationship is not linear. Aerodynamics confirm that flying with a headwind decreases power consumption due to an increase in relative flow over propellers and hence an increase in translational lift (FAA, 2016). On the other hand, at higher wind speeds, aerodynamic drag can outweigh translational lift (Tseng et al., 2017). During the experiments described above, when the drone was flying with a headwind at its maximum speed, more drag is created than translational lift resulting in more power consumption.

3.3.2 Regression Model of Power Consumption for the DJI Mavic Pro

Assuming a constant wind speed at all locations of the experiment, a multivariate linear regression model (Equation (14)) was derived using altitude values, horizontal and vertical speeds, horizontal and vertical accelerations collected from the empirical studies conducted in the previous section. The coefficients of the model were estimated by standard regression method. Estimated battery power consumption P, in Watts, is given by:

$$\begin{aligned} P = 103.67 &+ \begin{bmatrix} 0.9 \\ 0.048 \\ 0.204 \\ 0.128 \end{bmatrix}^T \begin{bmatrix} v_{xy} \\ v_{xy}^2 \\ v_{xy}.a_{xy} \\ v_{xy}.wind \end{bmatrix} + \begin{bmatrix} -0.764 \\ 0.006 \\ -0.505 \\ 0.034 \end{bmatrix}^T \begin{bmatrix} a_{xy} \\ a_{xy}^2 \\ a_{xy}.a_z \\ a_{xy}.wind \end{bmatrix} \\ &+ \begin{bmatrix} -2.54 \\ -2.359 \\ 1.167 \\ 1.987 \end{bmatrix}^T \begin{bmatrix} v_z \\ v_z^2 \\ v_z.a_z \\ v_z.wind \end{bmatrix} + \begin{bmatrix} -2.493 \\ -0.016 \\ -0.075 \\ -0.08 \end{bmatrix}^T \begin{bmatrix} a_z \\ a_z^2 \\ wind \\ wind^2 \end{bmatrix} \end{aligned} \tag{14}$$

where v_{xy} and a_{xy} are magnitudes of speed and acceleration vectors in the horizontal direction, respectively; andv_z and a_z are magnitudes of speed and acceleration vectors in the vertical direction, respectively. The wind vector in the horizontal direction is denoted by $wind$. If wind direction and speed are considered constant, total energy consumed within a flight with duration T can be estimated by $P \times T$.

3.3.3 Model Validation

The model presented in Equation (14) was validated by conducting a new set of experiments in which the same Mavic Pro was programmed to fly in both vertical and horizontal directions under different wind conditions. Wind speed during this flight was 5.76 km/h. It was observed that the given model was able to capture power consumption trends with respect to wind speed and direction of movement, as shown in Figure 23a. The average error of estimation for power consumption is 0.7% with a standard deviation of 0.11. Figure 23b depicts total energy consumption for the flight, as the ultimate goal is to optimize the entire flight of the drone. It was observed that the error in estimating total energy consumption at the end of the flight is 0.6%. These low levels of error in estimating power and energy consumption show good accuracy of the power consumption model for the drone allowing the model to be used to determine which direction would consume relatively more battery power and not to predict actual power consumption values for the given UAV while flying. This approach can also be repeated for any other commercially available drone.

3.3.4 Path Optimization

The given UAV flight planning and optimization problem is such that the UAV has to visit each waypoint to capture a picture exactly once and return to the starting point with the minimum trip cost (*i.e.*, lowest power consumption). As described earlier, this is a classic traveling salesman problem (TSP) and the literature contains numerous genetic algorithms solutions.

Genetic algorithms (GAs) are based on Darwin's theory of evolution, which states that the survival of an organism is defined by the "survival of the fittest" rule (Goldberg, 1989). The energy consumption model derived in the previous section has been used as a fitness function in the given optimization problem. Figure 24 presents the flow of the proposed algorithm whereas its main components are discussed in the next sections. The objective of the algorithm is to determine a UAV flight path with the least energy consumption, which also fulfills constraints of the TSP.

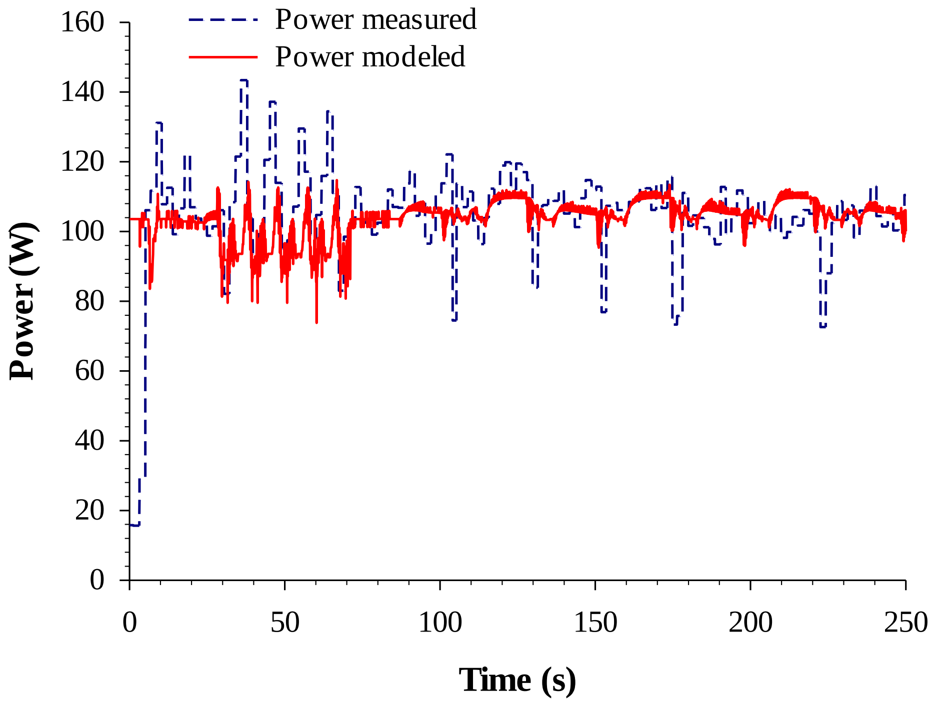

(a)

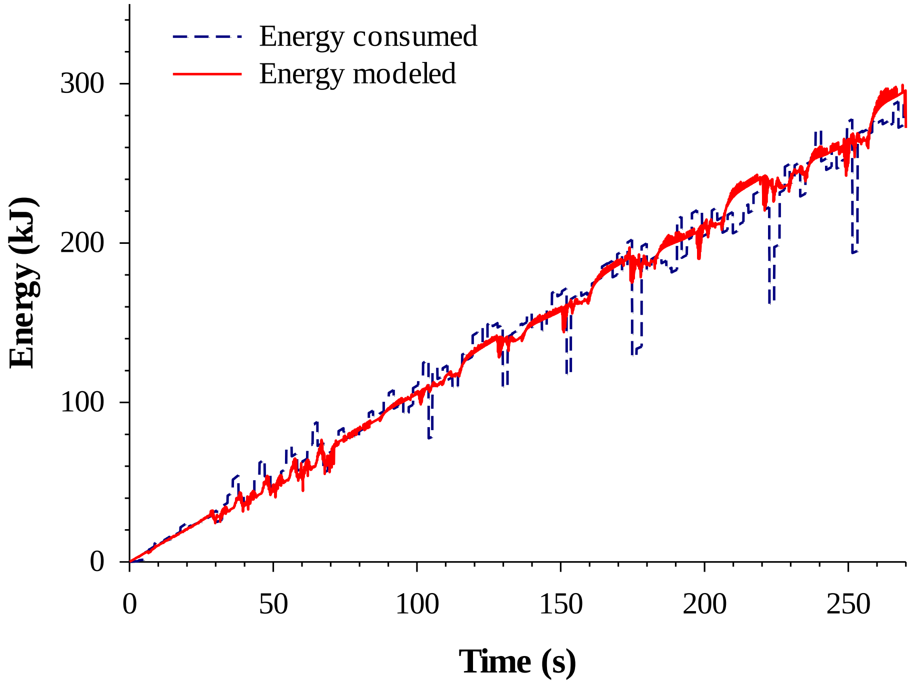

(**b**)

*Figure 23 Measured and modelled (**a**) power and (**b**) energy consumption for the DJI Mavic UAV.*

3.3.4.1 Fitness Function

The flight mission consists of a series of waypoints, and the UAV has been outfitted with a camera at the bottom to take pictures at each point in the flight. If *i*-1, *i*, and *i*+1 are three consecutive points in a proposed flight path, then the fitness of that path can be determined by Equation (15).

$$\text{Fitness Function} = \sum_{i=2}^{n-1} E_{i,i+1} + \alpha\theta_{i-1,i,i+1} \tag{15}$$

where $E_{i,i+1}$ is the energy consumed by the UAV while moving from waypoint *i* to waypoint *i*+1, and $\theta_{i-1,i,i+1}$ is the vector angle between path segments (*i*-1, *i*) and (*i*, *i*+1). Preliminary studies proposed that if the path has a significant number of sharp turns, then the drone consumes more time and consequently more energy in changing its direction.

Therefore, α has been included as the penalty for sharp turns between two path segments. Its value can be increased if sharp turns are not required. The fitness of a route is being interpreted in an inverse way such that routes with the least fitness values are better than those with higher values. The aim is to select individual routes that consume less power and have a smaller amount of sharp turns.

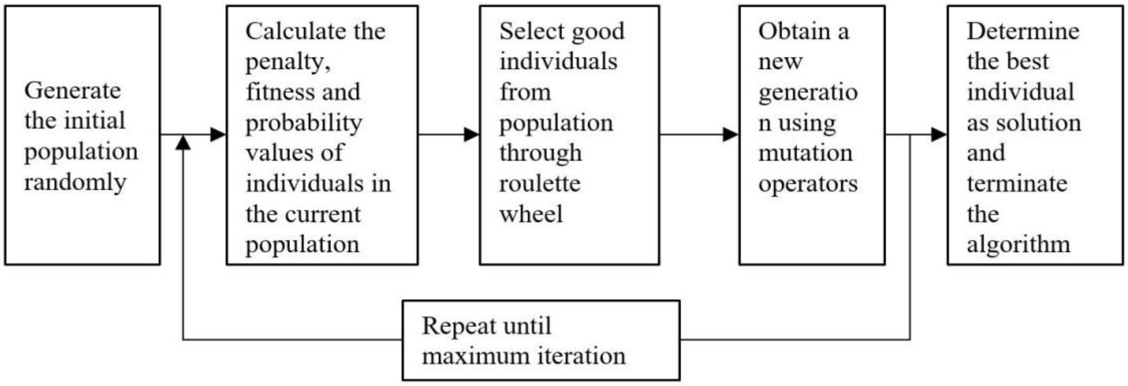

Figure 24 Proposed genetic algorithm (Meneses et al., 2017).

3.3.4.2 Chromosome Structure

Each chromosome has been defined by a series of waypoints in which each waypoint has a latitude, longitude, and elevation in the World Geodetic System (WGS 84). Such representation is called *Path Representation* and possibly the most natural representation of a tour (Larrañaga et al., 1999). This representation is also more suitable because it facilitates the use of many popular genetic operators like partially mapped crossover (PMX), cycle crossover, order crossover, and genetic edge recombination crossover (ER). Each chromosome should contain all points in it so that each point is visited by the UAV. Further, each waypoint should occur in a chromosome exactly once so that the UAV would visit each point only once. This chromosome structure has been implemented such that the drone, after visiting all waypoints, will return to its initial start point. Therefore, the first and the last genes in every chromosome should be entered the same depending on the location selected as a start point. If waypoint *i* is at the *j*-th position in the chromosome, then waypoint *i* is the *j*-th point to be visited.

3.4 Results

A case study was developed by deriving centerlines of benches for an open-pit mine in Nevada. Mine bench centerlines were manually extracted from the mine's point cloud using PhotoScan software. These centerlines were then elevated 36.75 m above the ground as the required image resolution is 1.27 cm. To ensure the minimum forward overlap of 80% between successive images along the bench, the maximum distance between two consecutive points was restricted to 7.6 m (using Equations (9-13)) . From these centerlines, two different regions (R1 and R2) were selected and optimized UAV flight paths for these regions were determined as shown in Figure 25b and Figure 26b using the designed GA in Matlab (MathWorks, 2020).

The maximum number of iterations was set at 10,000 and mutation operators implemented were swap, flip and slide. Using Equations (9-13), parallel paths for taking overlapping images with 80% forward and side overlap were determined for R1 and R2 as shown in Figure 25a and Figure 26a. The number of waypoints calculated in parallel and optimized missions for region R1 are 70 and 80, respectively; and for region R2 are 63 and 81, respectively.

Flight simulations for parallel and optimized paths were performed using the DJI assistant 2 software, which is the provided flight simulator for Mavic Pro (DJI, 2020b). Once both optimized and parallel missions have been designed, the UAV could be connected to the simulator. Initial and final battery readings were recorded from telemetry data once the drone has landed. The time of flight was determined as the difference between the time the mission started and time the drone landed back at the take-off point. The simulator is running on a Windows PC with 16 GB of RAM.

(**a**) (**b**)

Figure 25 Illustrations of ***(a)*** *parallel path for R1;* ***(b)*** *optimum path for R1.*

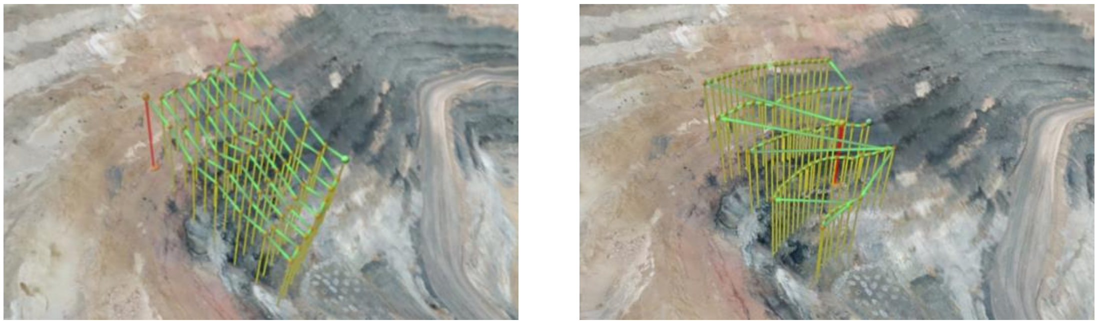

(**a**) (**b**)

*Figure 26 Illustrations of (****a****) parallel path for R2; (****b****) optimum path for R2.*

From Figure 27, it can be observed that battery percent and mission time for both regions are 50% less for the optimized path compared to the parallel path. Moreover, in the case of the optimized path, the UAV is programed to fly exactly over benches to image only the area of interest (horizontal bench surface in this case, with a final aim to monitor tension cracks in the next step of the research) saving both time and battery power. It can be seen that total battery power consumed in a particular UAV flight is directly proportional to flight time. This simulation study validates the proposed UAV flight path optimization algorithm by determining UAV paths for high-resolution imaging of an area that consume less battery power compared to a conventional parallel path.

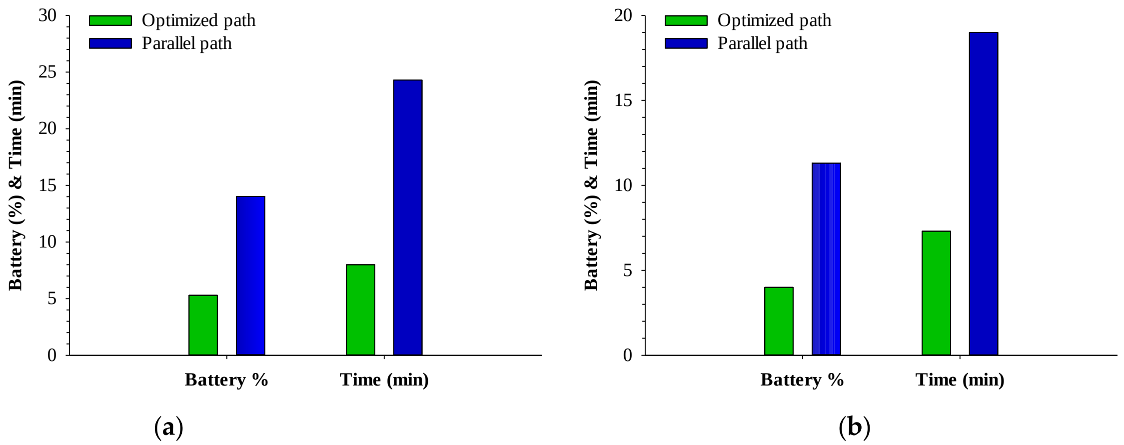

*Figure 27 Battery power consumed and flight time comparison for (**a**) region R1 and (**b**) region R2*

3.5 Discussion

In this study, a methodology has been presented to generate high-resolution 3D models of open-pit slopes using low cost DJI drones in an optimized manner. These drones are widely used in the Earth science industry (Al-Rawabdeh et al., 2016; Car et al., 2016; Lee and Choi, 2015; Suh and Choi, 2017). Methods presented in this paper have been validated using experimental and simulation studies. A comparison was performed between the resolution of 3D models generated using Stage 1 (constant elevation) and Stage 2 (proposed method) flights. The resolution of DEMs and orthomosaics generated from Stage 2 were double compared to Stage 1 3D models. Further, all autonomous UAV flights were performed safely without any accidents. With this validation study, it can be concluded that the proposed software can generate millimeter resolution 3D models of hazardous inaccessible open-pit slopes without any risks to personnel who are responsible for the surveys and measurements to obtain multiple parameters of mine slopes (For an extensive list of influencing factors, see, e.g., (Zare and Jimenez, 2015b; Zare Naghadehi et al., 2013)). Li and Ling (Li and Ling) have presented an approach for modifying a consumer like DJI by fitting it with an external computer equipped with camera and Wi-Fi link; however, in this approach, the flight of the drone could not be controlled by the external computer. The developed application is significantly beneficial from the point of view of its application in a real mining environment. It can not only plan and execute flights autonomously for any DJI drone but also collect high-resolution images of mine terrain with a low-resolution camera sensor. The generation of 3D model after the Stage 1 flight using photogrammetry is a time-consuming process which in case of large open-pit mines could take days to complete. However, this is a one-time step because the same 3D model could be used for several Stage 2 flights in future unless the terrain is changed significantly. It is also difficult to use the application in case of high winds weather conditions. It is advisable to conduct drone flights when the wind speed is around 2-4 m/s. Quadcopters have a finite battery time (Siebert and Teizer, 2014), which limits their operation in large open-pit mines for achieving centimeter-scale accuracy. The battery power consumption of the UAV has been studied and modeled using several experimental studies. For a test flight, model-predicted drone power consumption was compared with actual on-board battery power consumption. The average error of estimation was found to be 0.7%, which validates the drone power consumption model. The presented methodology can also be repeated for determining the power consumption model of any other consumer drone.

Further, a genetic algorithm (GA) has been used to compute optimized UAV flights for high-resolution imaging of open-pit slopes using the battery power consumption model. A simulation study was conducted to test battery power and time consumed by UAV flight paths computed by the GA for two different regions in a mine. Results showed that the proposed power consumption model and GA-computed UAV flights consumed 50% less time and battery power as compared to normal parallel flights for both regions. It can be seen in Figure 21, that the UAV consumes more energy when flying in a vertical direction than in a horizontal direction. Optimum paths for regions R1 and R2 (Figure 25b and Figure 26b) have significantly greater portions of horizontal segments as compare to vertical segments. Also, these paths reduce the number of turns the UAV takes in a flight mission. These two factors are the main reasons for lower flight time and battery power consumption in optimized paths. These results are similar to those presented in a recent paper (Shivgan and Dong) that used GAs to estimate energy efficient UAV flight paths. The optimized path with more horizontal segments and fewer turns is more suitable for open-pit mines where only the horizontal part of each bench is imaged sequentially. These paths can be computed for detecting and monitoring tension cracks on mine benches or for measuring the positional accuracy of drill holes on a production bench using a drone. The centerline of benches in an open-pit mine can be automatically extracted from the DEM as shown in (Winkelmaier et al., 2020). Wind speed during simulation studies was 0 m/s and hence not considered, although speed and direction of wind are parameters in Equation (14). The optimal flight plan would certainly change depending on wind conditions (Tseng et al., 2017). These study results show that high-resolution imaging using UAVs in open-pit mines can be optimized using battery power consumption modeling and the proposed genetic algorithm.

3.6 Conclusions

A high-resolution imaging setup is studied based on low-trim UAVs with the final aim to monitor stability conditions of open-pit highwalls. A ground station mobile application was designed using Android Studio, Google Maps API, and DJI Android SDK for generating high-resolution terrain maps of open-pit mines. The application is able to plan and execute area mapping operations for remote surveying of any area with UAVs. The application can also import 3D terrain models generated from photogrammetric software. A terrain-awareness feature has been incorporated into the application to maneuver the UAV over a non-planar terrain. This feature enables the drone to fly at altitudes as low as 10 m to capture millimetre-level resolution images of an area. It is able to accomplish this task with two flight stages. Stage 1 flight is a traditional high-altitude mapping operation, which outputs 3D models of the area. Stage 2 flight is planned using these models to adjust the drone’s flying altitude based on ground elevation. The entire method has been tested and validated at a local test site in a case study that generated 3D models with 6.3 mm/px resolution.

An empirical study was performed to model battery performance of the test UAV considering various flight circumstances. A linear regression model for the power consumption of the drone was derived and validated for a test scenario. Further, an optimization algorithm was proposed to solve the problem of path planning, which resulted in a path that consumes less battery power. A case study based on an open-pit mine in Nevada was presented. The algorithm was tested by performing simulation studies to determine the optimum path for high-resolution imaging of benches at the host mine. It is safe to conclude that the proposed algorithm can generate tours that consume approximately 50% less battery power and time for a given area.

CHAPTER 4 : AUTOMATIC EXTRACTION OF DISCONTINUITY CHARACTERISTICS

4.1 Introduction

The accurate characterization of geological discontinuities is an essential requirement in any slope stability analysis. Rock blocks detach and fail along weak planes defined by intersecting discontinuities (Jaboyedoff *et al.*, 2009; Kainthola *et al.*, 2015). All the major empirical rockfall risk analysis approaches need the joint set orientations and other characteristics as input (Ferrari *et al.*, 2016). Conclusive data on rock joints additionally assist with anticipating groundwater flow and rockfall, better blasting results in open-pit mines, and lastly superior conditions of slopes (Peik et al., 2020b; Zare and Jimenez, 2015a). Conventionally, discontinuities in a rock slope are measured manually in the field using scanline mapping with a compass. In some mines, 3D models of the rock mass surface are collected using a vehicle-mounted laser scanner and specialized software are used to make digital measurements of discontinuity characteristics. There are many limitations in traditional practices. In addition to being laborious, often safe access to the slope is not possible for carrying out in-person mapping or using a scanner. Especially, the in-person mapping method at the base of steep slope exposes the geologist to extreme rockfall hazards. Further, measurement of joint orientation and geometry at a few sample locations where a scanline crosses the structure doesn’t accurately account for the huge variation in the measurements across different parts of the mine. Finally, the development of mine requires more rigorous measurements as new slope faces are blasted every day.

There are ten parameters suggested by the International Society of Rock Mechanics (ISRM) for quantitative description of discontinuities in rock mass such as orientation, spacing, persistence, roughness, wall strength, aperture, filling, seepage, number of sets, and blocks size. The automated methods for the characterization of discontinuities from point clouds of rock mass are efficient compared to traditional methods (Slob et al., 2005).

In this paper, a novel method has been presented for the automatic extraction of joint sets from a 3D point cloud model for rock mass surfaces. This method leverages the advantage of a state-of-the-art deep neural network for automatic joint surface detection from high-resolution point clouds obtained from aerial photogrammetry. The orientation and joint sets are then determined using statistical analyses of the detected joint surfaces. The results confirm the benefits of this approach in terms of accuracy and time complexity.

After a review of the literature on this field in the next section, the proposed method has been described. This is followed by a case study to evaluate the overall methodology where the results from the proposed method are compared with previous approaches.

4.2 Related Work

In the last two decades, there has been an increased interest in developing automated and semi-automated methods for extracting discontinuity data from 3D surface models of rock masses. Many researchers used mathematical-statistical analyses and clustering algorithms for the segmentation of joint surfaces from 3D point clouds or meshes. Geometrical properties of points such as Euclidean distances or square of the sine of the angle between point normals are used as criteria for clustering the points belonging to joints. Major clustering-based methods used for joint sets extraction are multileader clustering (Olariu et al., 2008b), K-means clustering (Chen *et al.*, 2016), Fuzzy K-means clustering (Van Knapen and Slob, 2006), spectral clustering (Jimenez-Rodriguez and Sitar, 2006), Firefly algorithm with fuzzy K-means algorithm (Guo et al., 2017), Kernel density estimation with DBSCAN (Riquelme et al., 2014), Iterative Self-organizing Data Analysis Techniques Algorithm (ISODATA) (Zhang et al., 2018), and fast search and find density peaks (CFSFDP) algorithm. The application of some clustering algorithms requires prior knowledge of the number of clusters i.e., K. This might introduce human bias in the joint set analysis process. However, the optimum value of K can be determined using minimum description length (MDL) (Barron *et al.*, 1998) statistic or Silhouette validity index (Rousseeuw, 1987). Clustering-based algorithms struggle to find optimal results in presence of noise in the 3D model such as vegetation, sky or rock debris. Further, the computation time for these methods is usually higher and increases significantly for more than one million points.

Recently, joint surfaces have been automatically extracted using region growing-based methods in which random seed points are selected in the 3D point cloud and then expanded based on preset rules. The point normal and curvature values are used to find and grow the initial seed points (Wang et al., 2017). Ge *et al.* (2018) proposed an efficient growth criterion to determine seed points and gridded evenly spaced point cloud to improve computation time. Drews *et al.* (2018) suggested additional growth criteria for increasing accuracy such as distance between candidate points and the growing region as well as the standard deviation of candidate points. Hu *et al.* (2019) divided a rock mass point cloud into voxels and determined coplanar points in them. The voxels with detected planar points are merged using region growing. Higher accuracy and lower computation time are found to be the strengths of these methods. However, these methods require the optimal values for up to eight to ten parameters. There is not an objective way yet to find the values for these parameters. Usually, it is accomplished using a trial-and-error approach by using a subset.

Other approaches based on iterative plane fitting using RANSAC, PCA (Ferrero et al., 2009b; Gomes et al., 2016) or extracting least-square fitting planes (Gigli and Casagli, 2011) by a moving cube have also been proposed for extracting joints from 3D point cloud model of the rock mass. Some of the limitations of these methods are relatively lower accuracy, higher computation time, and difficulty in determining the optimum size of the moving cube. Fusion methods where the data from 2D images is combined with digital elevation maps for detection of discontinuity traces and measurement of their orientations (Vasuki et al., 2014).

Recent developments in the field of artificial intelligence such as machine learning and 3D deep learning show the possibility of application of these methods for discontinuity characterization. Qi *et al.* (2017) proposed a deep learning network “PointNet” which can be employed for the classification of the 3D point cloud as well as prediction of point normal. Soilán *et al.* (2019) used the PointNet for automatic classification of an aerial point cloud collected using laser scanner into vegetation, roads, and other structures with 87% of accuracy. Weidner *et al.* (2019) proposed a Random Forest machine learning approach for automatic classification of TLS data into vegetation, talus, bedrock, or other categories. A critical analysis of all the major approaches presented in the literature for automatic or semi-automatic extraction of joint characteristics from 3D surface models of the rock mass is presented in Battulwar *et al.* (2021).

4.3 Proposed Method

In this paper, a novel method has been proposed for the automatic extraction of average dip angles and dip directions of the joint sets from a 3D point cloud model of the rock mass. This method comprises five steps which are depicted in Figure 28 and are built upon the approach proposed by Battulwar *et al.* (2020). These steps are thoroughly explained in the following sub-sections.

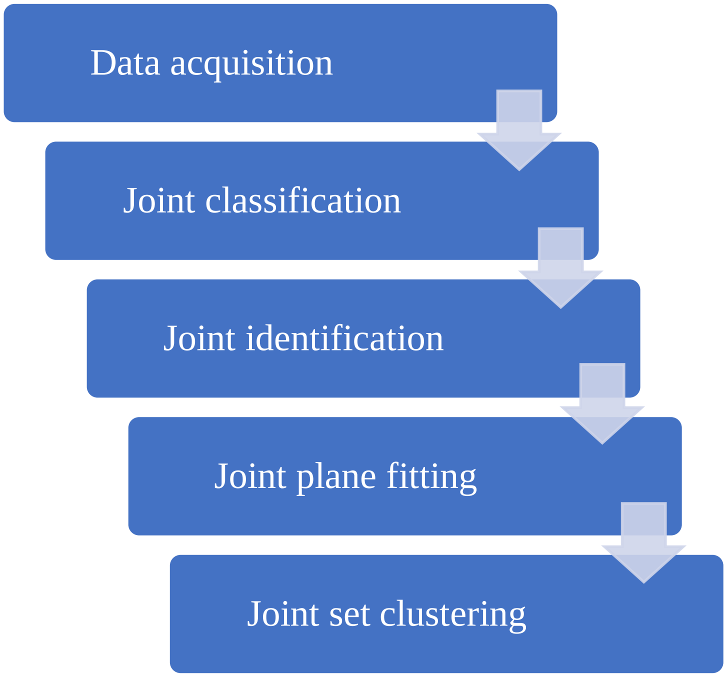

Figure 28. Flow chart of the proposed methodology

4.3.1 Data acquisition

The first step in this methodology consists of collecting images and generating high-resolution 3D point clouds of rock mass using photogrammetry (Battulwar *et al.*, 2020). For this study, the images of the road cut from three different sites have been collected from the Donner Pass Road, California, USA. High-quality overlapping images of the rock face were collected using DJI Phantom 4 Pro drone (DJI, 2020a). The drone was equipped with a 20 MP imaging sensor and has a flight time of 20-25 minutes. Once the images were collected, they were processed in the office to generate 3D point cloud models using Agisoft Metashape software (Agisoft, 2020). The properties of the three datasets created by the above procedure are shown in Table 6 as well as their 3D representations are depicted in Figure 29. Each dataset represents the exposed surface of the rock mass using more than a million 3D points where each point has a geographical coordinate and RGB value. Apart from the discontinuities, the datasets also consist of vegetation, rock debris, and parts of the road. It is important to note that Dataset A and B are used in Section 3.2 whereas Dataset C has been used to evaluate the entire methodology.

Table 6. Properties of Dataset A, B, and C

Dataset	**A**	**B**	**C**
No. of points	12M	2.4M	1.6M
Average point density	0.682 pts/cm2	0.615 pts/cm2	0.34 pts/cm2
No. of images	107	102	40
Location	Donner Pass Road, USA		
Rock type	Granite		
Physical setting	Road cut		

(a)

(b)

(c)

Figure 29. Rock Mass 3D Point Clouds: (a) Dataset A, (b) Dataset B, and (c) Dataset C

4.3.2 Joint classification

4.3.2.1 PointNet

PointNet (Qi et al., 2017) is a deep neural net proposed for 3D point cloud classification, part segmentation, and semantic segmentation. Figure 30 shows the architecture of this deep net that directly takes the raw point cloud as input and outputs the class labels for the entire point cloud or each point. This network learns all the parameters required for the classification of points during supervised training. Since this is a semantic classification task, a segmentation network is used for the prediction of labels per point. The size of the input point cloud is fixed at 2048 points.

In this method, PointNet is employed to detect joint points from the entire rock mass point cloud. Hence, this step helps the entire process in terms of accuracy and computation time. Specifically, PointNet directly eliminates the points belonging to the non-joint surfaces as well as the noise points belonging to vegetation, sky, debris, and road. This elimination decreases the total number of points of interest in the successive steps significantly thus improving the run time of the algorithm.

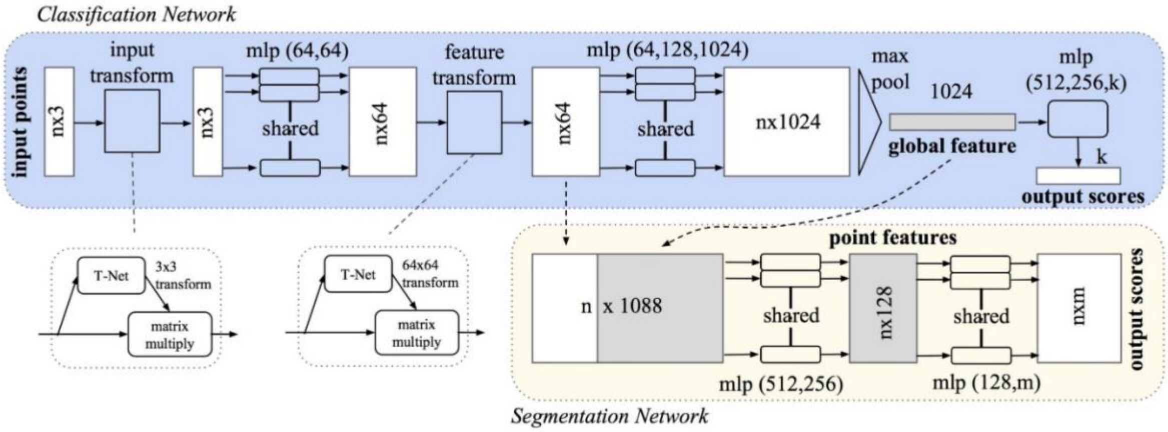

Figure 30. The architecture of PointNet (Qi et al., 2017)

4.3.2.2 Dataset Preparation

PointNet needs to be trained using labeled datasets for it to recognize points belonging to the joint surfaces. Datasets A and B were used for generating training and validation data required by PointNet. The “Segment” tool in CloudCompare (CloudCompare, 2020) software was used to manually label the rock mass point clouds. In each dataset, the points which represent the joint surfaces are labeled as a joint class and the rest of the points are labeled as the non-joint class as shown in Figure 31. Since the input size of each sample to PointNet is 2048, these datasets were separately divided into voxels such that each voxel will have at least 2048 points. This resulted in a total of 5765 voxels. From this collection, 1000 voxels were selected such each voxel will have points from both the classes. All the selected voxels were partitioned into two parts: training and validation sets. The training set contained 800 voxels whereas the validation set contained 200 voxels.

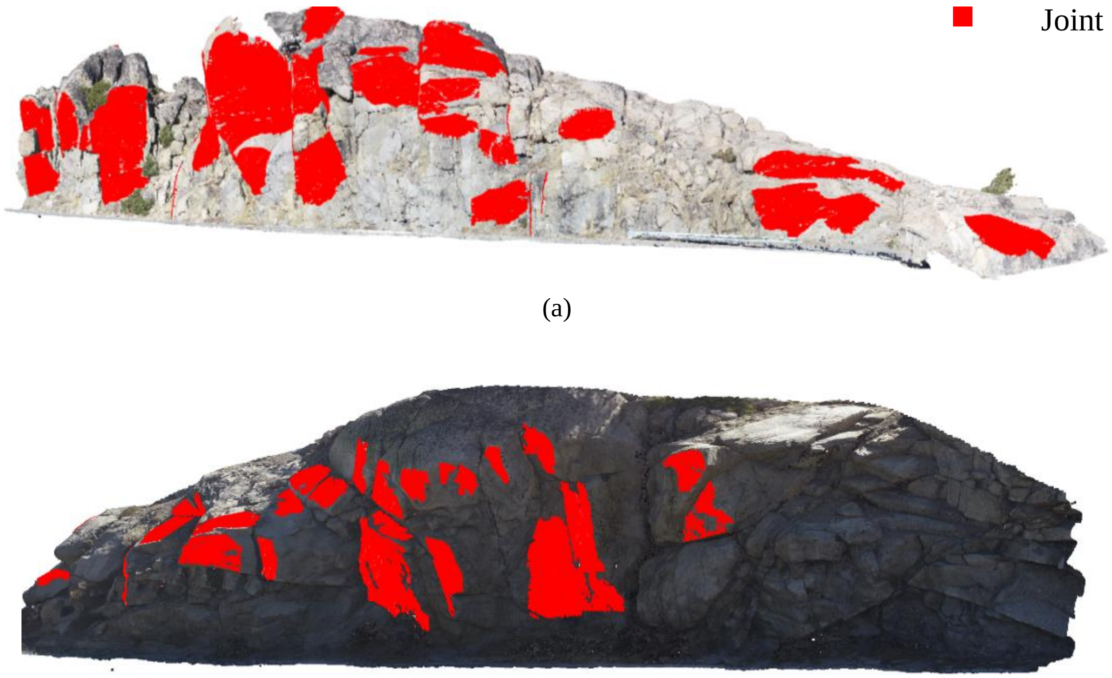

(a)

(b)

Figure 31. Labelled point clouds: (a) Dataset A, and (b) Dataset B

4.3.2.3 Experimental Work

The PointNet model was implemented using the Keras library with the TensorFlow backend. During training, each sample consists of a voxel from which 2048 points were randomly sampled for input to PointNet. These points were represented by x, y, and z coordinate and normalized to a unit sphere. The training data was further augmented by rotating the input voxel points by a random angle between 0° to 60° clockwise or anti-clockwise about all three axes. The experiments were performed using Nvidia GTX 2080 Ti graphics cards. The experimental results were evaluated using accuracy, which the ratio of correctly classified points to the total number of points. The parameters for the training stage are shown in Table 7. During the experiments, the training accuracy of 84% was achieved whereas the classification accuracy on the validation set was 77%. This was the highest validation accuracy achieved during the experimental analysis without overfitting. This trained PointNet model was used for the automatic classification of joint points.

Table 7. Training parameters

Training parameters	
No. of input points	2048
Batch size	12
Epoch	80
Learning rate	0.001
Momentum	0.9
Decay step	337620
Decay rate	0.5
Dropout	0.8
Optimizer type	Adam

4.3.3 Joint identification

After the classification of joint points using PointNet, the next step is to cluster them into individual joint surfaces. In this method, DBSCAN (Ester et al., 1996) has been used for this purpose. There are two parameters needed by DBSCAN: (a) eps, the density parameter used to determine neighboring points; (b) min-points, the minimum number of points to designate a cluster. The change in density of the point cloud affects the performance of DBSCAN. The value of eps has been adopted from Riquelme *et al.* (2014). As a result of this step, the joint points will be segmented into clusters with each cluster representing a joint surface.

4.3.4 Joint plane fitting

After the identification of joint surfaces, their geological orientations can be computed by fitting planes to points belonging to those surfaces. This is achieved using the random sample consensus (RANSAC) algorithm (Fischler and Bolles, 1981). The RANSAC method outputs a plane equation for each joint surface in the form:

$$ax + by + cz + d = 0 \tag{15}$$

where a, b and c represent the unit normal vector of the plane. The dip direction and dip angle for the plane can then be computed by using Eqs. 16 and 17 (Kong *et al.*, 2020)

$$dip\ direction = p - \tan^{-1}\left(\frac{b}{a}\right) \tag{16}$$

where p = 90°, if a < 0; p = 270, if a >0; Dip direction = 0°, if a=0 and b ≥ 0; Dip direction = 180°, if a=0 and b ≤ 0.

$$dip = q - \tan^{-1}\left(\frac{|c|}{\sqrt{a^2 + b^2}}\right) \tag{17}$$

where q = 90°, if $a^2 + b^2 \neq 0$; Dip direction = 0°, if $a^2 + b^2 = 0$.

4.3.5 Joint set clustering

A joint set is the collection of joint planes which occur at similar orientations in the rock mass. Once the joint planes and their orientations have been extracted, they can be analyzed using advanced machine learning algorithms to find the mean joint set orientations. The proposed method employs a clustering algorithm to classify the joint planes into clusters that represent each joint set. The criterion for clustering is the square of the sine of the angle between joint plane normals. DBSCAN has been again employed in this step to find the joint sets and mean orientations. The values for eps and min-points were 0.021 and 5 respectively in this step.

4.4 Spacing

As discussed in Chapter 2, spacing is the normal distance between joint planes. It is measured along a scanline intersecting the discontinuity planes perpendicularly. Spacing is an essential characteristic of a joint set as it defines the block sizes in jointed rock mass. It is difficult to calculate spacing manually for large joint planes which are spread in across the rock mass.

In this section, a methodology has been presented for automatic calculation of non-persistence (NP) spacing. In this approach, spacing has been calculated between a given joint plane and its closest neighbour in a joint set such that their 3D relationship is considered. It method assumes that the 3D plane equations and surfaces of discontinuities in all joint sets are available. For calculation of NP spacing for each joint sets, the algorithm first sorts all the joints planes based on *d* parameter of their equations and stores them in a list *l*. Then, it calculates the centroids of all the joint planes. Then, it starts from the plane with the smallest *d* in list *l* and finds centroid nearest to it from all the planes with *d* greater than itself. The normal spacing between the joint plane and the plane corresponding to the nearest centroid is calculated and stored. This process is repeated for all the *d* parameters in *l*. The spacing is calculated using the formula where *a*, *b*, and *c* are the average orientation of the given joint set:

$$\frac{|d_1 - d_2|}{\sqrt{a^2 + b^2 + c^2}} \tag{18}$$

At the end of the process, spacings are calculated for each joint set. The normal spacing is then determined by taking the mean of all the spacings. Further statistical values such as standard deviation, minimum, maximum and mode are calculated. A density function of spacing distribution is also estimated.

4.5 Results and Discussion

A case study has been presented in this section for validating the application of the proposed technique using Dataset C. Initially, the PointNet is used to classify joint and non-joint points in this dataset. Figure 32 depicts the results of PointNet classification on the entire dataset. It can be seen that the major joints were correctly classified whereas the noise such as vegetation or debris was rejected. The classification accuracy, in this case, was 69.64%.

Application of DBSCAN resulted in the identification of 111 joint surfaces as shown in Figure 33. The values of eps and min-points were 0.5 and 100 respectively. Manual readings for the joint orientations measured using the Compass plugin (Samuel T. Thiele et al., 2017) in CloudCompare software were considered as ground truth. Finally, the dip and dip direction were computed for these joint surfaces using RANSAC and compared with the ground truth.

The comparative analysis revealed that 67 joint surfaces of the total detected surfaces were identified correctly as the rests were vegetation or rock debris. Further, the average error in the measurement of orientations for the correctly identified joint surfaces was -2.06° and -1.24° in the cases of dip direction and dip angle respectively. This shows that the methodology is accurate for joint plane orientation purposes.

Figure 32. Visual results of joint classification using PointNet.

The performance of the proposed method was further evaluated in terms of accuracy and computation time. Discontinuity Set Extractor (DSE) (A. Riquelme et al., 2016) was used to find the joint sets using the same dataset. The mean orientations of the joint sets from DSE as well as the proposed method were compared with ground truth. In this case, the ground truth has been generated by manually extracting joint sets using Dips (Dips, 2020) software as shown in Figure 34a. The results from this analysis are summarized in Table 8. A total of five joint sets were identified using Dips. It can be seen Figure 35 that the proposed method was able to identify all the joint sets. The average error for the proposed method was lower than DSE in case of dip indicating that the computed dip values for the joint sets are closer to ground truth. The average error is higher than DSE for dip direction due to excessive deviation in case of joint set #1. Therefore, it can be concluded that the proposed method is able to measure mean joint dip orientations from 3D point cloud model of rock mass with relatively higher accuracy. The higher average error observed for dip directions needs to be further investigated.

Figure 33. Results of DBSCAN clustering on the segmented point cloud.

This research work proposed the foremost methodology for the application of 3D deep learning for the automatic characterization of joint sets. It has been observed earlier that the classification accuracy for joint points for Dataset C was lower compared to the

PointNet accuracy during the training and validation stage. The lower accuracy is due to the difficulty in differentiating between joint surfaces and other parts of rock mass which also have planar surfaces. In particular, the bottom regions of the 3D model represent road which is planar and horizontal. This might be affecting the performance of the method.

The extraction of discontinuity characteristics using methods based on a statistical analysis of geometrical properties requires high computation time. One of the goals of this research was to reduce the computation times for joint set extraction. The proposed method based on PointNet supports parallel processing using GPUs in contrast to DSE which only runs on the CPU. The recorded processing time for more than one million points using the proposed method was only 55.27 seconds whereas it was 3231 seconds in the case of DSE. Moreover, this method doesn't need extensive statistical analysis thus removing human bias. Previously proposed methods based on region growing required determination of various parameters reducing their usefulness whereas the DBSCAN algorithm used in the proposed method requires only two parameters.

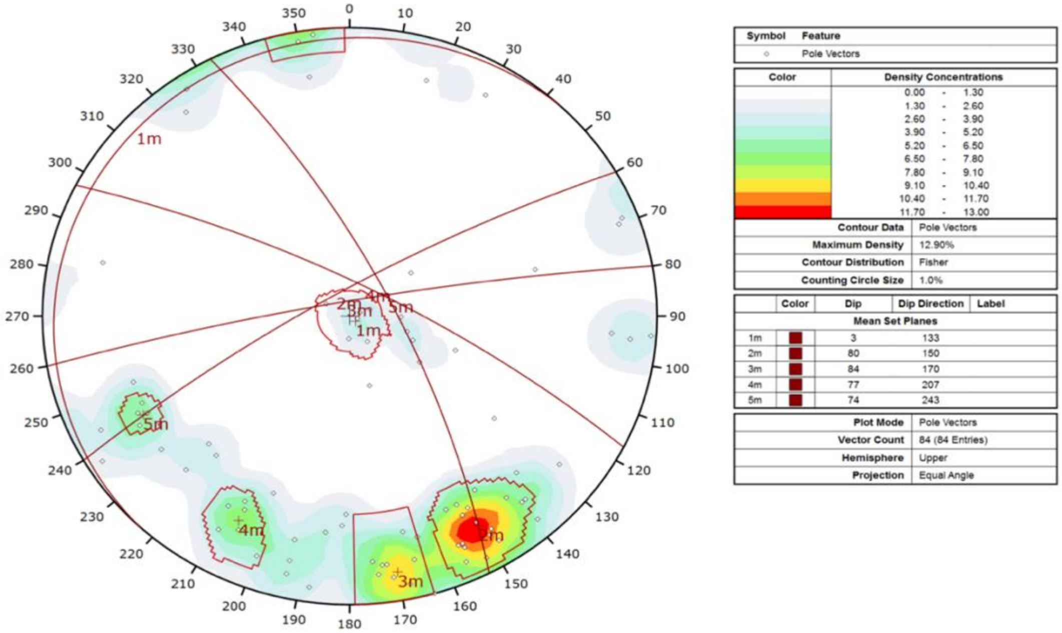

Symbol	Feature
○	Pole Vectors

Color	Density Concentrations
⬜	0.00 - 1.30
⬜	1.30 - 2.60
🟦	2.60 - 3.90
🟦	3.90 - 5.20
🟩	5.20 - 6.50
🟩	6.50 - 7.80
🟩	7.80 - 9.10
🟨	9.10 - 10.40
🟧	10.40 - 11.70
🟥	11.70 - 13.00
Contour Data	Pole Vectors
Maximum Density	12.90%
Contour Distribution	Fisher
Counting Circle Size	1.0%

	Color	Dip	Dip Direction	Label
Mean Set Planes				
1m	🟥	3	133	
2m	🟥	80	150	
3m	🟥	84	170	
4m	🟥	77	207	
5m	🟥	74	243	

Plot Mode	Pole Vectors
Vector Count	84 (84 Entries)
Hemisphere	Upper
Projection	Equal Angle

(a)

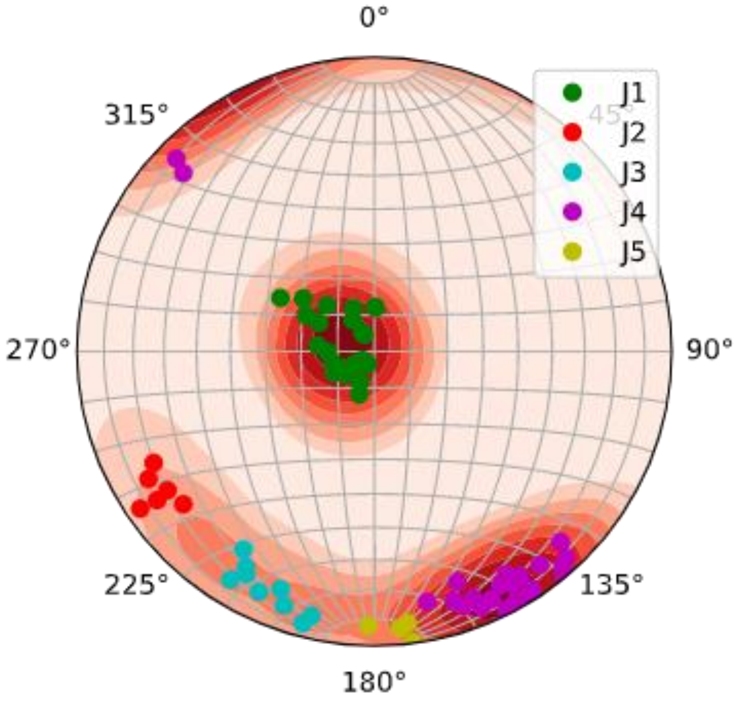

(b)

Figure 34 Comparison of joint sets orientations between (a) Dips software; (b) proposed method

Table 8. Comparison of mean joint set orientations using different methods. D – Dip (º), DD - Dip direction (º)

	Dips		**DSE**		**Proposed method**		**DSE**		**Proposed method**	
Set	D	DD	D	DD	D	DD	Δ|D|	Δ|DD|	Δ|D|	Δ|DD|
1	3	133	3.85	45.04	8.4	277.42	0.85	87.96	5.4	144.42
2	80	150	80.18	151.26	83.2	152.71	0.18	1.26	3.2	2.71
3	84	170	76.54	185.2	83.94	174.4	7.46	15.2	0.06	4.4
4	74	243	66.35	236.89	74.8	237.02	7.65	6.11	0.8	5.98
5	77	207	65.51	218.99	75.4	204.7	11.49	11.99	1.6	2.3
Average error							5.526	24.504	2.212	31.962

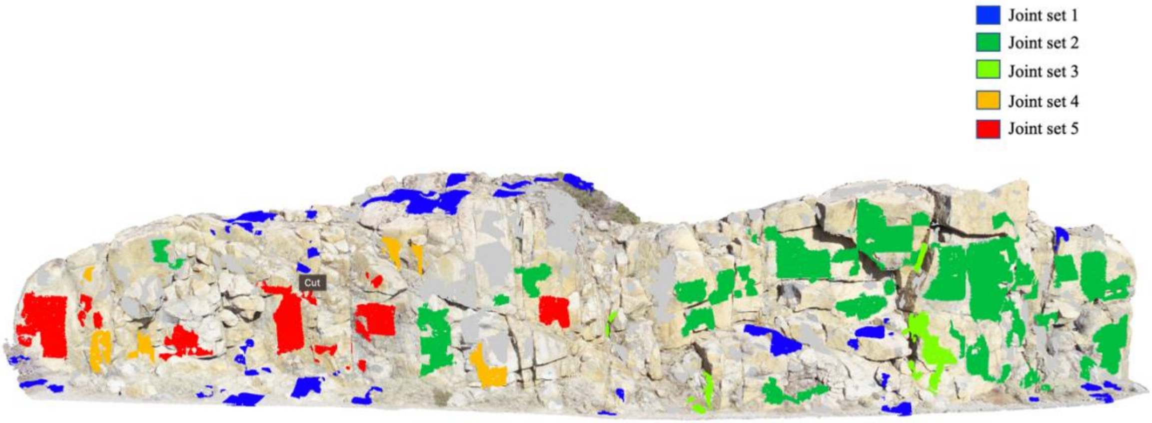

Figure 35 Extracted joint sets

In order to validate the spacing method a case study has been considered from (Riquelme et al., 2015). A limestone rock slope shown has been selected which is shown in Figure 36 . This rock represents several challenges such as smoothed surfaces due to weathering and non-persistence discontinuity. A 3 x 2 m area of this rock mass has been selected and its 3D point cloud has been derived using a Leica C10 laser scanner. This point cloud has 301089 points.

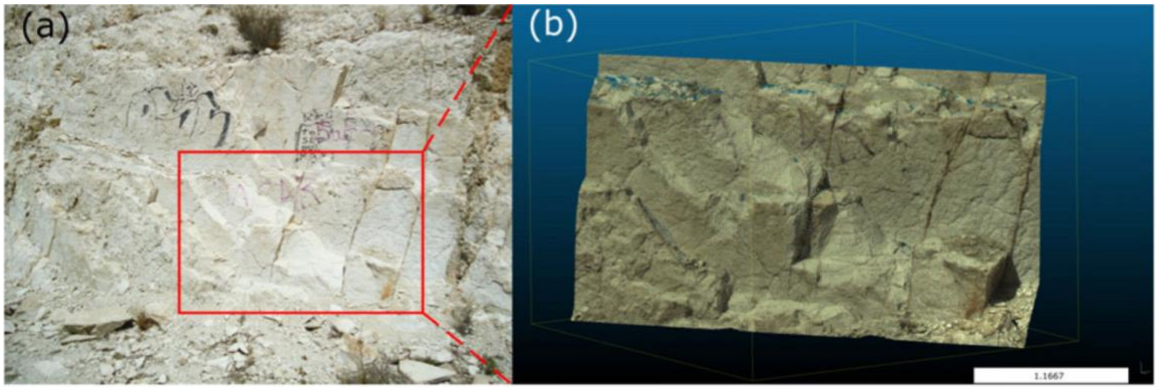

Figure 36 Spacing case study data set (Riquelme et al., 2015)

The analysis of the rock mass 3D point cloud using DSE software has shown that there are four discontinuity sets. Joint plane equations and point cloud are taken from this case study as input for the presented methodology.

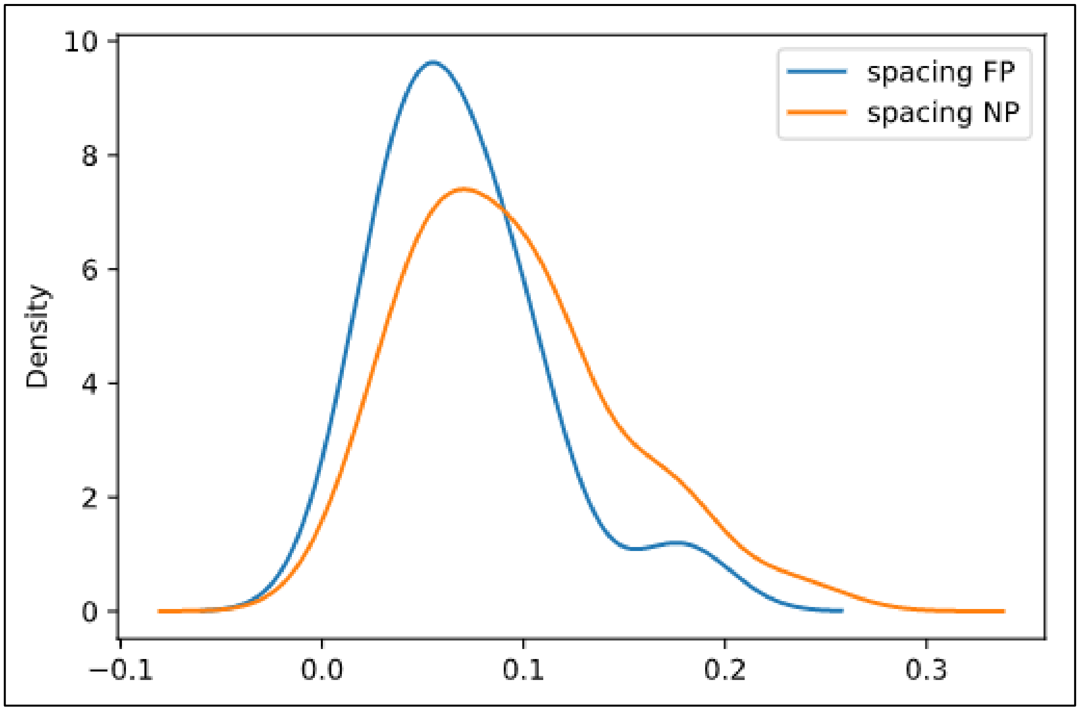
10
8
6
4
2
0
Density
−0.1
0.0
0.1
0.2
0.3
spacing FP
spacing NP

(a)

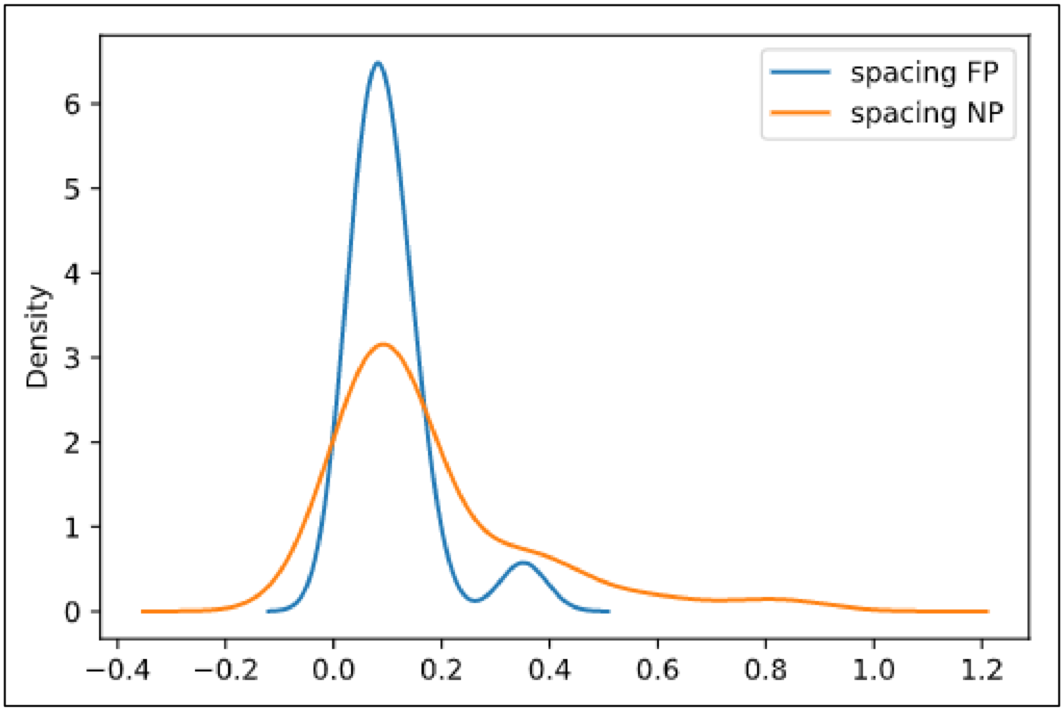
6
5
4
3
2
1
0
Density
−0.4
−0.2
0.0
0.2
0.4
0.6
0.8
1.0
1.2
spacing FP
spacing NP

(b)

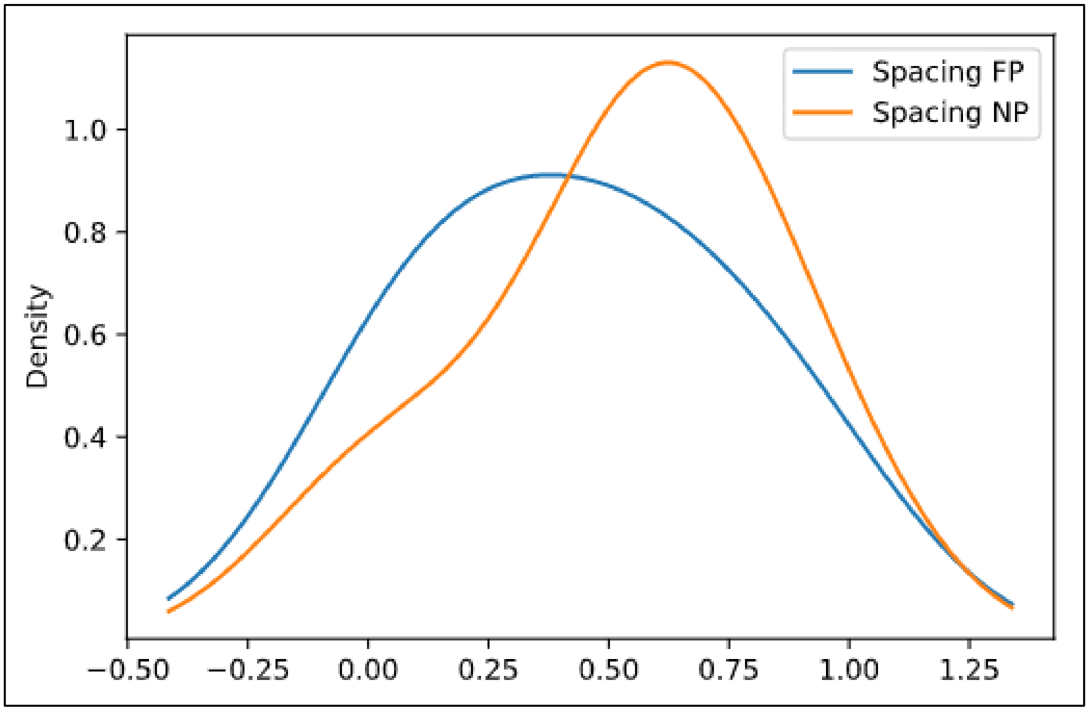

(c)

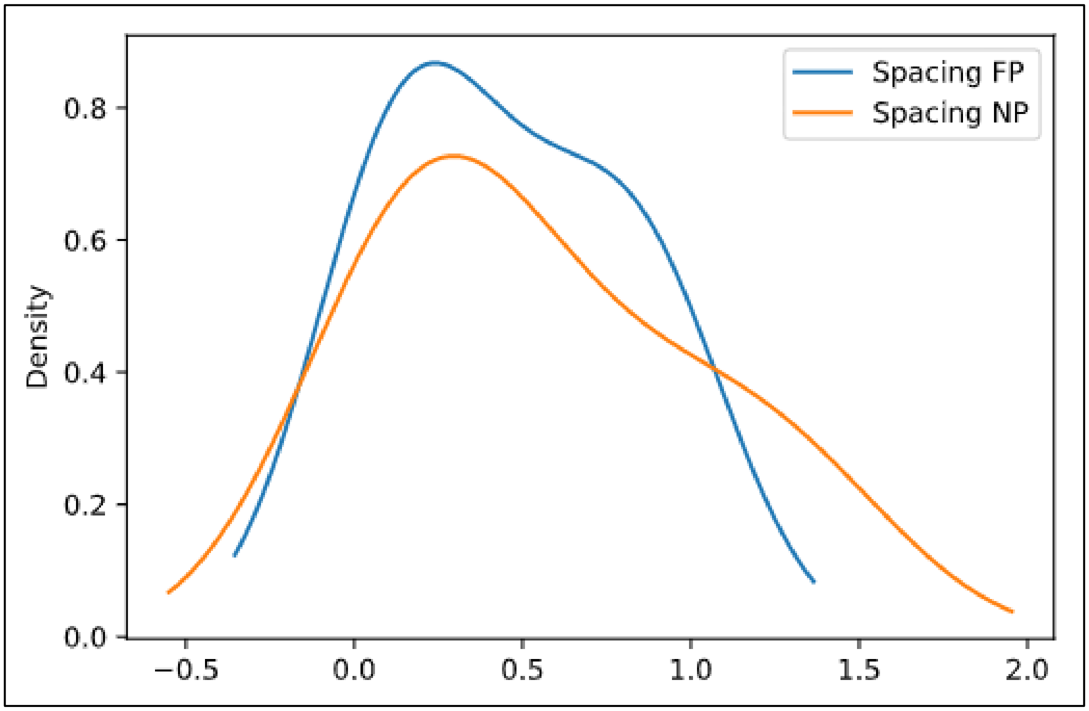

(d)

Figure 37 Density function of spacing values for (a) Joint set 1;(b) Joint set 2; (c) Joint set 3; (d) Joint set 4

Table 9 Spacing calculated using the proposed method

	Jt #1 (FP)	Jt #1 (NP)	Jt #2 (FP)	Jt #2 (NP)	Jt #3 (FP)	Jt #3 (NP)	Jt #4 (FP)	Jt #4 (NP)
Minimum (m)	0.020	0.024	0.037	0.037	0.024	0.024	0.075	0.075
Maximum (m)	0.178	0.233	0.351	0.818	0.900	0.900	0.935	1.327
Mode (m)	0.020	0.109	0.037	0.111	0.024	0.024	0.075	0.075
Std. deviation (m)	0.042	0.052	0.075	0.180	0.344	0.323	0.361	0.488
Mean (m)	0.069	0.094	0.103	0.175	0.437	0.529	0.453	0.554
Field value (m)	0.172		0.224		0.397		0.503	
Error (m)	0.103	**0.078**	0.121	**0.049**	**0.040**	0.132	**0.050**	0.051

The density functions for full-persistent (FP) and non-persistent (NP) spacing for each joint set was estimated using kernel density estimation functions available in the Seaborn plotting library in Python as shown in Figure 37. Statistical values for the spacing distributions are shown in Table 9. The mean spacing values are compared against the field values which were based on evident discontinuity planes exposed on the surfaces. The field values are also corrected (Terzaghi, 1965) based on the slope of rock and discontinuity orientations.

It can be observed from Table 9 that the mean spacing value determined using the algorithm are close to the field values. The calculated values were also less than the field values. This could be due to sampling only large joints visible to eyes in the field where the algorithm onsiders smaller discontinuities as well. This method calculates the non-persistent spacing of joints which are higher than full persistence.

4.6 Conclusions

This study aims to propose a fast and automatic method for joint sets extraction from 3D point cloud models of rock mass surfaces. In this work, unmanned aerial vehicles and photogrammetry have been used for the generation of rock mass models. A deep neural network PointNet classifies joint points from the 3D models. Then, individual joint surfaces are segmented using DBSCAN and their dip and dip directions are calculated. Finally, the method outputs joint sets and their mean orientations. A case study is used to evaluate the performance of the entire methodology. The results show that the proposed method can characterize joint sets orientations with average errors of 2.2° and 31.9° in case of dip and dip direction respectively. The computation time of the proposed method was almost an hour faster than a previously published method. Finally, this research shows the significant potential of deep learning for discontinuity characterization from rock mass point clouds.

4.7 Future Work

The presented research has shown that the application of 3D deep learning networks for joint mapping in surface models of rock mass can enable efficient and safe geotechnical mapping in open pit mines. In future, more research will be done on the same methodology to extract other discontinuity characteristics such as persistence, block size and face irregularity. Further, data collection endeavors at mines need to be undertaken to increase the training date set for PointNet. Excessive deviation of dip direction in case joint sets also needs to be investigated. The ultimate objective of this research project is to create an automated rock fall risk assessment system (ARAS) for open pit mines. Therefore, in the final stages of the project, this methodology will be integrated into an empirical system which takes into account other rock mass characteristics and parameters to output a rock fall risk index for every location in the mine.

REFERENCES

3DF Zephyr - photogrammetry software - 3d models from photos [WWW Document], 2020. URL https://www.3dflow.net/3df-zephyr-photogrammetry-software/ (accessed 11.27.20).

Abe, J., Marzolff, I., Ries, J., 2010. Small-Format Aerial Photography, Small-Format Aerial Photography. Elsevier Inc. https://doi.org/10.1016/C2009-0-18493-3

Abellán, A., Oppikofer, T., Jaboyedoff, M., Rosser, N.J., Lim, M., Lato, M.J., 2014. Terrestrial laser scanning of rock slope instabilities. Earth Surf. Process. Landforms 39, 80–97. https://doi.org/10.1002/esp.3493

Abellán, A., Vilaplana, J.M., Calvet, J., García-Sellés, D., Asensio, E., 2011. Natural Hazards and Earth System Sciences Rockfall monitoring by Terrestrial Laser Scanning-case study of the basaltic rock face at Castellfollit de la Roca (Catalonia, Spain). Hazards Earth Syst. Sci 11, 829–841. https://doi.org/10.5194/nhess-11-829-2011

Abellán, A., Vilaplana, J.M., Martínez, J., 2006. Application of a long-range Terrestrial Laser Scanner to a detailed rockfall study at Vall de Núria (Eastern Pyrenees, Spain). Eng. Geol. 88, 136–148. https://doi.org/10.1016/j.enggeo.2006.09.012

Agisoft, 2020. Agisoft Metashape. [WWW Document]. URL https://www.agisoft.com/ (accessed 4.23.20).

Airware, 2018. Blog Barrick Nevada’s Surveying Team Integrates Airware into Daily Goldstrike Operations [WWW Document]. URL https://www.owler.com/reports/airware/airware-blog-barrick-nevada-s-surveying-team-integ/1532558691413 (accessed 4.23.20).

Al-Rawabdeh, A., He, F., Moussa, A., El-Sheimy, N., Habib, A., 2016. Using an Unmanned Aerial Vehicle-Based Digital Imaging System to Derive a 3D Point Cloud for Landslide Scarp Recognition. Remote Sens. 8, 95. https://doi.org/10.3390/rs8020095

Alejano, L.R., Stockhausen, H.W., Alonso, E., Bastante, F.G., Ramírez Oyanguren, P., 2008. ROFRAQ: A statistics-based empirical method for assessing accident risk from rockfalls in quarries. Int. J. Rock Mech. Min. Sci. 45, 1252–1272. https://doi.org/10.1016/j.ijrmms.2008.01.003

AliceVision | Meshroom - 3D Reconstruction Software [WWW Document], 2020. URL https://alicevision.org/#meshroom (accessed 11.27.20).

Armesto, J., Ordóñez, C., Alejano, L., Arias, P., 2009. Terrestrial laser scanning used to determine the geometry of a granite boulder for stability analysis purposes. Geomorphology 106, 271–277. https://doi.org/10.1016/j.geomorph.2008.11.005

Assali, P., Grussenmeyer, P., Villemin, T., Pollet, N., Viguier, F., 2014. Surveying and modeling of rock discontinuities by terrestrial laser scanning and photogrammetry: Semi-automatic approaches for linear outcrop inspection. J. Struct. Geol. 66, 102–114. https://doi.org/10.1016/j.jsg.2014.05.014

Ball, G.H., Hall, D.J., 1965. ISODATA, a Novel Method of Data Analysis and Pattern Classification.

Barron, A., Rissanen, J., Yu, B., 1998. The Minimum Description Length Principle in Coding and Modeling. IEEE Trans. Inf. Theory 44, 2743–2760. https://doi.org/10.1109/18.720554

Barton, N., 1982. Modelling rock joint behavior from in situ block tests: implications for nuclear waste repository design.

Barton, N., 1976. The shear strength of rock and rock joints. Int. J. Rock Mech. Min. Sci. https://doi.org/10.1016/0148-9062(76)90003-6

Barton, N., 1973. Review of a new shear-strength criterion for rock joints. Eng. Geol. https://doi.org/10.1016/0013-7952(73)90013-6

Barton, N., Choubey, V., 1977. The shear strength of rock joints in theory and practice. Rock Mech. Felsmechanik Mécanique des Roches 10, 1–54. https://doi.org/10.1007/BF01261801

Battulwar, R., 2018. Flight Path Planning and Optimization for High-Resolution Imaging in Open Pit Mines by UAVs. University of Nevada Reno.

Battulwar, R., Emami, E., Zare Naghadehi, M., Sattarvand, J., 2020a. Automatic Extraction of Joint Orientations in Rock Mass Using PointNet and DBSCAN, in: G. Bebis et Al. (Eds.): ISVC 2020, LNCS 12510. pp. 1–10. https://doi.org/https://doi.org/10.1007/978-3-030-64559-5_57

Battulwar, R., Winkelmaier, G., Valencia, J., Bahram, P., Sattarvand, J., 2019. High-resolution modeling of open-pit slopes using UAV and photogrammetry, in: 39th International Symposium on Application of Computers and Operations Research in the Mineral Industry. Wroclaw, Poland, 4-6 June 2019, pp. 661–670.

Battulwar, R., Winkelmaier, G., Valencia, J., Naghadehi, M.Z., Peik, B., Abbasi, B., Parvin, B., Sattarvand, J., 2020b. A Practical Methodology for Generating High-Resolution 3D Models of Open-Pit Slopes using UAVs: Flight Path Planning and Optimization. Remote Sens.

Battulwar, R., Zare-Naghadehi, M., Emami, E., Sattarvand, J., 2021. A state-of-the-art review of automated extraction of rock mass discontinuity characteristics using three-dimensional surface models. J. Rock Mech. Geotech. Eng. https://doi.org/10.1016/j.jrmge.2021.01.008

Belem, T., Homand-Etienne, F., Souley, M., 2000. Quantitative parameters for rock joint surface roughness. Rock Mech. Rock Eng. 33, 217–242. https://doi.org/10.1007/s006030070001

Bellian, J.A., Kerans, C., Jennette, D.C., 2005. Digital Outcrop Models: Applications of Terrestrial Scanning Lidar Technology in Stratigraphic Modeling. J. Sediment. Res. 75, 166–176. https://doi.org/10.2110/jsr.2005.013

Bemis, S.P., Micklethwaite, S., Turner, D., James, M.R., Akciz, S., T. Thiele, S., Bangash, H.A., 2014. Ground-based and UAV-Based photogrammetry: A multi-scale, high-resolution mapping tool for structural geology and paleoseismology. J. Struct. Geol. https://doi.org/10.1016/j.jsg.2014.10.007

Besada-Portas, E., De La Torre, L., De La Cruz, J.M., De Andrés-Toro, B., 2010. Evolutionary trajectory planner for multiple UAVs in realistic scenarios. IEEE Trans. Robot. 26, 619–634. https://doi.org/10.1109/TRO.2010.2048610

Bhide, S., John, N., Kabuka, M.R., 1993. A Boolean Neural Network Approach for the Traveling Salesman Problem. IEEE Trans. Comput. 42, 1271–1278. https://doi.org/10.1109/12.257714

Bircher, A., Kamel, M., Alexis, K., Burri, M., Oettershagen, P., Omari, S., Mantel, T., Siegwart, R., 2016. Three-dimensional coverage path planning via viewpoint resampling and tour optimization for aerial robots. Auton. Robots 40, 1059–1078.

https://doi.org/10.1007/s10514-015-9517-1

Bitenc, M., Kieffer, D.S., Khoshelham, K., 2019. Range Versus Surface Denoising of Terrestrial Laser Scanning Data for Rock Discontinuity Roughness Estimation. Rock Mech. Rock Eng. 52, 3103–3117. https://doi.org/10.1007/s00603-019-01755-2

Bitenc, M., Scott Kieffer, D., Khoshelham, K., Vezočnik, R., 2015. Quantification of rock joint roughness using terrestrial laser scanning, in: Engineering Geology for Society and Territory - Volume 6: Applied Geology for Major Engineering Projects. Springer International Publishing, pp. 835–838. https://doi.org/10.1007/978-3-319-09060-3_150

Bolkas, D., Vazaios, I., Peidou, A., Vlachopoulos, N., 2018. Detection of Rock Discontinuity Traces Using Terrestrial LiDAR Data and Space-Frequency Transforms. Geotech. Geol. Eng. 36, 1745–1765. https://doi.org/10.1007/s10706-017-0430-6

Buckley, S.J., Howell, J.A., Enge, H.D., Kurz, T.H., 2008. Terrestrial laser scanning in geology: Data acquisition, processing and accuracy considerations. J. Geol. Soc. London. 165, 625–638. https://doi.org/10.1144/0016-76492007-100

Cai, M., Kaiser, P.K., Uno, H., Tasaka, Y., Minami, M., 2004. Estimation of rock mass deformation modulus and strength of jointed hard rock masses using the GSI system. Int. J. Rock Mech. Min. Sci. 41, 3–19. https://doi.org/10.1016/S1365-1609(03)00025-X

Cai, Y., Tang, H., Wang, D., Wen, T., 2018. A Method for Estimating the Surface Roughness of Rock Discontinuities. Math. Probl. Eng. https://doi.org/10.1155/2018/9835341

Cao, T., Xiao, A., Wu, L., Mao, L., 2017. Automatic fracture detection based on Terrestrial Laser Scanning data: A new method and case study. Comput. Geosci. 106, 209–216. https://doi.org/10.1016/j.cageo.2017.04.003

Cappiello, A., Chabini, I., Nam, E.K., Luè, A., Abou Zeid, M., 2002. A statistical model of vehicle emissions and fuel consumption, in: IEEE 5th International Conference on Intelligent Transportation Systems. Singapore, Singapore, 6-6 Sept. 2002, pp. 801–809. https://doi.org/10.1109/ITSC.2002.1041322

Car, M., Juric Kacunic, D., Kovacevic, M.S., 2016. Application of unmanned aerial vehicle for landslide mapping, in: International Symposium on Engineering Geodesy - SIG 2016. Varaždin, Croatia, 20-22 May 2016, pp. 549–559.

Cawood, A.J., Bond, C.E., Howell, J.A., Butler, R.W.H., Totake, Y., 2017. LiDAR, UAV or compass-clinometer? Accuracy, coverage and the effects on structural models. J. Struct. Geol. 98, 67–82. https://doi.org/10.1016/j.jsg.2017.04.004

Chen, J., Zhu, H., Li, X., 2016. Automatic extraction of discontinuity orientation from rock mass surface 3D point cloud. Comput. Geosci. 95, 18–31. https://doi.org/10.1016/j.cageo.2016.06.015

Chen, N., Kemeny, J., Jiang, Q., Pan, Z., 2017. Automatic extraction of blocks from 3D point clouds of fractured rock. Comput. Geosci. 109, 149–161. https://doi.org/10.1016/j.cageo.2017.08.013

CloudCompare, 2020.

Colomina, I., Molina, P., 2014. Unmanned aerial systems for photogrammetry and remote sensing: A review. ISPRS J. Photogramm. Remote Sens. https://doi.org/10.1016/j.isprsjprs.2014.02.013

Dewez, T.J.B., Girardeau-Montaut, D., Allanic, C., Rohmer, J., 2917. Facets : a Cloudcompare Plugin to Extract Geological Planes from Unstructured 3d Point Clouds. ISPRS - Int. Arch. Photogramm. Remote Sens. Spat. Inf. Sci. XLI-B5, 799–804. https://doi.org/10.5194/isprsarchives-XLI-B5-799-2016

Dharavath, R., Singh, A.K., 2016. Entity resolution-based Jaccard similarity coefficient for heterogeneous distributed databases, in: Advances in Intelligent Systems and Computing. Springer Verlag, pp. 497–507. https://doi.org/10.1007/978-81-322-2517-1_48

Di Franco, C., Buttazzo, G., 2016. Coverage Path Planning for UAVs Photogrammetry with Energy and Resolution Constraints. J. Intell. Robot. Syst. Theory Appl. 83, 445–462. https://doi.org/10.1007/s10846-016-0348-x

Dips | Analyze orientation-based geological data [WWW Document], 2020. URL https://www.rocscience.com/software/dips (accessed 12.7.20).

DJI, 2020a. DJI Mavic Pro – Specs, Tutorials & Guides. [WWW Document]. URL https://www.dji.com/mavic/info (accessed 4.23.20).

DJI, 2020b. DJI Developer. [WWW Document]. URL https://developer.dji.com/ (accessed 4.23.20).

Do, M.N., Vetterli, M., 2005. The contourlet transform: An efficient directional multiresolution image representation. IEEE Trans. Image Process. 14, 2091–2106. https://doi.org/10.1109/TIP.2005.859376

Drews, T., Miernik, G., Anders, K., Höfle, B., Profe, J., Emmerich, A., Bechstädt, T., 2018. Validation of fracture data recognition in rock masses by automated plane detection in 3D point clouds. Int. J. Rock Mech. Min. Sci. 109, 19–31.

https://doi.org/10.1016/j.ijrmms.2018.06.023

Ergezer, H., Leblebicioglu, M.K., 2013. 3D Path Planning for UAVs for Maximum Information Collection, in: 2013 International Conference On Unmanned Aircraft Systems (ICUAS). IEEE, Atlanta, GA, USA, 28-31 May 2013, pp. 79–88. https://doi.org/10.1109/ICUAS.2013.6564676

Ester, M., Kriegel, H.-P., Sander, J., Xu, X., 1996. A Density-Based Algorithm for Discovering Clusters in Large Spatial Databases with Noise.

FAA, 2016. Remote Pilot-Small Unmanned Aircraft Systems Study Guide. [WWW Document]. URL https://www.faa.gov/regulations_policies/handbooks_manuals/aviation/media/remote_pilot_study_guide.pdf (accessed 4.23.20).

Fardin, N., Feng, Q., Stephansson, O., 2004. Application of a new in situ 3D laser scanner to study the scale effect on the rock joint surface roughness. Int. J. Rock Mech. Min. Sci. 41, 329–335. https://doi.org/10.1016/S1365-1609(03)00111-4

Feng, Q., Röshoff, K., 2015. A Survey of 3D Laser Scanning Techniques for Application to Rock Mechanics and Rock Engineering, in: The ISRM Suggested Methods for Rock Characterization, Testing and Monitoring: 2007-2014. Springer International Publishing, pp. 265–293. https://doi.org/10.1007/978-3-319-07713-0_25

Ferrari, F., Giacomini, A., Thoeni, K., 2016. Qualitative Rockfall Hazard Assessment: A Comprehensive Review of Current Practices. Rock Mech. Rock Eng. 49, 2865–2922. https://doi.org/10.1007/s00603-016-0918-z

Ferrero, A.M., Forlani, G., Roncella, R., Voyat, H.I., 2009a. Advanced geostructural survey methods applied to rock mass characterization. Rock Mech. Rock Eng. 42, 631–665. https://doi.org/10.1007/s00603-008-0010-4

Ferrero, A.M., Forlani, G., Roncella, R., Voyat, H.I., 2009b. Advanced geostructural survey methods applied to rock mass characterization. Rock Mech. Rock Eng. 42, 631–665. https://doi.org/10.1007/s00603-008-0010-4

Fischler, M.A., Bolles, R.C., 1981. Random sample consensus: A Paradigm for Model Fitting with Applications to Image Analysis and Automated Cartography. Commun. ACM 24, 381–395. https://doi.org/10.1145/358669.358692

Franklin, J., Senior, S., 1997. The Ontario rockfall hazard rating system, in: Conference on Engineering Geology and Environment. pp. 647–658.

Franklin, J.A., Maerz, N.H., Po BENNETT, C., 1988. Rock mass characterization using photoanalysis*, International Journal of Mining and Geological Engineering.

Gao, F., Chen, D., Zhou, K., Niu, W., Liu, H., 2019. A Fast Clustering Method for Identifying Rock Discontinuity Sets. KSCE J. Civ. Eng. 23, 556–566. https://doi.org/10.1007/s12205-018-1244-7

García-Cortés, S., Galán, C.O., Argüelles-Fraga, R., Díaz, A.M., 2012. Automatic detection of discontinuities from 3D point clouds for the stability analysis of jointed rock masses, in: Proceedings of the 2012 18th International Conference on Virtual Systems and Multimedia, VSMM 2012: Virtual Systems in the Information Society. pp. 595–598. https://doi.org/10.1109/VSMM.2012.6365985

Ge, Y., Tang, H., Eldin, M.A.M.E., Chen, P., Wang, L., Wang, J., 2015. A Description for Rock Joint Roughness Based on Terrestrial Laser Scanner and Image Analysis. Sci. Rep. 5, 1–10. https://doi.org/10.1038/srep16999

Ge, Y., Tang, H., Xia, D., Wang, L., Zhao, B., Teaway, J.W., Chen, H., Zhou, T., 2018.

Automated measurements of discontinuity geometric properties from a 3D-point cloud based on a modified region growing algorithm. Eng. Geol. 242, 44–54. https://doi.org/10.1016/j.enggeo.2018.05.007

Gigli, G., Casagli, N., 2013. Extraction of rock mass structural data from high resolution laser scanning products, in: Landslide Science and Practice: Spatial Analysis and Modelling. Springer Berlin Heidelberg, pp. 89–94. https://doi.org/10.1007/978-3-642-31310-3_13

Gigli, G., Casagli, N., 2011. Semi-automatic extraction of rock mass structural data from high resolution LIDAR point clouds. Int. J. Rock Mech. Min. Sci. 48, 187–198. https://doi.org/10.1016/j.ijrmms.2010.11.009

Giordan, D., Hayakawa, Y., Nex, F., Remondino, F., Tarolli, P., 2017. Review article: The use of remotely piloted aircraft systems (RPAS) for natural hazards monitoring and management. Nat. Hazards Earth Syst. Sci. Discuss. 1–26. https://doi.org/10.5194/nhess-2017-339

Glover, F., 1990. Artificial intelligence, heuristic frameworks and tabu search. Manag. Decis. Econ. 11, 365–375. https://doi.org/10.1002/mde.4090110512

Goldberg, D.E., 1989. Genetic Algorithms in Search, Optimization and Machine Learning. Addison-Wesley Longman Publishing Co., Inc.75 Arlington Street, Suite 300 Boston, MA, United States.

Gomes, R.K., De Oliveira, L.P.L., Gonzaga, L., Tognoli, F.M.W., Veronez, M.R., De Souza, M.K., 2016. An algorithm for automatic detection and orientation estimation of planar structures in LiDAR-scanned outcrops. Comput. Geosci. 90, 170–178. https://doi.org/10.1016/j.cageo.2016.02.011

Google, 2020. Maps SDK for Android. [WWW Document]. URL https://developers.google.com/maps/documentation/android-sdk/intro (accessed 4.23.20).

Grasselli, G., Wirth, J., Egger, P., 2002. Quantitative three-dimensional description of a rough surface and parameter evolution with shearing. Int. J. Rock Mech. Min. Sci. 39, 789–800. https://doi.org/10.1016/S1365-1609(02)00070-9

Greenwood, W.R., Zekkos, D., Lynch, J.P., Bateman, J.M., Clark, M.K., Chamlagain, D., 2016. UAV-Based 3-D Characterization of Rock Masses and Rock Slides in Nepal.

Guo, J., Liu, S., Zhang, P., Wu, L., Zhou, W., Yu, Y., 2017. Towards semi-automatic rock mass discontinuity orientation and set analysis from 3D point clouds. Comput. Geosci. 103, 164–172. https://doi.org/10.1016/j.cageo.2017.03.017

Guo, J., Liu, Y., Wu, L., Liu, S., Yang, T., Zhu, W., Zhang, Z., 2019. A geometry- and texture-based automatic discontinuity trace extraction method for rock mass point cloud. Int. J. Rock Mech. Min. Sci. 124. https://doi.org/10.1016/j.ijrmms.2019.104132

Guo, J., Wu, L., Zhang, M., Liu, S., Sun, X., 2018. Towards automatic discontinuity trace extraction from rock mass point cloud without triangulation. Int. J. Rock Mech. Min. Sci. 112, 226–237. https://doi.org/10.1016/j.ijrmms.2018.10.023

Hammah, R.E., Curran, J.H., 2000. Validity Measures for the Fuzzy Cluster Analysis of Orientations. IEEE Trans. Pattern Anal. Mach. Intell. 22, 1467–1472. https://doi.org/10.1109/34.895981

Haneberg, W.C., 2008. Using close range terrestrial digital photogrammetry for 3-D rock slope modeling and discontinuity mapping in the United States. Bull. Eng. Geol.

Environ. 67, 457–469. https://doi.org/10.1007/s10064-008-0157-y

Haneberg, W.C., 2007. Directional Roughness Profiles From Three-dimensional Photogrammetric Or Laser Scanner Point Clouds.

Hannon, J., 2007. Slope Stability Radar. Queen’s University, Kingston, Ontario, Canada.

Hartley, R., Zisserman, A., 2004. Multiple View Geometry in Computer Vision, Cambridge University Press. Cambridge University Press.

Hasan, S., Montzka, C., Rüdiger, C., Ali, M., R. Bogena, H., Vereecken, H., 2014. Soil moisture retrieval from airborne L-band passive microwave using high resolution multispectral data. ISPRS J. Photogramm. Remote Sens. 91, 59–71. https://doi.org/10.1016/j.isprsjprs.2014.02.005

Henk, A., Laux, D., 2015. Terrestrial laser scanning and fracture network characterisation-Perspectives for a (semi-) automatic analysis of point cloud data from outcrops. Z. Dt. Ges. Geowiss. (German J. Geol.) 166, 99–118. https://doi.org/10.1127/1860-1804/2015/0089

Hodgetts, D., Gawthorpe, R.L., Wilson, P., Rarity, F., 2007. Integrating digital and traditional field techniques using virtual reality geological studio (VRGS), in: 69th European Association of Geoscientists and Engineers Conference and Exhibition 2007: Securing The Future. Incorporating SPE EUROPEC 2007. Society of Petroleum Engineers, pp. 83–87. https://doi.org/10.3997/2214-4609.201401718

Hong, E.-S., Lee, I.-M., Lee, J.-S., 2006. Measurement of Rock Joint Roughness by 3D Scanner.

Hu, L., Xiao, J., Wang, Y., 2019. Efficient and automatic plane detection approach for 3-D rock mass point clouds. Multimed. Tools Appl. https://doi.org/10.1007/s11042-

019-08189-6

Hussain, A., Muhammad, Y.S., Nauman Sajid, M., Hussain, I., Mohamd Shoukry, A., Gani, S., 2017. Genetic Algorithm for Traveling Salesman Problem with Modified Cycle Crossover Operator. Comput. Intell. Neurosci. 2017, 7430125. https://doi.org/10.1155/2017/7430125

InnovMetric Software | Your 3D Metrology Software Partner [WWW Document], 2020. URL https://www.innovmetric.com/ (accessed 4.6.20).

International society for rock mechanics commission on standardization of laboratory and field tests. Suggested methods for the quantitative description of discontinuities in rock masses, 1978. . Int. J. Rock Mech. Min. Sci. https://doi.org/10.1016/0148-9062(78)91472-9

Jaboyedoff, M., Couture, R., Locat, P., 2009. Structural analysis of Turtle Mountain (Alberta) using digital elevation model: Toward a progressive failure. Geomorphology 103, 5–16. https://doi.org/10.1016/j.geomorph.2008.04.012

Jaboyedoff, M., Metzger, R., Oppikofer, T., Couture, R., Derron, M.-H., Locat, J., Turmel, D., 2007. New insight techniques to analyze rock-slope relief using DEM and 3D-imaging cloud points: COLTOP-3D software Development of landslide-generated tsunami model View project Landslide-generated waves View project New insight techniques to analyze rock-slope. https://doi.org/10.1201/NOE0415444019-c8

Jafari, A., Khishvand, M., Rahami, H., 2013. Developing an algorithm for reconstruction blocky systems in discontinuous media: three-dimensional analysis. Int. J. Numer. Anal. Methods Geomech. 37, 661–684. https://doi.org/10.1002/nag.1113

Jang, H.S., Kang, S.S., Jang, B.A., 2014. Determination of Joint Roughness Coefficients

Using Roughness Parameters. Rock Mech. Rock Eng. 47, 2061–2073. https://doi.org/10.1007/s00603-013-0535-z

JAXA, 1997. ALOS Global Digital Surface Model “ALOS World 3D - 30m” (AW3D30). [WWW Document]. URL https://www.eorc.jaxa.jp/ALOS/en/aw3d30/index.htm (accessed 4.23.20).

Jimenez-Rodriguez, R., Sitar, N., 2006. A spectral method for clustering of rock discontinuity sets. Int. J. Rock Mech. Min. Sci. 43, 1052–1061. https://doi.org/10.1016/j.ijrmms.2006.02.003

Jimenez, R., 2008. Fuzzy spectral clustering for identification of rock discontinuity sets. Rock Mech. Rock Eng. 41, 929–939. https://doi.org/10.1007/s00603-007-0155-6

Kainthola, A., Singh, P.K., Singh, T.N., 2015. Stability investigation of road cut slope in basaltic rockmass, Mahabaleshwar, India. Geosci. Front. 6, 837–845. https://doi.org/10.1016/j.gsf.2014.03.002

Kemeny, John and Turner, Keith and Norton, B., 2006. LIDAR for rock mass characterization: hardware, software, accuracy and best-practices. Laser Photogramm. methods rock face Charact. 49–62.

Kemeny, J., Post, R., 2003. Estimating three-dimensional rock discontinuity orientation from digital images of fracture traces. Comput. Geosci. 29, 65–77. https://doi.org/10.1016/S0098-3004(02)00106-1

Kim, E., Lee, J., Shin, K.G., 2013. Real-time prediction of battery power requirements for electric vehicles, in: ACM/IEEE 4th International Conference on Cyber-Physical Systems, ICCPS 2013. Philadelphia, PA, USA, 8-11 April 2013, pp. 11–20. https://doi.org/10.1145/2502524.2502527

Kim, H.S., Choi, H.K., Lee, K.H., 2009. Feature detection of triangular meshes based on tensor voting theory. Comput. Des. 41, 47–58. https://doi.org/10.1016/J.CAD.2008.12.003

Kirkpatrick, S., Toulouse, G., 1985. Configuration space analysis of travelling salesman problems. J. Phys. 46, 1277–1292. https://doi.org/10.1051/jphys:019850046080127700

Knox, F., 2017. How drones are changing mining. [WWW Document]. BHP. URL https://www.bhp.com/media-and-insights/prospects/2017/04/how-drones-are-changing-mining/ (accessed 4.23.20).

Kong, D., Wu, F., Saroglou, C., 2020. Automatic identification and characterization of discontinuities in rock masses from 3D point clouds. Eng. Geol. 265. https://doi.org/10.1016/j.enggeo.2019.105442

Kurz, T.H., Buckley, S.J., Howell, J.A., Schneider, D., 2011. Integration of panoramic hyperspectral imaging with terrestrial lidar data. Photogramm. Rec. 26, 212–228. https://doi.org/10.1111/j.1477-9730.2011.00632.x

Labate, D., Lim, W.-Q., Kutyniok, G., Weiss, G., 2005. Sparse multidimensional representation using shearlets, in: Papadakis, M., Laine, A.F., Unser, M.A. (Eds.), Wavelets XI. SPIE, p. 59140U. https://doi.org/10.1117/12.613494

Lai, P., Samson, C., Bose, P., 2014. Surface roughness of rock faces through the curvature of triangulated meshes. Comput. Geosci. 70, 229–237. https://doi.org/10.1016/j.cageo.2014.05.010

Large Scale 3D Reality Modeling Software | ContextCapture [WWW Document], 2020. URL https://www.bentley.com/en/products/product-line/reality-modeling-software/contextcapture-center (accessed 11.27.20).

Larrañaga, P., Kuijpers, C.M.H., Murga, R.H., Inza, I., Dizdarevic, S., 1999. Genetic algorithms for the travelling salesman problem: A review of representations and operators. Artif. Intell. Rev. 13, 129–170. https://doi.org/10.1023/A:1006529012972

Lary, D.J., Alavi, A.H., Gandomi, A.H., Walker, A.L., 2016. Machine learning in geosciences and remote sensing. Geosci. Front. 7, 3–10. https://doi.org/10.1016/j.gsf.2015.07.003

Lato, M., Diederichs, M.S., Hutchinson, D.J., Harrap, R., 2009. Optimization of LiDAR scanning and processing for automated structural evaluation of discontinuities in rockmasses. Int. J. Rock Mech. Min. Sci. 46, 194–199. https://doi.org/10.1016/j.ijrmms.2008.04.007

Lato, M., Kemeny, J., Harrap, R.M., Bevan, G., 2013. Rock bench: Establishing a common repository and standards for assessing rockmass characteristics using LiDAR and photogrammetry. Comput. Geosci. 50, 106–114. https://doi.org/10.1016/j.cageo.2012.06.014

Lato, M.J., Diederichs, M.S., Hutchinson, D.J., 2010. Bias correction for view-limited lidar scanning of rock outcrops for structural characterization. Rock Mech. Rock Eng. 43, 615–625. https://doi.org/10.1007/s00603-010-0086-5

Lato, M.J., Vöge, M., 2012. Automated mapping of rock discontinuities in 3D lidar and photogrammetry models. Int. J. Rock Mech. Min. Sci. 54, 150–158. https://doi.org/10.1016/j.ijrmms.2012.06.003

Lee, S., Choi, Y., 2015. Topographic Survey at Small-scale Open-pit Mines using a Popular Rotary-wing Unmanned Aerial Vehicle (Drone). J. Korean Soc. Rock Mech.

25, 462–469. https://doi.org/10.7474/tus.2015.25.5.462

Leica Geosystems [WWW Document], 2020. URL https://leica-geosystems.com/en-us/products/laser-scanners/scanners/leica-rtc360 (accessed 7.4.20).

Lemy, F., Hadjigeorgiou, J., 2003. Discontinuity trace map construction using photographs of rock exposures. Int. J. Rock Mech. Min. Sci. 40, 903–917. https://doi.org/10.1016/S1365-1609(03)00069-8

Li, B., Xu, X., Zhang, L., Han, J., Bian, C., Li, G., Liu, J., Jin, L., 2020. Above-ground biomass estimation and yield prediction in potato by using UAV-based RGB and hyperspectral imaging. ISPRS J. Photogramm. Remote Sens. 162, 161–172. https://doi.org/10.1016/j.isprsjprs.2020.02.013

Li, C.J., Ling, H.,. High-resolution, downward-looking radar imaging using a small consumer drone, in: 2016 IEEE Antennas and Propagation Society International Symposium, APSURSI 2016. Fajardo, Puerto Rico, 26 June-1 July 2016, pp. 2037–2038. https://doi.org/10.1109/APS.2016.7696725

Li, X., Chen, J., Zhu, H., 2016. A new method for automated discontinuity trace mapping on rock mass 3D surface model. Comput. Geosci. 89, 118–131. https://doi.org/10.1016/j.cageo.2015.12.010

Li, X., Chen, Z., Chen, J., Zhu, H., 2019. Automatic characterization of rock mass discontinuities using 3D point clouds. Eng. Geol. 259. https://doi.org/10.1016/j.enggeo.2019.05.008

Life as a drone pilot. [WWW Document], 2020. . Rio Tinto. URL https://www.riotinto.com/en/news/stories/life-as-drone-pilot (accessed 4.23.20).

Longoni, L., Arosio, D., Scaioni, M., Papini, M., Zanzi, L., Roncella, R., Brambilla, D.,

2012. Surface and subsurface non-invasive investigations to improve the characterization of a fractured rock mass. J. Geophys. Eng. 9, 461. https://doi.org/10.1088/1742-2132/9/5/461

Lucieer, A., Robinson, S., Turner, D., 2011. Unmanned aerial vehicle (UAV) remote sensing for hyperspatial terrain mapping of antarctic moss beds based on structure from motion (SfM) point clouds, in: 34th International Symposium on Remote Sensing of Environment - The GEOSS Era: Towards Operational Environmental Monitoring. Sydney, Australia, 10-15 April 2011.

Mabee, S.B., Hardcastle, K.C., Wise, D.U., 1994. A Method of Collecting and Analyzing Lineaments for Regional-Scale Fractured-Bedrock Aquifer Studies. Ground Water 32, 884–894. https://doi.org/10.1111/j.1745-6584.1994.tb00928.x

Maerz, N.H., Franklin, J.A., Bennett, C.P., 1990. Joint roughness measurement using shadow profilometry. Int. J. Rock Mech. Min. Sci. 27, 329–343. https://doi.org/10.1016/0148-9062(90)92708-M

Mah, J., Samson, C., McKinnon, S.D., 2011. 3D laser imaging for joint orientation analysis. Int. J. Rock Mech. Min. Sci. 48, 932–941. https://doi.org/10.1016/j.ijrmms.2011.04.010

Malinverno, A., 1990. A simple method to estimate the fractal dimension of a self-affine series. Geophys. Res. Lett. 17, 1953–1956. https://doi.org/10.1029/GL017i011p01953

Martínez-Carricondo, P., Agüera-Vega, F., Carvajal-Ramírez, F., Mesas-Carrascosa, F.J., García-Ferrer, A., Pérez-Porras, F.J., 2018. Assessment of UAV-photogrammetric mapping accuracy based on variation of ground control points. Int. J. Appl. Earth Obs.

Geoinf. 72, 1–10. https://doi.org/10.1016/j.jag.2018.05.015

MathWorks, 2020. MATLAB - MathWorks - MATLAB & Simulink [WWW Document]. URL https://www.mathworks.com/products/matlab.html (accessed 4.21.20).

MATLAB - MathWorks - MATLAB & Simulink [WWW Document], 2020. URL https://www.mathworks.com/products/matlab.html (accessed 4.21.20).

Mauldon, M., Dunne, W.M., Rohrbaugh, M.B., 2001. Circular scanlines and circular windows: New tools for characterizing the geometry of fracture traces. J. Struct. Geol. 23, 247–258. https://doi.org/10.1016/S0191-8141(00)00094-8

Mavrouli, O., Corominas, • J, Jaboyedoff, • M, 2015. Size Distribution for Potentially Unstable Rock Masses and In Situ Rock Blocks Using LIDAR-Generated Digital Elevation Models. Rock Mech. Rock Eng. 48, 1589–1604. https://doi.org/10.1007/s00603-014-0647-0

Meneses, S., Cueva, R., Tupia, M., Guanira, M., 2017. A genetic algorithm to solve 3D traveling salesman problem with initial population based on a GRASP algorithm. J. Comput. Methods Sci. Eng. 17, S1–S10. https://doi.org/10.3233/JCM-160675

MicMac [WWW Document], 2020. URL https://micmac.ensg.eu/index.php/Accueil (accessed 11.27.20).

Miller, C.E., Zemlin, R.A., Tucker, A.W., 1960. Integer Programming Formulation of Traveling Salesman Problems. J. ACM 7, 326–329. https://doi.org/10.1145/321043.321046

MSEdge: A Multi-Scale Edge Chain Detector, 2017. , in: The 5th International Conference on Computational Visual Media (CVM).

Myers, N.O., 1962. Characterization of surface roughness. Wear 5, 182–189.

https://doi.org/10.1016/0043-1648(62)90002-9

NASA, 2012. ASTER: Advanced Spaceborne Thermal Emission and Reflection Radiometer. [WWW Document]. URL https://asterweb.jpl.nasa.gov/ (accessed 4.23.20).

Newmont, 2017. Newmont 2017 Sustainability Report [WWW Document]. Newmont. URL https://www.newmont.com/files/doc_downloads/newmont_archive/Newmont_2017-Beyond-the-Mine-Full-Report.pdf (accessed 4.23.20).

Nosal, E.M., 2008. Flood-fill algorithms used for passive acoustic detection and tracking, in: New Trends for Environmental Monitoring Using Passive Systems, PASSIVE 2008. https://doi.org/10.1109/PASSIVE.2008.4786975

Olariu, M.I., Ferguson, J.F., Aiken, C.L.V., Xu, X., 2008a. Outcrop fracture characterization using terrestrial laser scanners: Deep-water Jackfork sandstone at big rock quarry, Arkansas. Geosphere 4, 247–259. https://doi.org/10.1130/GES00139.1

Olariu, M.I., Ferguson, J.F., Aiken, C.L.V., Xu, X., 2008b. Outcrop fracture characterization using terrestrial laser scanners: Deep-water Jackfork sandstone at big rock quarry, Arkansas. Geosphere 4, 247–259. https://doi.org/10.1130/GES00139.1

Oppikofer, T., Jaboyedoff, M., Blikra, L., Derron, M.-H., Metzger, R., 2009. Characterization and monitoring of the Åknes rockslide using terrestrial laser scanning. Nat. Hazards Earth Syst. Sci. 9, 1003–1019. https://doi.org/10.5194/nhess-9-1003-2009

Oppikofer, T., Jaboyedoff, M., Pedrazzini, A., Derron, M.-H., Blikra, L.H., 2011. Detailed DEM analysis of a rockslide scar to characterize the basal sliding surface of active rockslides. J. Geophys. Res. Earth Surf. 116. https://doi.org/10.1029/2010JF001807

Patton, F.D., 1966. Multiple Modes of Shear Failure In Rock.

Pehlivanoglu, Y.V., Hacioglu, A., 2007. Vibrational genetic algorithm based path planner for autonomous UAV in spatial data based environments, in: 3rd International Conference on Recent Advances in Space Technologies, RAST 2007. Istanbul, Turkey, 14-16 June 2007, pp. 573–578. https://doi.org/10.1109/RAST.2007.4284058

Peik, B., Zare Naghadehi, M., Battulwar, R., Abbasi, B., Sattarvand, J., Sadrabadi Soltany, M., Azarfar, B., 2020a. An Analytical Study of Rockfall Trajectory Simulation to Develop Hazard Maps for Open-Pit Mines, in: 54th US Rock Mechanics/Geomechanics Symposium. American Rock Mechanics Association. Online.

Peik, B., Zare Naghadehi, M., Battulwar, R., Abbasi, B., Sattarvand, J., Sadrabadi Soltany, M., Azarfar, B., 2020b. An Analytical Study of Rockfall Trajectory Simulation to Develop Hazard Maps for Open-Pit Mines., in: 54th US Rock Mechanics/Geomechanics Symposium. American Rock Mechanics Association. Online.

Peirson, L., 1992. Rockfall Hazard Rating System. National Academy Press.

PIX4D, 2018. How to verify that there is enough overlap between the images. [WWW Document]. URL https://support.pix4d.com/hc/en-us/articles/203756125-How-to-verify-that-there-is-enough-overlap-between-the-images (accessed 4.23.20).

Pollyea, R.M., Fairley, J.P., 2011. Estimating surface roughness of terrestrial laser scan data using orthogonal distance regression. Geology 39, 623–626. https://doi.org/10.1130/G32078.1

Preparata, F.P., Hong, S.J., 1977. Convex Hulls of Finite Sets of Points in Two and Three Dimensions. Commun. ACM 20, 87–93. https://doi.org/10.1145/359423.359430

Priest, S.D., Hudson, J.A., 1981. Estimation of discontinuity spacing and trace length using scanline surveys. Int. J. Rock Mech. Min. Sci. 18, 183–197. https://doi.org/10.1016/0148-9062(81)90973-6

Qi, C.R., Su, H., Mo, K., Guibas, L.J., 2017. PointNet: Deep Learning on Point Sets for 3D Classification and Segmentation, in: IEEE Conference on Computer Vision and Pattern Recognition. Honolulu, Hawaii, pp. 79–85.

RealityCapture: Mapping and 3D Modeling Photogrammetry Software - CapturingReality.com [WWW Document], 2020. URL https://www.capturingreality.com/ (accessed 11.27.20).

ReCap Pro Features | 3D Scanning Software Features | Autodesk [WWW Document], 2020. URL https://www.autodesk.com/products/recap/features?plc=RECAP&term=1-YEAR&support=ADVANCED&quantity=1#internal-link-buy (accessed 11.27.20).

Reid, T.R., Harrison, J.P., 2000. A semi-automated methodology for discontinuity trace detection in digital images of rock mass exposures. Int. J. Rock Mech. Min. Sci. 37, 1073–1089. https://doi.org/10.1016/S1365-1609(00)00041-1

Riquelme, A., Cano, M., Tomás, R., Abellán, A., 2017. Identification of Rock Slope Discontinuity Sets from Laser Scanner and Photogrammetric Point Clouds: A Comparative Analysis, in: Procedia Engineering. Elsevier Ltd, pp. 838–845. https://doi.org/10.1016/j.proeng.2017.05.251

Riquelme, A., Tomás, R., Cano, M., Abellan, A., 2016. Using open-source software for extracting geomechanical parameters of a rock mass from 3D point clouds: Discontinuity set extractor and SMRTool.

Riquelme, A., Tomás, R., Cano, M., Pastor, J.L., Abellán, A., 2018. Automatic Mapping of Discontinuity Persistence on Rock Masses Using 3D Point Clouds. Rock Mech. Rock Eng. 51, 3005–3028. https://doi.org/10.1007/s00603-018-1519-9

Riquelme, A.J., Abellán, A., Tomás, R., 2015. Discontinuity spacing analysis in rock masses using 3D point clouds. Eng. Geol. 195, 185–195. https://doi.org/10.1016/j.enggeo.2015.06.009

Riquelme, A.J., Abellán, A., Tomás, R., Jaboyedoff, M., 2014. A new approach for semi-automatic rock mass joints recognition from 3D point clouds. Comput. Geosci. 68, 38–52. https://doi.org/10.1016/j.cageo.2014.03.014

Riquelme, A.J., Tomás, R., Abellán, A., 2016. Characterization of rock slopes through slope mass rating using 3D point clouds. Int. J. Rock Mech. Min. Sci. 84, 165–176. https://doi.org/10.1016/j.ijrmms.2015.12.008

Rock Mass Characterization Service - Split-FX [WWW Document], 2020. URL https://www.spliteng.com/products/split-fx-analysis-service/ (accessed 3.24.20).

Rodriguez, A., Laio, A., 2014. Clustering by fast search and find of density peaks. Science (80-.). 344, 1492–1496. https://doi.org/10.1126/science.1242072

Roncella, R., Forlani, G., 2005. Extraction of planar patches from point clouds to retrieve dip and dip direction of rock discontinuities, in: ISPRS WG III/3, III/4, V/3 Workshop "Laser Scanning 2005." Enschede, the Netherlands, September 12-14, pp. 162–167.

Rosen, E., Jansson, E., Brundin, M., 2014. Implementation of a fast and efficient concave hull algorithm - PDF Free Download.

Rousseeuw, P.J., 1987. Silhouettes: A graphical aid to the interpretation and validation of cluster analysis. J. Comput. Appl. Math. 20, 53–65. https://doi.org/10.1016/0377-0427(87)90125-7

Salvini, R., Mastrorocco, G., Seddaiu, M., Rossi, D., Vanneschi, C., 2017. The use of an unmanned aerial vehicle for fracture mapping within a marble quarry (Carrara, Italy): photogrammetry and discrete fracture network modelling. Geomatics, Nat. Hazards Risk 8, 34–52. https://doi.org/10.1080/19475705.2016.1199053

Santi, P.M., Russell, C.P., Higgins, J.D., Spriet, J.I., 2009. Modification and statistical analysis of the Colorado Rockfall Hazard Rating System. Eng. Geol. 104, 55–65. https://doi.org/10.1016/j.enggeo.2008.08.009

Schnabel, R., Wahl, R., Klein, R., 2007. Efficient RANSAC for Point-Cloud Shape Detection. Comput. Graph. Forum 26, 214–226. https://doi.org/10.1111/j.1467-8659.2007.01016.x

Senior, S., 2003. Ontario rockfall hazard rating system. Fieldprocedures manual. Ontario.

Shivgan, R., Dong, Z.,. Energy-Efficient Drone Coverage Path Planning using Genetic Algorithm, in: 2020 IEEE 21st International Conference on High Performance Switching and Routing (HPSR). Newark, NJ, USA, 11-14 May 2020, pp. 1–6. https://doi.org/10.1109/HPSR48589.2020.9098989

Siebert, S., Teizer, J., 2014. Mobile 3D mapping for surveying earthwork projects using an Unmanned Aerial Vehicle (UAV) system. Autom. Constr. 41, 1–14. https://doi.org/10.1016/j.autcon.2014.01.004

Slob, S., Hack, R., 2004. 3D Terrestrial Laser Scanning as a New Field Measurement and Monitoring Technique, in: Engineering Geology for Infrastructure Planning in

Europe. Lecture Notes in Earth Sciences. Springer Berlin Heidelberg, pp. 179–189. https://doi.org/10.1007/978-3-540-39918-6_22

Slob, Siefko, Van Knapen, B., Hack, Robert, Turner, K., Kemeny, J., Slob, S, Hack, R, 2005. Method for Automated Discontinuity Analysis of Rock Slopes with Three-Dimensional Laser Scanning. Transp. Res. Rec. J. Transp. Res. Board 1913, 187–194. https://doi.org/https://doi.org/10.1177/0361198105191300118

Soilán, M., Lindenbergh, R., Riveiro, B., Sánchez-Rodríguez, A., 2019. PointNet for the Automatic Classification of Aerial Point Clouds. ISPRS Ann. Photogramm. Remote Sens. Spat. Inf. Sci. IV-2/W5, 445–452. https://doi.org/10.5194/isprs-annals-IV-2-W5-445-2019

Sturzenegger, M., Stead, D., 2009a. Close-range terrestrial digital photogrammetry and terrestrial laser scanning for discontinuity characterization on rock cuts. Eng. Geol. 106, 163–182. https://doi.org/10.1016/j.enggeo.2009.03.004

Sturzenegger, M., Stead, D., 2009b. Quantifying discontinuity orientation and persistence on high mountain rock slopes and large landslides using terrestrial remote sensing techniques. Nat. Hazards Earth Syst. Sci. 9, 267–287. https://doi.org/10.5194/nhess-9-267-2009

Sturzenegger, M., Stead, D., Elmo, D., 2011. Terrestrial remote sensing-based estimation of mean trace length, trace intensity and block size/shape. Eng. Geol. 119, 96–111. https://doi.org/10.1016/j.enggeo.2011.02.005

Suh, J., Choi, Y., 2017. Mapping hazardous mining-induced sinkhole subsidence using unmanned aerial vehicle (drone) photogrammetry. Environ. Earth Sci. 76. https://doi.org/10.1007/s12665-017-6458-3

Suziedelyte Visockiene, J., Puziene, R., Stanionis, A., Tumeliene, E., 2016. Unmanned Aerial Vehicles for Photogrammetry: Analysis of Orthophoto Images over the Territory of Lithuania. Int. J. Aerosp. Eng. 2016. https://doi.org/10.1155/2016/4141037

Tatone, B.S.A., Grasselli, G., 2013. An investigation of discontinuity roughness scale dependency using high-resolution surface measurements. Rock Mech. Rock Eng. 46, 657–681. https://doi.org/10.1007/s00603-012-0294-2

Terzaghi, R.D., 1965. Sources of Error in Joint Surveys. http://dx.doi.org/10.1680/geot.1965.15.3.287 15, 287–304. https://doi.org/10.1680/GEOT.1965.15.3.287

Thiele, Samuel T, Grose, L., Samsu, A., Micklethwaite, S., Vollgger, S.A., Cruden, A.R., 2017. Rapid, semi-automatic fracture and contact mapping for point clouds, images and geophysical data. Solid Earth 8, 1241–1253. https://doi.org/10.5194/se-8-1241-2017

Thiele, Samuel T., Grose, L., Samsu, A., Micklethwaite, S., Vollgger, S.A., Cruden, A.R., 2017. Rapid, semi-automatic fracture and contact mapping for point clouds, images and geophysical data. Solid Earth 8, 1241–1253. https://doi.org/10.5194/se-8-1241-2017

Torres, M., Pelta, D.A., Verdegay, J.L., Torres, J.C., 2016. Coverage path planning with unmanned aerial vehicles for 3D terrain reconstruction. Expert Syst. Appl. 55, 441–451. https://doi.org/10.1016/j.eswa.2016.02.007

Tournaire, O., Paparoditis, N., 2009. A geometric stochastic approach based on marked point processes for road mark detection from high resolution aerial images. ISPRS J.

Photogramm. Remote Sens. 64, 621–631. https://doi.org/10.1016/j.isprsjprs.2009.05.005

Trimble Inpho | Trimble Geospatial [WWW Document], 2020. URL https://geospatial.trimble.com/products-and-solutions/inpho (accessed 11.27.20).

Tse, R., Cruden, D.M., 1979. Estimating joint roughness coefficients. Int. J. Rock Mech. Min. Sci. 16, 303–307. https://doi.org/10.1016/0148-9062(79)90241-9

Tseng, C.-M., Chau, C.-K., Elbassioni, K., Khonji, M., 2017. Autonomous Recharging and Flight Mission Planning for Battery-operated Autonomous Drones. arXiv Robot.

Umili, G., Ferrero, A., Einstein, H.H., 2013. A new method for automatic discontinuity traces sampling on rock mass 3D model. Comput. Geosci. 51, 182–192. https://doi.org/10.1016/j.cageo.2012.07.026

Ünlüsoy, D., Süzen, M.L., 2019. A new method for automated estimation of joint roughness coefficient for 2D surface profiles using power spectral density. Int. J. Rock Mech. Min. Sci. 125, 104156. https://doi.org/10.1016/j.ijrmms.2019.104156

USGS, 2018. USGS EROS Archive - Digital Elevation - Shuttle Radar Topography Mission (SRTM) 1 Arc-Second Global. [WWW Document]. Earth Resour. Obs. Sci. Cent. https://doi.org/10.5066/F7PR7TFT

Valencia, J., Battulwar, R., Naghadehi, M.Z., Sattarvand, J., 2019. Enhancement of explosive energy distribution using UAVs and machine learning, in: 39th International Symposium on Application of Computers and Operations Research in the Mineral Industry. Wroclaw, Poland, 4-6 June 2019, pp. 670–677.

Van Knapen, B., Slob, S., 2006. Identification and characterisation of rock mass discontinuity sets using 3D laser scanning.

Vasuki, Y., Holden, E.J., Kovesi, P., Micklethwaite, S., 2014. Semi-automatic mapping of geological Structures using UAV-based photogrammetric data: An image analysis approach. Comput. Geosci. 69, 22–32. https://doi.org/10.1016/j.cageo.2014.04.012

VisualSFM : A Visual Structure from Motion System [WWW Document], 2020. URL http://ccwu.me/vsfm/ (accessed 11.27.20).

Vivas, J., Hunt, C., Stead, D., Allen, D.M., Elmo, D., 2015. Characterising Groundwater in Rock Slopes using a Combined Remote Sensing - Numerical Modelling Approach.

Vöge, M., Lato, M.J., Diederichs, M.S., 2013. Automated rockmass discontinuity mapping from 3-dimensional surface data. Eng. Geol. 164, 155–162. https://doi.org/10.1016/j.enggeo.2013.07.008

Vollgger, S.A., Cruden, A.R., 2016. Mapping folds and fractures in basement and cover rocks using UAV photogrammetry, Cape Liptrap and Cape Paterson, Victoria, Australia. J. Struct. Geol. 85, 168–187. https://doi.org/10.1016/j.jsg.2016.02.012

Wahab, M.H.A., Zakaria, N., Latip, R., Salam, R.A., 2013. Image contrast enhancement for outdoor machine vision applications, in: 2013 International Conference on Soft Computing and Pattern Recognition, SoCPaR 2013. Institute of Electrical and Electronics Engineers Inc., pp. 377–383. https://doi.org/10.1109/SOCPAR.2013.7054162

Wang, X., Zou, L., Shen, X., Ren, Y., Qin, Y., 2017. A region-growing approach for automatic outcrop fracture extraction from a three-dimensional point cloud. Comput. Geosci. 99, 100–106. https://doi.org/10.1016/j.cageo.2016.11.002

Wang, X.C., Cao, J.J., Liu, X.P., Li, B.J., Shi, X.Q., Sun, Y.Z., 2012. Feature detection of triangular meshes via neighbor supporting. J. Zhejiang Univ. Sci. C.

https://doi.org/10.1631/jzus.C1100324

Wang, Y., Feng, H.Y., Delorme, F.É., Engin, S., 2013. An adaptive normal estimation method for scanned point clouds with sharp features. CAD Comput. Aided Des. 45, 1333–1348. https://doi.org/10.1016/j.cad.2013.06.003

Weidner, L., Walton, G., Kromer, R., 2019. Classification methods for point clouds in rock slope monitoring: A novel machine learning approach and comparative analysis. Eng. Geol. 263. https://doi.org/10.1016/j.enggeo.2019.105326

Wichmann, V., Strauhal, T., Fey, C., Perzlmaier, S., 2019. Derivation of space-resolved normal joint spacing and in situ block size distribution data from terrestrial LIDAR point clouds in a rugged Alpine relief (Kühtai, Austria). Bull. Eng. Geol. Environ. 78, 4465–4478. https://doi.org/10.1007/s10064-018-1374-7

Winkelmaier, G., Battulwar, R., Khoshdeli, M., Valencia, J., Sattarvand, J., Bahram, P., 2020. Topographically Guided UAV for Identifying Tension Cracks using Image-Based Analytics in Open-Pit Mines. IEEE J. Trans. Ind. Eng. https://doi.org/10.1109/TIE.2020.2992011

Yan, G., Li, L., Coy, A., Mu, X., Chen, S., Xie, D., Zhang, W., Shen, Q., Zhou, H., 2019. Improving the estimation of fractional vegetation cover from UAV RGB imagery by colour unmixing. ISPRS J. Photogramm. Remote Sens. 158, 23–34. https://doi.org/10.1016/j.isprsjprs.2019.09.017

Yang, X.S., 2009. Firefly algorithms for multimodal optimization, in: Lecture Notes in Computer Science (Including Subseries Lecture Notes in Artificial Intelligence and Lecture Notes in Bioinformatics). Springer, Berlin, Heidelberg, pp. 169–178. https://doi.org/10.1007/978-3-642-04944-6_14

Ye, J., 2015. Improved cosine similarity measures of simplified neutrosophic sets for medical diagnoses. Artif. Intell. Med. 63, 171–179. https://doi.org/10.1016/j.artmed.2014.12.007

Ye, J., 2012. Multicriteria decision-making method using the Dice similarity measure based on the reduct intuitionistic fuzzy sets of interval-valued intuitionistic fuzzy sets. Appl. Math. Model. 36, 4466–4472. https://doi.org/10.1016/j.apm.2011.11.075

Yong, R., Ye, J., Liang, Q.F., Huang, M., Du, S.G., 2018. Estimation of the joint roughness coefficient (JRC) of rock joints by vector similarity measures. Bull. Eng. Geol. Environ. 77, 735–749. https://doi.org/10.1007/s10064-016-0947-6

Zare, M., Jimenez, R., 2015a. On the Development of a Slope Instability Index for Open-Pit Mines using an Improved Systems Approach, in: ISRM Regional Symposium - EUROCK 2015. International Society for Rock Mechanics and Rock Engineering, Salzburg, Austria, pp. 1041–1046.

Zare, M., Jimenez, R., 2015b. On the Development of a Slope Instability Index for Open-Pit Mines using an Improved Systems Approach, in: ISRM Regional Symposium - EUROCK 2015. International Society for Rock Mechanics and Rock Engineering, Salzburg, Austria.

Zare, M., Kakaie, R., Torabi, S.R., Jalali, S.M.E., 2008. A New Empirical Criterion for Prediction of the Shear Strength of Natural Infilled Rock Joints under Constant Normal Load (CNL) Conditions, in: 5th Asian Rock Mechanics Symposium (ARMS5). Tehran, Iran.

Zare Naghadehi, M., 2015. Laboratory study of the shear behaviour of natural rough rock joints infilled by different soils. Period. Polytech. Civ. Eng. 59, 413–421.

https://doi.org/10.3311/PPci.7928

Zare Naghadehi, M., Jimenez, R., KhaloKakaie, R., Jalali, S.M.E., 2013. A new open-pit mine slope instability index defined using the improved rock engineering systems approach. Int. J. Rock Mech. Min. Sci. 61, 1–14. https://doi.org/10.1016/j.ijrmms.2013.01.012

Zekkos, D., Professor, A., Greenwood, W., Lynch, J., Athanasopoulos-Zekkos, A., Clark, M., 2018. Lessons Learned from the Application of UAV-Enabled Structure-From-Motion Photogrammetry in Geotechnical Engineering. Int. J. Geoengin. Case Hist. © 4, 254. https://doi.org/10.4417/IJGCH-04-04-03

Zhang, G., Karakus, M., Tang, H., Ge, Y., Jiang, Q., 2017a. Estimation of Joint Roughness Coefficient from Three-Dimensional Discontinuity Surface. Rock Mech. Rock Eng. 50, 2535–2546. https://doi.org/10.1007/s00603-017-1264-5

Zhang, G., Karakus, M., Tang, H., Ge, Y., Jiang, Q., 2017b. Estimation of Joint Roughness Coefficient from Three-Dimensional Discontinuity Surface. Rock Mech. Rock Eng. 50, 2535–2546. https://doi.org/10.1007/s00603-017-1264-5

Zhang, G., Karakus, M., Tang, H., Ge, Y., Zhang, L., 2014a. A new method estimating the 2D Joint Roughness Coefficient for discontinuity surfaces in rock masses. Int. J. Rock Mech. Min. Sci. 72, 191–198. https://doi.org/10.1016/j.ijrmms.2014.09.009

Zhang, G., Karakus, M., Tang, H., Ge, Y., Zhang, L., 2014b. A new method estimating the 2D Joint Roughness Coefficient for discontinuity surfaces in rock masses. Int. J. Rock Mech. Min. Sci. 72, 191–198. https://doi.org/10.1016/j.ijrmms.2014.09.009

Zhang, L., Einstein, H.H., 1998. Estimating the mean trace length of rock discontinuities. Rock Mech. Rock Eng. 31, 217–235. https://doi.org/10.1007/s006030050022

Zhang, P., Li, J., Yang, X., Zhu, H., 2018. Semi-automatic extraction of rock discontinuities from point clouds using the ISODATA clustering algorithm and deviation from mean elevation. Int. J. Rock Mech. Min. Sci. 110, 76–87. https://doi.org/10.1016/j.ijrmms.2018.07.009

Zhang, P., Zhao, Q., Tannant, D.D., Ji, T., Zhu, H., 2019. 3D mapping of discontinuity traces using fusion of point cloud and image data. Bull. Eng. Geol. Environ. 78, 2789–2801. https://doi.org/10.1007/s10064-018-1280-z